PHASE NOISE OF NANOELECTROMECHANICAL SYSTEMS

Thesis by

Ya-Tang Yang

In Partial Fulfillment of the Requirements for the

Degree of

Doctor of Philosophy

CALIFORNIA INSTITUTE OF TECHNOLOGY

Pasadena, California

2007

(Defended August 9, 2004)

© 2007

Ya-Tang Yang

All Rights Reserved

Dedicated to

my family

ACKNOWLEDGEMENTS

Through the course of my study in Caltech, I have gained much more than I originally anticipated. During the process of working on graduate research and writing this thesis, many things have happened that were better and worse than I expect. The period of time I spent at Caltech certainly brought major transformations to my entire life as a result of friendship, team work, persistence, intellectual education, sorrow, and merriment.

First, I would like to thank the Lord for His bountiful supply through these years and I would certainly acknowledge the reigning of His throne over all things through my toughest time in my personal life and school years. He is active and living God and my ultimate protector. I sincerely hope this thesis will in some way glorify Him for His purpose on earth.

I would like to acknowledge the research opportunity provided by my graduate advisor, Prof. Michael Roukes. Through the training in his research group, I have acquired incredibly many technical and personal skills that are indispensable in my career development. I am also privileged to work with so many talented people and benefit from them. Special thanks go to Prof. Carlo Callegari for his support both on the professional and the personal level. Carlo has made many breakthroughs in our research sometimes through our "constructive" confrontation and brainstorming. I very much enjoyed his company for the time we spent chatting about many small but important things about life in the cafe and the lab. I would also like to thank Philip Xiao-li Feng for his friendship, hands-on help in the lab, and efforts to get our results published. I have collaborated on various projects with Prof. Kamil Ekinci, Larry Schiviaone, Dr. Warren Fon, Dr. Darrel Harrington, Dr. Henry Xue-Ming Huang, Dr. Hong Tang, Dr. Ali Husain, Prof. Chris Zorman, Prof. Jim Hone, Dr. Henk Postma, Prof. Keith Schwab, Meher Prakash, Inna Kozinsky, and many others, whose

help has been invaluable for making my graduate research productive. I also thank our honorary group member, Prof. Philps Wigen from Ohio State University, for his personal support and encouragement.

I am grateful to my mother Li-chu Chu for her unconditioned love and support and dedicate my doctorate degree to her. During my stay at Caltech, major tragedy has happened to my family. Ever since, the prayer, fellowship, support, and practical advice from the brothers and sisters of the church in Monterey Park and Santa Clara have eased my pain and anxiety in this prolonged academic process of obtaining the diploma. Last but not least, I would like thank my fiancée, Jessie Yung-chieh Yu, for her thoughtfulness and prayer for me and my family. She has brought me joy and peace beyond words and knowledge and dissolved my confusion about life in many cases. As we begin the new phase in our life, I am indebted to her for her love through this period and for many years to come.

ABSTRACT

Nanoelectromechanical systems (NEMS) are microelectromechanical devices (MEMS) scaled down to nanometer range. NEMS resonators can be fabricated to achieve high natural resonance frequencies, exceeding 1 GHz with quality factors in excess of 10^4. These resonators are candidates for ultrasensitive mass sensors and frequency determining elements of precision on-chip clocks. As the size of the NEMS resonators is scaled downward, some fundamental and nonfundamental noise processes will impose sensitivity limits to their performance. In this work, we examine both fundamental and nonfundamental noise processes to obtain the corresponding expressions for phase noise density, Allan deviation, and mass sensitivity. Fundamental noise processes considered here include thermomechanical noise, momentum-exchange noise, adsorption-desorption noise, diffusion noise, and temperature-fluctuation noise. For nonfundamental noise processes, we develop a formalism to consider the Nyquist-Johnson noise from transducer-amplifier implementations.

As an initial step to experimental exploration of these noise processes, we demonstrate the phase noise measurement of NEMS using the phase-locked loop scheme. We analyze control servo behavior of the phase-locked loop and describe several implementation schemes at very high frequency and ultra high frequency bands. By incorporating the ~190 MHz NEMS resonator into the frequency modulation phase-locked loop, we investigate the diffusion noise arising from xenon atoms adsorbed on the device surface. Our experimental results can be explained with the diffusion noise theory. The measured spectra of fractional frequency noise confirm the predicted functional form from the diffusion noise theory and are fitted to extract the diffusion coefficients of adsorbed xenon atoms. Moreover, the observed Allan deviation is consistent with the theoretical

estimates from diffusion noise theory, using the total number of adsorbed atoms and extracted diffusion times.

Finally, very high frequency NEMS devices provide unprecedented potential for mass sensing into the zeptogram level due to their minuscule mass and high quality factor. We demonstrate *in situ* measurements in real time with mass noise floor ~20 zeptogram. Our best mass sensitivity corresponds to ~7 zeptograms, equivalent to ~30 xenon atoms or the mass of an individual 4 kDa molecule. Detailed analysis of the ultimate sensitivity of such devices based on these experimental results indicates that NEMS can ultimately provide inertial mass sensing of individual intact, electrically neutral macromolecules with single-Dalton (1 amu) sensitivity. This is an exciting prospect—when realized it will blur the traditional distinction between inertial mass sensing and mass spectrometry. We anticipate that it will also open intriguing possibilities in atomic physics and life science.

CONTENTS

FIGURES

TABLES

Chapter 1

Overview

1.1 Nanoelectromechanical Systems

Nanoelectromechanical systems (NEMS) are microelectromechanical devices (MEMS) scaled down to nanometer range.[1] NEMS have a lot of intriguing attributes.[2] They offer access to fundamental frequencies in the microwave range; [3] quality factor (Q) in the tens of thousands; [4] active mass in the femtogram range; force sensitivities at the attonewton level;[5,6] mass sensitivity at the level of individual molecules[7] — this list goes on. These traits translate into new prospects for a variety of important technological applications. Among them, nanomechanical resonators are rapidly being pushed to smaller sizes and higher frequencies due to their applications as Q filters and on-chip clocks.[4] The fully integrated NEMS oscillators will boast smaller size and lower power consumption and thus can potentially replace their macroscopic counterparts such as the quartz crystal oscillators and surface wave acoustic resonators.

The resonance frequency in general scales as $1/L$, where L is the scale of the resonator. As size scales are reduced and frequency is increased, the corresponding statistical fluctuations will be more pronounced and inevitably limit performance. The central question of this thesis is: as the size of the resonator becomes smaller, how stable

can the resonant frequency be? The answers to this seemingly simple question form the subject of phase noise of NEMS. We will review the pioneering work before going to this subject in detail.

1.2 Brownian Motion, Nyquist-Johnson Noise, and Fluctuation-Dissipation Theorem

A microscopic particle immersed in a liquid exhibits a random type of motion. This phenomenon is called Brownian motion and reveals clearly the statistical fluctuations that occur in a system in thermal equilibrium.[8] The Einstein relation, perhaps the most important result of the study of Brownian motion, states that the diffusion constant is proportional to the frictional coefficient determined by the hydrodynamic interaction of the particle with the viscous fluid.[12] The Brownian motion serves as a prototype problem whose analysis provides considerable insight into the mechanisms responsible for the existence of fluctuations and dissipation of energy. This problem is also of great practical interest because such fluctuations constitute a background of "noise" which imposes sensitivity limits on delicate physical measurements. For example, Nyquist-Johnson noise, which originates from thermal agitation of electrical charge in a conductor,[9,10] is present at any circuitry with nonzero dissipation, and in many cases determines the noise floor of an amplifier.[11] Nyquist's theorem states that the spectral density of the thermal fluctuating voltage of any electrical impedance is always proportional to the square root of its resistive part.[13] The same arguments used to study Brownian motion and Nyquist-Johnson noise can be extended on a more abstract level to a general result of wide applicability, the fluctuation-dissipation theorem.[12-14] The

fluctuation-dissipation theorem explicitly indicates how the cross-correlation functions of the fluctuating quantities are associated with the friction coefficients of the equations of motion, or equivalently, how the spectra of statistical fluctuations are related to the dissipations of the system near thermal equilibrium.

1.3 Noise in Microelectromechancial Systems and Nanoelectromechanical Systems

We now review the study of the noise of MEMS and NEMS, starting from the work in a liquid. Paul and Cross have considered the Brownian motion of NEMS cantilevers and concluded that the corresponding force sensitivities are in the range of piconewton.[15] Considering the hydrogen bond strength is ~10 pN, such sensitivities imply the possibility of using NEMS to sense biological forces at single molecule level. On the other hand, optical tweezers have recently led to quite spectacular measurements of small weak force, with the force sensitivities again limited by Brownian motion.[16] In this technique, an optical beam, focused to the diffraction limit, is employed. Functionalized dielectric beads, typically having diameters of ~1 μm, are attached to the biomolecules under study to provide a handle. In this way, direct measurements of piconetwon scale biological forces have been obtained.[18] In a more recent study, internal dynamics of DNA, yielding forces in the femtonewton range, have been observed via the two-point correlation technique.[17]

We now discuss the work on characterization the thermomechancial noise of MEMS and NEMS in vacuum. Albrecht et al. demonstrate frequency modulation detection using high Q cantilevers for enhanced force microscopy sensitivity, limited by

thermomechancial noise in vacuum.[19] Similarly, using a high *Q* single crystal silicon cantilever as thin as 60 nm, T. D. Stowe et al. have achieved attonewton force sensitivity at 4.8 K in vacuum.[5] Cooling down similar devices further to millikelvin temperatures, force sensitivity at subattonewton scale has also been demonstrated.[6] Such exquisite force sensitivities have ultimately led to the detection of single electron spin using magnetic resonance force microscopy (MRFM).[20]

The observation of thermomechancial noise of high frequency NEMS has been hindered, largely due to the diminishing transducer responsivity as the dimensions are reduced into the submicron range. This can only be circumvented by delicate incorporation of the actuator, transducer, and readout amplifier, all meticulously chosen and orchestrated to minimize the noise from these extrinsic elements. For example, the piezoresistors on NEMS silicon cantilevers, which acts as transducers upon current biasing, convert the mechanical displacement into a voltage signal, which is subsequently read out by a low noise amplifier. Using such a scheme, Arlett et al. have observed the theromomechanical noise down to cryogenic temperatures for NEMS devices with resonance frequencies of ~2 MHz.[22]

Another example is the nanomechanical parametric amplifier at 17 MHz by Harrington,[23] which is similar to the one demonstrated by Rugar and Grutter using a microscale cantilever.[21] Operating in degenerate mode, a parametric modulation of the beam's effective stiffness at twice the signal frequency is produced by the application of an alternating longitudinal force to both ends of a doubly clamped beam. At highest mechanical gains, noise matching performance is achieved, resulting in the observation of thermomechanical noise squeezing at cryogenic temperatures.

Finally, we mention the recent attempt to approach the quantum limit of a nanomechancial resonator by coupling a single electron transistor (SET) with a high *Q*, 19.7 MHz nanomechanical resonator by LeHaye et al.[24] At temperatures as low as 56 millikelvin, they observe thermomechanical noise corresponding to a quantum occupation number of 58, and demonstrate the near-ideal performance of the SET as a linear amplifier. This work clearly paves the feasible way to the quantum mechanical limits of NEMS, blurring the division between quantum optics and solid state physics.[2]

1.4 Phase Noise in Microelectromechancial Systems and Nanoelectromechanical Systems

We now review work on the phase noise of NEMS and MEMS. The phase noise of MEMS resonators was first analyzed by Vig and Kim.[25] They examine how frequency stabilities of MEMS and NEMS resonators scale with dimensions. When the dimensions of a resonator becomes small, instabilities that are negligible in macroscale devices become prominent. At submicron dimensions, the temperature fluctuation noise, adsorption-desorption noise, and thermomechanical noise are likely to limit the applications of ultra small resonators. Later, Cleland and Roukes develop a self-containing formalism to treat a similar list of noise sources and estimate their impact on a doubly clamped beam of single crystal silicon with a resonance frequency of 1 GHz.[26] Their calculation, however, does not agree with Vig and Kim's work in terms of the magnitude of the impact of the noise, as well as the method of analysis of some of the noise sources, in particular, that of the effect of temperature fluctuations. In analyzing the temperature fluctuation noise, they consider a more realistic thermal circuit by dividing

the device into sections, and show that the resulting Allan variance is of the same magnitude as that due to thermomechanical noise for the model resonator with Q of 10^4. This apparently contradicts the excessive temperature fluctuations predicted by Vig and Kim.[25] Moreover, they conclude that the noise performance, limited by the fundamental noise processes, can be comparable with their macroscale counterparts, the oven stabilized quartz crystal oscillators. By consolidating these studies, we first introduce the subject of phase noise in chapter 2, and then present the theory of the phase noise mechanisms affecting NEMS in chapter 3.

Except for the aforementioned theoretical works, very little experimental data are available for evaluating whether the calculated noise performance can be achieved. More systematic approaches, measuring the performance of high Q resonators operating in phase-locked loops, with controlled variations in temperature, environment, and materials, need to be followed. As an initial step into these efforts, we describe the implementations of phase-locked loops based on NEMS devices in chapter 4. We also report the observation of adsorption-desorption noise arising from xenon atoms adsorbed on the device surface. Our measurement results are in excellent agreement with the proposed idea gas model. More generally, our approach represents a canonical example on how to study the frequency stabilities arising from a particular noise process of interest.

1.5 Mass Sensing Based on Microelectromechanical Systems and Nanoelectromechancial Systems

We now review a separate, but closely related front: the inertial mass sensing based on MEMS and NEMS. Today mechanically based sensors are ubiquitous, having a long history of important applications in many diverse fields of science and technology. Among the most responsive sensors are those based on the acoustic vibratory modes of crystals,[27,28] thin films,[29] and more recently, MEMS[30,31] and NEMS.[7,32,] Three attributes of these devices establish their mass sensitivity: effective vibratory mass, quality factor, and resonant frequency. The miniscule mass, high *Q*, and high resonant frequency of NEMS provide them with unprecedented potential for mass sensing. Femtogram mass sensing using NEMS cantilevers has been demonstrated by Lavrik and Datskos by photothermally exciting silicon cantilevers in the range of 1 to 10 MHz and measuring a mass change of 5.5 fg upon chemisorption of 11-mercaptoundecanoic acid.[32] Ekinci and Roukes achieve attogram mass sensing by exposing NEMS devices with Au atomic flux and tracking the resulting frequency shift in a phase-locked loop.[33] Motivated by these experiments, we start to examine theoretically the ultimate limits of inertial mass sensing based upon NEMS devices as a result of fundamental noise processes.[7] We present the resulting theoretical analysis in chapter 3. The conclusion is quite compelling: it indicates that NEMS devices can directly "weigh" individual intact, electrically neutral, molecules with single Dalton sensitivities.

As an initial step toward this goal, we present our mass sensing experiments at zeptogram scale in chapter 4. This is demonstrated by depositing xenon atoms and nitrogen molecules on the NEMS device, and tracking the resulting frequency shift in

high precision phase-locked loop. But more importantly, the agreement of our experimental results with the theory justifies our formalism and validates its use to delineate, for the first time, the feasible pathway into single Dalton sensitivity.

1.6 Organization

To help the reader understand this work in a more coherent and clear way, this thesis is organized in the following way:

Chapter 2 introduces the subject of phase noise and serves as the mathematical foundation of this work. We first describe how phase fluctuations of an oscillator convert to the noise sideband of the carrier. We then define the phase noise, the frequency noise, and Allan deviation, emphasizing their relationship with each other. As an example, Leeson's model is described and used to analyze the thermal noise of an ideal linear LC oscillator.

Chapter 3 discusses the phase noise mechanism of the NEMS resonators. We first examine fundamental noise processes, including thermomechancial noise, momentum exchange noise, adsorption-desorption noise, diffusion noise, and temperature fluctuation noise. We also discuss nonfundamental noise processes arising from the Nyquist-Johnson noise of the transducer amplifier implementations. For each noise process presented here, we give expressions for the phase noise spectra and Allan deviation and then translate them into the corresponding minimum measurable frequency shift and mass sensitivity in light of their importance in sensing applications.

Chapter 4 presents the experimental measurement of the phase noise of NEMS. First, we first analyze the control servo behavior of the phase-locked loops and give the

detailed implementations together with their noise performance. The achieved noise performance is compared to the local oscillator (LO) requirements of chip scale atomic clocks (CSAC) to evaluate the viability of NEMS based oscillators for this application. Finally, we investigate the diffusion noise arising from adsorbed xenon atoms by putting a very high frequency NEMS into the phase-locked loop and measuring the frequency noise spectra and Allan deviation.

Chapter 5 shows very high frequency NEMS that provide a profound sensitivity increase for inertial mass sensing into zeptogram scale. We demonstrate *real time*, *in situ* mass detection of sequential pulses of ~100 zg nitrogen molecules by tracking resulting frequency shift. Measurement and analysis from our experiments demonstrate mass sensitivities at the level of ~7 zg, the mass of an individual 4 kDa molecule, or ~30 xenon atoms.

Chapter 6 describes a surface nanomachining process that involves electron beam lithography, followed by dry anisotropic and selective electron cyclotron resonance plasma etching steps. Measurements on a representative family of the resulting devices demonstrate that, for a given geometry, nanometer-scale SiC resonators are capable of yielding substantially higher frequencies than GaAs and Si resonators.

Chapter 7 describes a broadband radio frequency balanced bridge technique for electronic detection of displacement in NEMS. The effectiveness of the technique is demonstrated by detecting the minute electromechanical impedances of NEMS embedded in large electrical impedances at very high frequencies.

References

1. M. L. Roukes Plenty of room indeed. *Sci. Am.* **285**, 48 (2001).

2. M. L. Roukes Nanoelectromechanical Systems. *Technical Digest, Solid State Sensor and Actuator Workshop, Hilton Head Island, South Carolina (June4–8, 2000)* 367–376 (2000).

3. X. M. H. Huang, C. A. Zorman, M. Mehregany, and M. L. Roukes Nanodevices motion at microwave frequencies. *Nature* **421**, 496 (2003).

4. A. N. Cleland and M. L. Roukes Fabrication of high frequency nanometer scale mechanical resonators from bulk Si crystals *Appl. Phys. Lett.* **69**, 2653 (1996).

5. T. D. Stowe, K. Yasumura, T.W. Kenny, D. Botkin, K. Wago, and D. Rugar Attonewton force detection using ultrathin silicon cantilevers. *Appl. Phys. Lett.* **71**, 288 (1997).

6. H. J. Mamin and D. Rugar Sub-attonewton force detection at milikelvins. *Appl. Phys. Lett.* **79**, 3358 (2001).

7. K. L. Ekinci, Y. T. Yang, and M. L. Roukes Ultimate limits to inertial mass sensing based upon Nanoelectomechancial systems *J. Appl. Phys*. **95**, 2682 (2004).

8. A. Einstein *Investigation on the Theory of the Brownian Movement* (New York, Dover, 1956).

9. H. Nyquist Thermal agitation of electrical charge in conductors. *Phys. Rev.* **32**, 110 (1928).

10. J. B. Johnson Thermal agitation of electricity in conductors. *Phys. Rev.* **32**, 97 (1928).

11. P. R. Grey and R. G. Meyer *Analysis and Design of Analog Integrated Circuits* (New York, John Wiley & Sons, 1984).

12. P. M. Chaikin and T. C. Lubensky *Principles of Condensed Matter Physics* (New York, Cambridge University Press, 1995).

13. F. Reif *Fundamentals of Statistical and Thermal Physics* (Singapore, McGraw-Hill, 1996).

14. L. D. Landau and E. M. Lifshitz *Statistical Physics* (London, Oxford, 1980).

15. M. R. Paul and M. C. Cross Stochastic dynamics of nanoscale mechanical oscillators immersed in a viscous fluid. *Phys. Rev. Lett.* **92**, 235502-1, (2004).

16. J. C. Crocker Measurement of the hydrodynamic corrections to the Brownian motion of two colloidal spheres. *J. Chem. Phys.* **106**, 2837 (1997).

17. J. C. Meiners and S. R. Quake Femtonewton force spectroscopy of single extended DNA molecules. *Phys. Rev. Lett.* **84**, 5014 (2000).

18. K. Visscher, M. J. Schnitzer and S. M. Block Kinesin motors studied an optical force clamp. *Biophysical Journ.* **74**, A49 (1998).

19. T. R. Albrecht, P. Grutter, D. Horne, and D. Rugar Frequency modulation detection using high Q cantilever for enhanced force microscopy sensitivity *J. Appl. Phys.* **69**, 668 (1991).

20. D. Rugar, R. Budakian, H. J. Mamin, and B. W. Chui Single spin detection by magnetic resonance force microscope. *Nature* **430**, 329 (2004).

21. D. Rugar and P. Grutter Mechanical parametric amplification and thermomechanical noise squeezing. *Phys Rev. Lett.* **67**, 699 (1991).

22. J. L. Arlett, J. R. Maloney, B. Gudlewski, M. Muluneh, and M. L. Roukes Self-sensing micro- and nanocantilevers with attonewton-scale force resolution. *Nano Lett.* **6**, 1001, (2006).

23. D. A. Harrington Physics and applications of nanoelectromechanical systems (NEMS). PhD thesis, California Institute of Technology (2003).

24. M. D. LaHaye, O. Buu, B. Camarota, and K. C. Schwab Approaching the quantum limit of a nanomechanical resonator. *Science* **304**, 74 (2004).

25. J. Vig and Y. Kim Noise in microelectromechanical system resonators *IEEE Trans. on Ultrasonics, Ferroelectronics and Frequency Control* **46**, 1558 (1999).

26. A. N. Cleland and M. L. Roukes Noise processes in nanomechanical resonators. *J. Appl. Phys.* **92**, 2758 (2002).

27. D. S. Ballantine et al. *Acoustic Wave Sensors* (San Diego, Academic Press, 1997).

28. C. Lu *Application of Piezoelectric Quartz Crystal Microbalance* (London, Elsevier, 1984).

29. M. Thompson and D. C. Stone *Surface-Launched Acoustic Wave Sensors: Chemical Sensing and Thin Film Characterization* (New York, John Wiley and Sons, 1997).

30. J. Thundat, E. A. Wachter, S. L. Sharp, and R. J. Warmack Detection of mercury vapor using resonating microcantilevers. *Appl. Phys. Lett.* **66**, 1695-1697(1995).

31. Z. J. Davis, G. Abadal, O. Kuhn, O. Hansen, F. Grey, and A. Boisen Fabrication and characterization of nanoresonting devices for mass detection. *J. Vac. Sci. Technol.* **B 18**, 612-616(2000).

32. N. V. Lavrik and P. G. Datskos Femtogram mass detection using photothermally actuated nanomechanical resonators. *Appl. Phys. Lett* **82**, 2697 (2003).

Chapter 2

Introduction to Phase Noise

A brief introduction into the subject of phase noise is given here. We first describe the conversion of the phase fluctuations into the noise sideband of the carrier. We then define phase noise, frequency noise, and Allan deviation with emphasis on their relationship with each other. Leeson's model is described and used to analyze the thermal noise of an ideal, linear LC oscillator. Finally, we give the general expression of the minimum measurable frequency shift in a noisy system.

2.1 Introduction

In general, circuit and device noise can perturb both the amplitude and phase of an oscillator's output.[1,2] Of necessity, all practical oscillators inherently possess an amplitude limiting mechanism of some kind. Because the amplitude fluctuations are attenuated, phase noise generally dominates. We will primarily focus on phase noise in our theoretical exposition and divide the theoretical investigation into two parts. The first part is the general conceptual foundation on how the frequency stability of an oscillator should be characterized, more commonly known as the subject of phase noise. The second part is the exposition on the *physical* phase noise mechanisms affecting NEMS devices. In this chapter, we will deal with the first part and defer the second part to chapter 3. We will also describe Leeson's model to analyze the thermal noise of an ideal, linear LC oscillator. Finally, we will give expressions translating the frequency noise into the minimum measurable frequency shift in a noisy system.

2.2 General Remark

The output of an oscillator of angular frequency ω_C is generally given by

$$X(t) = X_0(1 + A(t))f[\omega_C t + \phi(t)]. \tag{2.1}$$

Here $\phi(t)$ and $A(t)$ are functions of time and f is a periodic function. Here X can be the output voltage from an electrical oscillator or the displacement of a mechanical oscillator. The output spectrum contains higher harmonics of ω_C if the waveform is not sinusoidal. For our purpose, we assume no higher harmonics from any nonlinearity of the devices or the circuits, and thus the output $X(t)$ is purely sinusoidal. For a sinusoidal oscillation, the output is given by

$$X(t) = X_0(1 + A(t))\sin[\omega_C t + \phi(t)]\,. \tag{2.2}$$

2.3 Phase Noise

The physical fluctuations in the oscillator can perturb the phase of the oscillation and produce phase fluctuations. We now describe how then phase fluctuations are converted into noise sidebands around the carrier. Considering a small phase variation $\phi(t) = \phi_0 \sin \omega t$, equation (2.2) can be expanded as

$$\begin{aligned} X(t) &= X_0(1 + A(t))\sin(\omega_C t + \phi_0 \sin \omega t + \theta) \\ &= X_0 \sin(\omega_C t + \theta) + X_0 \frac{\phi_0}{2}\sin[(\omega_C + \omega)t] - X_0 \frac{\phi_0}{2}\sin[(\omega_C - \omega)t]. \end{aligned} \tag{2.3}$$

The phase variation generates two sidebands spaced $\pm\omega$ from the carrier with amplitude $X_0\phi_0$ / 2. The upper sideband is phase-coherent with the lower sideband with the opposite sign. The generated sideband is characterized in the following definition: it is conventionally given by the ratio of noise power to carrier power for 1 Hz bandwidth with offset frequency from the carrier. In notation, the definition is given by

$$L_{total}(\omega) = 10\log\left(\frac{P_{sideband}(\omega_C + \omega, 1Hz)}{P_C}\right). \tag{2.4}$$

P_C is the carrier power and $P_{sidebank}(\omega_C + \omega, 1Hz)$ is the single sideband power at a frequency offset ω from the carrier frequency ω_C with the measurement bandwidth of 1 Hz as shown in figure 2.1. $L_{total}(\omega)$ is thus in units of decibel referred to the carrier power per hertz (dBc/Hz).

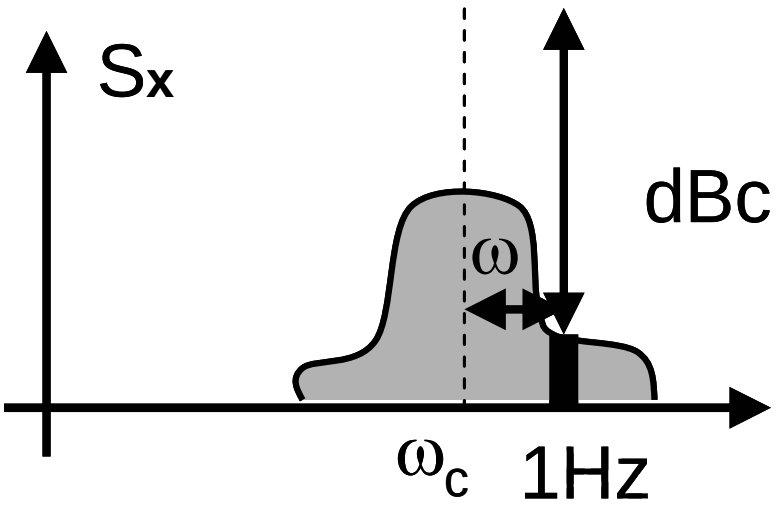

Figure 2.1. Definition of phase noise. The phase noise is conventionally expressed as the ratio of sideband noise power for 1 Hz bandwidth to the carrier power in units of dBc/Hz.

2.4 Frequency Noise

Phase is the integration of frequency over time, i.e.,

$$\phi(t) = \int_{-\infty}^{t} \omega(\tau) d\tau \,. \tag{2.5}$$

Conversely, frequency is the derivative of phase with respect to time, i.e.,

$$\omega(t) = \frac{d\phi}{dt} \,. \tag{2.6}$$

The spectral density of the phase noise is thus related to the spectral density of the frequency noise by

$$S_{\phi}(\omega) = \frac{1}{\omega^2} S_{\omega}(\omega) \,. \tag{2.7}$$

In addition to angular frequency, we introduce another commonly used quantity, fractional frequency, defined as ratio of frequency to carrier frequency.

$$y = \frac{\delta\omega}{\omega_C} \,. \tag{2.8}$$

The spectral density of fractional frequency is related to the spectral density of frequency by

$$S_y(\omega) = \frac{1}{\omega_C^2} S_{\omega}(\omega) \,. \tag{2.9}$$

The resonance frequency depends on many physical parameters of the resonator. The fluctuations of these parameters can translate into fractional frequency noise. The fractional noise is related to the fluctuation of the corresponding parameter by

$$S_y(\omega) = \left(\frac{\partial y}{\partial \chi} \right)^2 S_{\chi} \,. \tag{2.10}$$

χ is the physical parameter which the resonant frequency is dependent on. For example, if χ is the temperature T of the device, $\partial y / \partial T$ is simply the temperature coefficient of the resonant frequency.

2.5 Allan Variance and Allan Deviation

Allan variance is a quantity commonly used by the frequency standard community to compare the frequency stabilities of different oscillators. The phase and frequency noise are defined in the frequency domain; the Allan deviation is defined in the time domain. Allan deviation, $\sigma_A(\tau_A)$, is simply the square root of Allan variance, $\sigma_A^2(\tau_A)$. The defining expression of the Allan deviation is given by[1,3]

$$\sigma_A^2(\tau_A) = \frac{1}{2f_C^2}\frac{1}{N-1}\sum_{m=2}^{N_S}(\bar{f}_m - \bar{f}_{m-1})^2 . \tag{2.11}$$

$\bar{f}_m$ is the average frequency measured over the mth interval with zero dead time and N_S is the sample number. From this definition, the Allan deviation is related to the phase noise density by

$$\sigma_A^2(\tau_A) = 2\left(\frac{2}{\omega\tau_A}\right)^2 \int_0^\infty S_\phi(\omega)\sin^4(\omega\tau_A/2)d\omega . \tag{2.12}$$

In the experimental data, Allan deviation is usually presented with the error bar given by one standard deviation confidence interval (or 68% confidence interval), i.e., $\sigma_A / \sqrt{N_S - 1}$. For example, for sample number N_S=101, the one standard deviation confidence interval is 10% of the Allan deviation.

The noise spectra with different power laws are commonly used so we give the formulas of the corresponding Allan deviations. For phase noise having $1/f^4$ component, i.e., $S_\phi(\omega) = C_4(\omega_C/\omega)^4$, the Allan deviation is given by

$$\sigma_A(\tau_A) = \sqrt{\frac{\pi}{3} C_4 \omega_C^2 \tau_A} \,. \tag{2.13}$$

For phase noise having $1/f^3$ component, i.e., $S_\phi(\omega) = C_3(\omega_C/\omega)^3$, the Allan deviation is given by

$$\sigma_A(\tau_A) = \sqrt{2\log_e 2 C_3 \omega_C} \,. \tag{2.14}$$

For phase noise having $1/f^2$ component, i.e., $S_\phi(\omega) = C_2(\omega_C/\omega)^2$, the Allan deviation is given by

$$\sigma_A(\tau_A) = \sqrt{\frac{\pi C_2}{\tau_A}} \,. \tag{2.15}$$

For the fractional frequency noise having the Lorentizian function form, i.e., $S_y(\omega) = A/(1+(\omega\tau_r)^2)$, the spectral density of phase noise is given by $S_\phi(\omega) = A(\omega_C/\omega)^2/(1+(\omega\tau_r)^2)$. Upon integration, the Allan deviation is given by

$$\sigma_A(\tau_A) = \sqrt{\frac{A}{2\pi} F(\frac{\tau_r}{\tau_A})} \,. \tag{2.16}$$

$F(x)$ is an analytic function defined by

$$F(x) = \frac{1}{x^2}\int_0^\infty \frac{\sin^4(\xi x/2)d\xi}{\xi^2(1+\xi^2)} = \frac{1}{2x} - \frac{1}{x^2}[(1-e^{-x}) - \frac{1}{4}(1-e^{-2x})]. \tag{2.17}$$

As shown in figure 2.2, $F(x)$ reaches a maximum at x=1.89 with the value 0.095. The asymptotic expressions of $F(x)$ are $F(x) = \frac{1}{2x}$ for x>>1 and $F(x) = \frac{1}{6}x$ for x <<1.

These behaviors can also be clearly seen in figure 2.2. In the limit $\tau_r << \tau_A$, equation (2.16) becomes

$$\sigma_A(\tau_A) = \sqrt{\frac{A\tau_r}{4\pi\tau_A}}. \tag{2.18}$$

In the other limit $\tau_A << \tau_r$, equation (2.16) becomes

$$\sigma_A(\tau_A) = \sqrt{\frac{A\tau_A}{12\pi\tau_r}}. \tag{2.19}$$

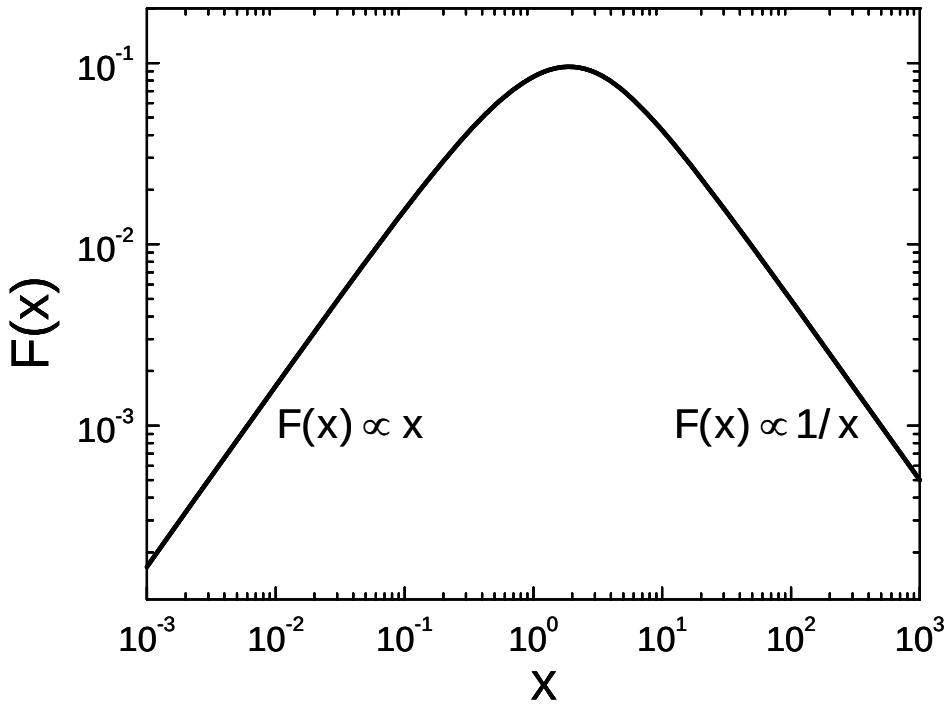

Figure 2.2. Plot of the function *F*(*x*). $F(x)$ shows the dependence of Allan deviation, having frequency noise density of Lorentzian form, on the ratio of the correlation time τ_r to the averaging time τ_A. $F(x)$ reaches a maximum at x=1.85 with the value 0.095. Its asymptotic behaviors for x <<1 and for x>>1 are also shown.

2.6 Thermal Noise of an Ideal Linear LC Oscillator

The phase noise of an ideal linear LC oscillator due to the Nyquist-Johnson noise is analyzed by Leeson.[4] Figure 2.3 shows that the Nyquist-Johnson noise source associated with the resistor injects noise current into a LC tank circuit. The impedance of the LC tank with a quality factor Q and the resonant frequency ω_0 at offset frequency ω ($\omega << \omega_0$) is given by

$$Z(\omega_0 + \omega) = \frac{1}{G} \frac{1}{1 + j2Q \frac{\omega}{\omega_0}}. \tag{2.20}$$

To sustain oscillation, the active device must compensate the energy dissipation by positive feedback. Therefore, the active device behaves as a negative conductance $-G$. For steady state oscillation, the impedance of the oscillator model is given by

$$Z(\omega) = \frac{v_{out}(\omega_0 + \omega)}{i_{in}(\omega_0 + \omega)} = -j \frac{1}{G} \frac{\omega_0}{2Q\omega}. \tag{2.21}$$

The total equivalent parallel resistance of the tank has an equivalent mean square noise current density of $i_{in}^2 / \Delta f = 4k_B TG$. Using this effective current power, the phase noise can be calculated as

$$S_\phi(\omega) = \frac{v_{noise}^2}{v_{signal}^2} = \frac{\frac{1}{2}|Z(\omega)|^2 i_{in}^2 / \Delta f}{\frac{1}{2} V_o^2} = \frac{k_B T}{2P_C Q^2} \left(\frac{\omega_0}{\omega} \right)^2. \tag{2.22}$$

P_C is the carrier power usually limited by saturation or nonlinearity of the active device. The Leeson model demonstrates explicitly the conversion of the current noise into sideband and explains the $1/\omega^2$ dependence of the phase noise density. Upon integration of the spectral density, we obtain the expression for the Allan deviation.

$$\sigma_A(\tau_A) = \sqrt{\frac{k_B T}{P_C} \frac{1}{Q^2 \tau_A}} \,. \tag{2.23}$$

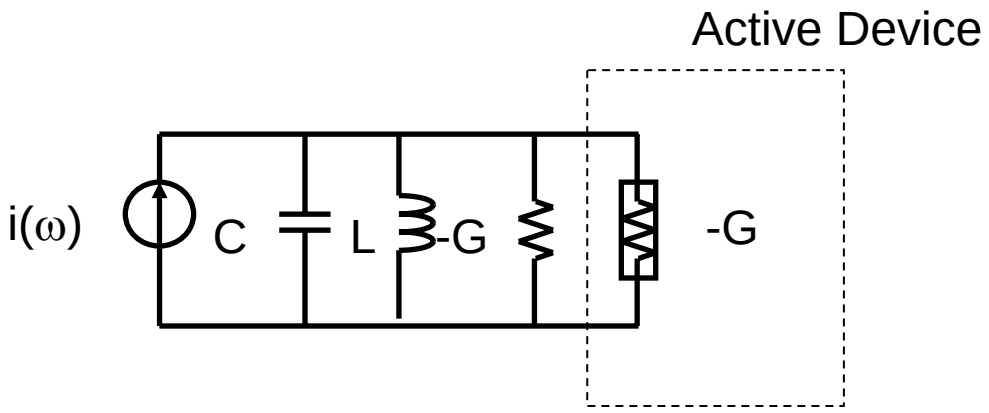

Figure 2.3. Leeson's model of phase noise for an ideal linear LC oscillator.
Equivalent one-port circuit for phase noise calculation for an ideal linear LC oscillator is used in the model. The Nyquist-Johnson noise source associated with the resistor injects noise current in LC tank, producing the noise sideband around the carrier. Note that the active device, compensating the energy dissipation from the resistor, is modeled as a negative conductance.

2.7 Minimum Measurable Frequency Shift

Experimentally we measure the change in physical properties of the resonator by detecting the corresponding frequency shift and thus an important question needs to be addressed:what is the minimum measurable frequency shift, $\delta\omega_0$, that can be resolved in a (realistic) noisy system? In principle, a shift comparable to the mean square noise (the spread) in an ensemble average of a series of frequency measurements should be resolvable, i.e., $\delta\omega_0 \approx \frac{1}{N}\sqrt{\sum_{i=1}^{N}(\omega_i - \omega_0)^2}$ for signal-to-noise ratio equal to unity. An estimate for $\delta\omega_0$ can be obtained by integrating the weighted effective spectral density of the frequency fluctuations, $S_\omega(\omega)$, by the normalized transfer function of the measurement loop, $H(\omega)$:

$$\delta\omega_0 \approx [\int_0^\infty S_\omega(\omega)H(\omega)d\omega]^{1/2}. \tag{2.24}$$

Here, $S_\omega(\omega)$ is in units of $(rad/s^2)/(rad/s)$. We can further simplify equation (2.24) by replacing $H(\omega)$ with the square transfer function $H'(\omega)$, which has the same integrated spectral weight, but is non-zero only within the passband delineated by $2\pi\Delta f$. Here, $\Delta f \approx 2\pi/\tau$ and is dependent upon the measurement averaging time, τ. Given this assumption, equation (2.24) takes the simpler, more familiar form.

$$\delta\omega_0 \approx [\int_0^{2\pi\Delta f} S_\omega(\omega)d\omega]^{1/2}. \tag{2.25}$$

This, of course, is an approximation to a real system — albeit a good one. If necessary, one can resort to the more accurate expression, equation (2.24).

2.8 Conclusion

We describe the conversion of phase fluctuations into the noise sideband of the carrier and present the definitions of phase noise, frequency noise, and Allan deviation, all commonly used to characterize the frequency stability of an oscillator. Figure 2.4 summarizes the relation between these quantities. We illustrate these definitions by analyzing the phase noise of an ideal, linear LC oscillator in the context of Leeson's model. In particular, Leeson's model explicitly demonstrates how the Nyquist-Johnson current noise produces noise sideband of carrier and explains the $1/\omega^2$ dependence of the phase noise density on the offset frequency. Finally, we give the expressions for the minimum measurable frequency shift in a noisy system for sensing applications involving oscillators.

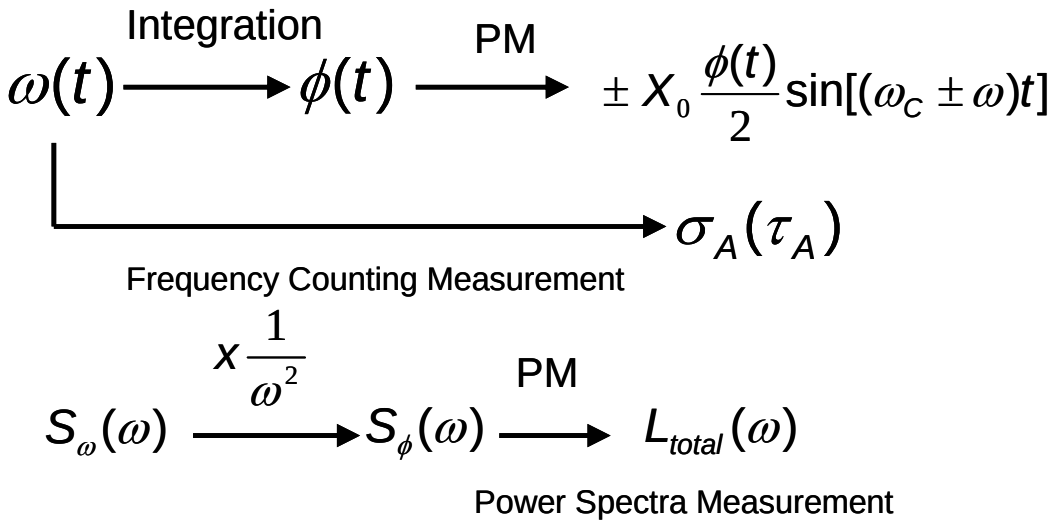

Figure 2.4. Summary of the relation between different quantities. In time domain, the phase variation $\phi(t)$, which is the integration of angular frequency variation $\omega(t)$, generates the sidebands $\pm x_0(\phi(t)/2)\sin[(\omega_c \pm \omega)t]$ through phase modulation (PM). The Allan deviation can be calculated with the frequency data from the frequency counting measurements. In the frequency domain, the frequency noise density $S_\omega(\omega)$ is related to the phase noise density $S_\phi(\omega)$ by $S_\phi(\omega) = 1/\omega^2 S_\omega(\omega)$. The noise sideband of the carrier is characterized by $L_{total}(\omega)$, which can be obtained from the power spectrum measurement.

References

1. A. N. Cleland and M. L. Roukes Noise processes in nanomechanical resonators. *J. Appl. Phys.* **92**, 2758 (2002).

2. A. Hajimiri and T. H. Lee *The design of low noise oscillator* (Norwell, Kluwer Academic Publisher, 1999).

3. D. W. Allan Statistics of atomic frequency standard. *Proc. IEEE* **54**, 221 (1966).

4. D. B Leeson A simple model of feedback oscillator noise spectrum. *Proc. IEEE* **54**, 329 (1996).

Chapter 3

Theory of Phase Noise Mechanism of NEMS

We present the theory of phase noise mechanism of NEMS. We examine both fundamental and nonfundamental noise processes to obtain expressons for phase noise density, Allan deviation, and mass sensitivity. Fundamental noise processes considered here include thermomechanical noise, momentum exchange noise, adsorption-desorption noise, diffusion noise, and temperature fluctuation noise. For nonfundamental noise processes, we develop a formalism to consider the Nyquist-Johnson noise from transducer amplifier implementations. The detailed analysis here not only reveals the achievable frequency stability of NEMS devices, but also provides a theoretical framework to fully optimize noise performance and the mass sensitivity for sensing applications.

3.1 Introduction

So far we have considered how physical fluctuations convert into the noise sidebands of the carrier and give the conventional definition of phase noise, frequency noise, and Allan deviation, all commonly used to characterize the frequency stability of an oscillator. Here we proceed to investigate phase noise mechanisms affecting NEMS devices. First, we examine the *fundamental* noise processes intrinsic to NEMS devices.[1-3] We begin our discussion from thermomechanical noise, originating from thermally driven random motion of the resonator, by considering the thermal fluctuating force acting on the resonator. We then consider momentum exchange noise, adsorption-desorption noise, and diffusion noise, all arising from gaseous molecules in resonator surroundings. The impinging gaseous molecules can impart momentum randomly to a NEMS device and induce momentum exchange noise. Moreover, when gaseous species adsorb on a NEMS device, typically from the surrounding environment, they can diffuse along the surface in and out of the device and produce diffusion noise. Meanwhile, they can also briefly reside on the surface and then desorb again and generate adsorption-desorption noise. We also discuss the noise due to the temperature fluctuations; these fluctuations are fundamental to any object with finite thermal conductance and are distinct from environmental drifts that can be controlled using oven-heated packaging, similar to that used for high precision quartz clocks.

Note that the thermomechanical noise from the internal loss mechanism in the resonator and the momentum exchange noise from gaseous damping are dissipation-induced fluctuations. They are expected for mechanical resonators with nonzero dissipation according to the fluctuation-dissipation theorem.[4] Other noise sources

including adsorption-desorption noise, diffusion noise, and temperature fluctuation noise are parametric noise. These have to do with parametric changes in the physical properties of the resonator such as device mass and temperature, which cause the natural resonance frequency of the resonator to change, but do not necessarily involve energy dissipation, leaving the quality factor unchanged.[1]

Finally, we consider the nonfundamental noise processes from the readout circuitry of transducer implementations.[5] In general, the NEMS transducers covert mechanical displacement into an electrical signal, which is subsequently amplified to the desired level by an amplifier for readout. Hence both the transducer and amplifier can add extrinsic noise to the NEMS devices, and the impact on frequency fluctuations is treated by our formalism developed here. Our formalism will reveal the resulting impact on the frequency fluctuations and enable the optimization of noise performance. Although we focus our discussion on the Nyquist-Johnson noise from the transducer and readout amplifier implementations, it can be readily generalized to incorporate other types of extrinsic noise such as flicker noise.

In conjunction with the discussion of each noise process, we also give the expression for the corresponding mass sensitivity limit. In general, resonant mass sensing is performed by carefully determining the resonance frequency ω_0 of the resonator and then, by looking for a frequency shift in the steady state due to the accreted mass. Therefore, the minimum measurable frequency shift, $\delta\omega_0$, will translate into the minimum measurable mass, δM, referred to as the mass sensitivity, δM. Henceforth, we model the resonator as a one-dimensional simple harmonic oscillator characterized by the

effective mass M_{eff} and the dynamic stiffness $\kappa_{eff} = M_{eff}\omega_0^2$.[6] Assuming that δM is a small fraction of M_{eff}, we can write a linearized expression

$$\delta M \approx \frac{\partial M_{eff}}{\partial \omega_0}\delta\omega_0 = \Re^{-1}\delta\omega_0 . \tag{3.1}$$

This expression assumes that the modal quality factor and compliance are not appreciably affected by the accreted species. This is consistent with the aforementioned presumption that $\delta M << M_{eff}$. Apparently, δM critically depends on the minimum measurable frequency shift $\delta\omega_0$ and the inverse mass responsivity $\Re^{-1}$. Since κ_{eff} for the employed resonant mode—a function of the resonator's elastic properties and geometry—is unaffected by small mass changes, we can further determine that

$$\Re = \frac{\partial \omega_0}{\partial M_{eff}} = -\frac{\omega_0}{2M_{eff}}, \tag{3.2}$$

$$\delta M \approx -2\frac{M_{eff}}{\omega_0}\delta\omega_0 . \tag{3.3}$$

We note that equation (3.3) is analogous to the Sauerbrey equation,[7] but is instead here written in terms of the absolute mass, rather than the mass density, of the accreted species. Both fundamental and nonfundamental noise processes will impose limits on $\delta\omega_0$, and therefore on δM. For each noise process, we will integrate phase noise density to obtain the expression for $\delta\omega_0$ by using equation (2.25) and translate it into δM using equation (3.3).[3]

3.2 Thermomechanical Noise

We now consider the thermomechanical noise, originating from thermally driven random motion of NEMS devices.[1-3] For the one-dimensional simple harmonic oscillator, the mean square displacement fluctuations of the center of mass, $\langle x_{th} \rangle$, satisfy $M_{eff}\,\omega_0{}^2 \langle x_{th}{}^2 \rangle / 2 = k_B T / 2$. Here, k_B is Boltzmann's constant and T is the resonator temperature. The spectral density of these random displacements, $S_x(\omega)$, (with units of m^2/Hz) is given by

$$S_x(\omega) = \frac{1}{M_{eff}{}^2} \frac{S_F(\omega)}{(\omega^2 - \omega_0{}^2)^2 + \omega^2 \omega_0{}^2 / Q^2}. \tag{3.4}$$

The thermomechanical force spectral density in units of N^2/Hz has a white spectrum $S_F(\omega) = 4 M_{eff}\,\omega_0 k_B T / Q$. For $\omega >> \omega_0 / Q$, the phase noise density is given by the expression[1]

$$S_\phi(\omega) = \frac{1}{2} \frac{S_x(\omega)}{|x_C|^2} = \frac{k_B T}{8\pi P_C} \left(\frac{\omega_0}{\omega} \right)^2. \tag{3.5}$$

P_C is the maximum carrier power, limited by onset of non-linearity of mechanical vibration of the NEMS. For a doubly clamped beam with rectangular cross section driven into flexural resonance, the non-linearity results from Duffing instability and the maximum carrier power can be estimated by $P_C = \omega_0 E_C / Q = M_{eff}\,\omega_0^3 |x_C|^2 / Q$ with critical amplitude $|x_C|$ given by $t / \sqrt{Q(1-\nu^2)}$ for doubly clamped beams.[8] t is the dimension of the beam in the direction of transverse vibration; ν is the Poisson ratio of the beam material.[9]

Upon direct integration of the spectral density, Allan deviation is given by

$$\sigma_A(\tau_A) = \sqrt{\frac{k_B T}{8 P_C Q^2 \tau_A}}\,. \tag{3.6}$$

We can rewrite this expression in terms of the ratio of the maximum drive (carrier) energy, $E_C = M_{eff}\omega_0^{\,2}\left|x_C\right|^2$, to the thermal energy, $E_{th} = k_B T$, representing the effective dynamic range intrinsic to the device itself. This is the signal-to-noise ratio (SNR) available for resolving the coherent oscillatory response above the thermal displacement fluctuations. We can express this dynamic range, as is customary, by $DR(dB) = 10\log(E_C / k_B T)$ in units of decibels. This yields a very simple expression

$$\sigma_A(\tau_A) = (1/\tau_A Q\omega_0)^{1/2} 10^{-DR/20}. \tag{3.7}$$

We now turn to the evaluation of the minimum measurable frequency shift, $\delta\omega_0$, limited by thermomechanical fluctuations of a NEMS resonator. To obtain $\delta\omega_0$, the integral in equation (2.25) must be evaluated using the expression for $S_\omega(\omega)$ given in equation (3.5) over the effective measurement bandwidth. Performing this integration for the case where $Q>>1$ and $2\pi\Delta f << \omega_0 / Q$, we obtain:

$$\delta\omega_0 \approx \left[\frac{k_B T}{E_C}\frac{\omega_0 \Delta f}{Q}\right]^{1/2}, \tag{3.8}$$

$$\delta M \approx 2M_{eff}\left(\frac{E_{th}}{E_c}\right)^{1/2}\left(\frac{\Delta f}{Q\omega_0}\right)^{1/2}. \tag{3.9}$$

We can also recast equation (3.9) in terms of dynamic range *DR* and mass responsivity $\Re$ as

$$\delta M \approx \frac{1}{\Re}\left(\Delta f\,\frac{\omega_0}{Q}\right)^{1/2} 10^{(-DR/20)}. \tag{3.10}$$

Note that Q/ω_0 is the open-loop response (ring-down) time of the resonator. In table 3.1, we have translated these analytical results from equation (3.7) and equation (3.9) into

concrete numerical estimates for representative realizable device configurations. We list the Allan deviation σ_A (for averaging time τ_A=1 sec) and the mass sensitivity δM (for measurement bandwidth Δf =1 kHz), limited by thermomechancial noise, for three representative device configurations with quality factor Q=10^4. For the calculation of resonant frequency, we assume Young's modulus E =169 GPa and mass density ρ =2.33 g/cm^3 for the silicon beam and silicon nanowire and E = 1 TPa and ρ = 1g/cm^3 for the single walled nanotube (SWNT). First, a large dynamic range is always desirable for obtaining frequency stability in the case of thermomechanical noise. Clearly, as the device sizes are scaled downward while maintaining high resonance frequencies, M_{eff} and κ_{eff} must shrink in direct proportion. Devices with small stiffness (high compliance) are more susceptible to thermal fluctuations and consequently, the dynamic range becomes reduced. Second, the values of the mass sensitivity span only the regime from a few tenths to a few tens of Daltons. This is the mass range for a small *individual* molecule or atom; hence it is clear that nanomechanical mass sensors offer unprecedented ability to *weigh* individual neutral molecules or atoms and will find many interesting applications in mass spectrometry and atomic physics.[10,11]

Device	Frequency	Dimensions ($L \times w \times t$)	M_{eff}	DR	σ_A (1sec)	δM (1kHz)
Si beam	1 GHz	660 nm × 50 nm × 50 nm	2.8 fg	66 dB	3.2×10^{-10}	7.0 Da
Si nanowire	7.7 GHz	100 nm × 10 nm × 10 nm	17 ag	47 dB	9.5×10^{-10}	0.13 Da
SWNT	10 GHz	56 nm × 1.2 nm(dia.)	165 ag	14 dB	7.4×10^{-8}	0.05 Da

Table 3.1. Allan deviation and mass sensitivity limited by thermomechanical noise for representative realizable NEMS device configurations

3.3 Momentum Exchange Noise

We now turn to a discussion of the consequences of momentum exchange in a gaseous environment between the NEMS resonator and the gas molecules that impinge upon it. Gerlach first investigated the effect of a rarefied gas surrounding a resonant torsional mirror.[12] Subsequently, Uhlenbeck and Goudmit calculated the spectral density of the fluctuating force acting upon the mirror due to these random collisions.[13] Following these analyses, Ekinci et al. have obtained the mass sensitivity of the NEMS limited by momentum exchange noise.[3] Here we reproduce a similar version of their discussions. In the molecular regime at low pressure, the resonator's equation of motion is given by

$$M_{eff}\ddot{x}+\left(M_{eff}\frac{\omega_0}{Q_i}+\frac{pA_D}{v}\right)\dot{x}+M_{eff}\omega_0^2 x=F(t). \tag{3.11}$$

The $(M_{eff}\omega_0/Q_i)\dot{x}$ term results from the intrinsic loss mechanism. The term $(pA_D/v)\dot{x}$ represents the drag force due to the gas molecules. P is the pressure, A_D is the device surface area, and $v=\sqrt{k_BT/m}$ is the thermal velocity of gas molecule. The quality factor due to gas dissipation can be defined as $Q_{gas}=MvPA_D$. The loaded quality factor Q_L, as a result of two dissipation mechanisms, can be defined as $Q_L^{-1}=Q_i^{-1}+Q_{gas}^{-1}$. Since we have treated the thermomechanical noise from the intrinsic loss mechanism, we assume that $Q_i >> Q_{gas}$ and focus on the noise from gaseous damping. The collision of gas molecules produces a random fluctuating force with the spectral density given by[3]

$$S_F(\omega)=4mvPA_D=\frac{4M\omega_0 k_BT}{Q_{gas}}. \tag{3.12}$$

Similar to equation (3.5) and equation (3.6), the resulting formulas for the phase noise density and the Allan deviation are

$$S_\phi(\omega) = \frac{k_B T}{8\pi P_C {Q_{gas}}^2}\left(\frac{\omega_0}{\omega}\right)^2, \tag{3.13}$$

$$\sigma_A = \sqrt{\frac{k_B T}{P_C}\frac{1}{Q_{gas}^2 \tau_A}}\,.$$

(3.14)

After taking similar steps leading to equation (3.9), we obtain

$$\delta M \approx 2M_{eff}\left(\frac{E_{th}}{E_c}\right)^{1/2}\left(\frac{\Delta f}{Q_{gas}\omega_0}\right)^{1/2}. \tag{3.15}$$

3.4 Adsorption-Desorption Noise

Adsorption-desorption noise has been first discussed by Yong and Vig.[14] The resonator environment will always include a nonzero pressure of surface contaminated molecules. As the gas molecules adsorb and desorb on the resonator surface, they mass load the device randomly and cause the resonant frequency to fluctuate. Yong and Vig developed the model for noninteracting, completely localized monolayer adsorption, henceforth referred to as Yong and Vig's model. In addition to Yong and Vig's model, we present the ideal gas model for the case of noninteracting, completely delocalized adsorption. However, the extreme of completely localized or completely delocalized adsorption rarely occurs on real surfaces; the adsorption on real surfaces always lies between these two extremes.[15] Adsorbed gases molecules can interact with each other, resulting in phase transitions on the surface.[16] Instead of monolayer adsorption, multilayer

adsorption usually happens on real surfaces.[15] All these effects can further complicate the analysis of adsorption-desorption noise. The two models presented here, despite their simplicity, reveal valuable insight in the theoretical understanding of the adsorption-desorption noise.

In Yong and Vig's model, the assumption of localized adsorption means that the kinetic energy of the adsorbed molecule is much smaller than the depth of surface potential, and thus the adsorbed molecule is completely immobile in the later direction. Thus the concept of adsorption site on the surface is well defined. We further assume each site can accommodate only one molecule and consider the stochastic process of adsorption-desorption of each site. Consider a NEMS device surrounded by the gas with pressure, P, and temperature, T. From kinetic theory of gas, the adsorption rate of each site is given by the number of impinging atoms or molecules per unit time per unit area times the sticking coefficient, s, and the area per site A_{site}.

$$r_a = \frac{2}{5}\frac{P}{\sqrt{mkT}} sA_{site}, \tag{3.16}$$

where P and T are the pressure and temperature of gas, respectively. In general, the sticking coefficient depends on temperature and gaseous species.[17] Here we assume that the sticking coefficient is independent of the temperature.

Once bound to the surface, a molecule desorbs at a rate

$$r_d = \nu_d \exp(-\frac{E_b}{kT}), \tag{3.17}$$

ν_d is the desorption attempt frequency, typically of order 10^{13} Hz for a noble gas on a metallic surface, and E_b is the binding energy. For N molecules adsorbed on the surface, the total desorption rate for the whole device is Nr_d. Since each site can only

accommodate one molecule, the number of available sites for adsorption is N_a-N, so the total adsorption rate is $(N_a\text{-}N)r_a$. Equating these two rates, we obtain the number of adsorbed molecules

$$N = N_a \frac{r_a}{r_a + r_d}. \tag{3.18}$$

The average occupation probability f of a site is defined as the ratio of the adsorbed molecules to the total number of sites, N/N_a, and is given by $f = r_a/(r_a + r_d)$. Substitution of equation (3.16) and equation (3.17) into equation (3.18) yields the formula for the number of adsorbed molecules as a function of temperature, also known as the Langmuir adsorption isotherm.[16]

$$\frac{N}{N_a} = \frac{\frac{2}{5}\frac{p}{\sqrt{mkT}}\frac{s}{\nu_d}A_{site}\exp(\frac{E_b}{kT})}{\frac{2}{5}\frac{p}{\sqrt{mkT}}\frac{s}{\nu_d}A_{site}\exp(\frac{E_b}{kT})+1} = \frac{a(T)p}{1+a(T)p}, \tag{3.19}$$

$$a(T) = \frac{2}{5}\frac{P}{\sqrt{mkT}}\frac{s}{\nu_d}\exp(\frac{E_b}{kT}). \tag{3.20}$$

We can rewrite equation (3.16) in terms of the gaseous flux, Φ_{flux}, given by $\Phi_{flux} = (2/5)(P/\sqrt{mkT})$.

$$\frac{N}{N_a} = \frac{\Phi_{flux}\frac{s}{\nu_d}A_{site}\exp(\frac{E_b}{kT})}{\Phi_{flux}\frac{s}{\nu_d}A_{site}\exp(\frac{E_b}{kT})+1}. \tag{3.21}$$

We derive the spectral density of the frequency noise by considering the stochastic process of the adsorption-desorption of each site, which can be described by a continuous time two state Markov chain.[14] Here we briefly sketch the derivation for a two state Markov chain.[18] Since each site can be occupied or unoccupied, we consider a

continuous time stochastic process $\{\zeta(t), t>0\}$, where the random variable $\zeta(t)$ can take either 0 (unoccupied) or 1 (occupied). The two rate constants of such a Markov chain are r_d, the rate from state 1 (occupied state) to state 0 (unoccupied), and r_a, the rate from state 0 (unoccupied state) to state 1 (occupied state).We define $P_{ij}(t)$ as the conditional probability that a Markov chain, presently in state *i*, will be in the state *j* after additional time *t*. Assuming that the site is initially occupied, we have initial condition, $P_{11}(0)=1$, and for a two state system, $P_{10}(t)=1-P_{11}(t)$. The corresponding Kolmogorov's forward equation and its solution are given by[10]

$$\frac{dP_{11}}{dt} = r_d P_{10}(t) - r_a P_{11}(t), \tag{3.22}$$

$$P_{11}(t) = \frac{r_a}{r_a + r_d} + \frac{r_d}{r_a + r_d} e^{-(r_a + r_d)t} = f + (1-f)e^{-t/\tau_r}. \tag{3.23}$$

The correlation time τ_r is defined as $1/(r_a + r_d)$. The autocorrelation function can be found by calculating the expectation value of $\zeta(t+\tau)\zeta(t)$ from the conditional probability function. By definition, the autocorrelation function of $\zeta(t)$ is given by

$$R_{site}(\tau) = E[\zeta(t+\tau)\zeta(t)] = \sigma_{OCC}^2 e^{-|\tau|/\tau_r} + f. \tag{3.24}$$

E[] denotes the expectation value of the random variable. Here for our purpose, we neglect the constant term *f* since this corresponds to the D.C. part of the spectra. σ_{OCC}^2 is the variance of occupational probability *f*, given by $\sigma_{OCC}^2 = f(1-f) = r_a r_d /(r_a + r_d)^2$. Note that σ_{OCC}^2 reaches a maximum for *f*=0.5 when the adsorption and desorption rates of the site are equal.

We apply the Wiener-Khintchine theorem to obtain the corresponding spectral density of $\zeta(t)$ for each site by performing the Fourier transform of equation (3.24).

$$S_{\zeta}(\omega) = \frac{2\sigma_{OCC}^2 \tau_r / \pi}{1 + (\omega\tau_r)^2}. \tag{3.25}$$

Each adsorbed molecule of mass m will contribute to fractional frequency change $m/2M_{eff}$. We obtain the spectral density of fractional frequency noise by simply summing the contribution from each individual site.

$$S_y(\omega) = \frac{2\sigma_{OCC}^2 N_a / \pi}{1 + (\omega\tau_r)^2}\left(\frac{m}{2M_{eff}}\right)^2. \tag{3.26}$$

Since the spectral density exhibits Lorentizian function form, we use equation (2.16) to obtain

$$\sigma_A(\tau_A) = \sqrt{N_a}\,\sigma_{OCC}\,\frac{m}{M_{eff}}\sqrt{F(\frac{\tau_r}{\tau_A})}. \tag{3.27}$$

$F(x)$ is the analytic function defined in equation (2.17). In the limit, $\tau_r << \tau_A$, equation (3.27) becomes

$$\sigma_A(\tau_A) = \sqrt{N_a}\,\sigma_{OCC}\,\frac{m}{M_{eff}}\sqrt{\frac{\tau_r}{2\tau_A}}. \tag{3.28}$$

In the other limit, $\tau_A << \tau_r$, equation (3.27) becomes

$$\sigma_A(\tau_A) = \sqrt{N_a}\,\sigma_{OCC}\,\frac{m}{M_{eff}}\sqrt{\frac{\tau_A}{6\tau_r}}. \tag{3.29}$$

In the ideal gas model, the assumption of delocalized adsorption means that the kinetic energy of the adsorbed molecule is much higher than the depth of the surface potential, and thus the adsorbed molecule is mobile in the lateral direction. The notion of adsorption site in Yong and Vig's model is not well defined.[14] We thus analyze the

kinetics of adsorption-desorption using the total adsorption and desorption rates of the adsorbed atoms on the device. The total adsorption rate of the device is given by the flux of molecules multiplied by the sticking coefficient *s* and the device area A_D,

$$R_a = \frac{2}{5}\frac{P}{\sqrt{mk_BT}}sA_D. \tag{3.30}$$

Once bound to the surface, the molecule desorbs at a rate given by $r_d = \nu_d \exp(-E_b / kT)$. The total desorption rate of all the adsorbed molecules on the device is simply

$$R_d = \nu_d \exp(-\frac{E_b}{kT})N. \tag{3.31}$$

At equilibrium, the total adsorption rate equals the total desorption rate, and the number of adsorbed molecules is given by

$$\frac{N}{A_D} = \frac{2}{5}\frac{s}{\nu_d}\frac{P}{\sqrt{mkT}}\exp(\frac{E_b}{kT}) = b(T)P, \tag{3.32}$$

$$b(T) = \frac{2}{5}\frac{s}{\nu_d}\frac{1}{\sqrt{mkT}}\exp(\frac{E_b}{kT}). \tag{3.33}$$

We also rewrite the expression in terms of the impinging gaseous flux Φ_{flux},

$$\frac{N}{A_D} = \frac{s}{\nu_d}\Phi_{flux}\exp(\frac{E_b}{kT}). \tag{3.34}$$

We derive the spectral density of the fractional frequency noise by considering the dilute gas limit of Yong and Vig's model. This is done by keeping the number of adsorbed molecules, $N = fN_a$, constant, and letting the occupational probability go to zero, and N_a go to infinity. Hence, $\sigma_{OCC}^2 N_a = f(1-f)N_a \to N$. The spectral density of fractional frequency noise becomes

$$S_y(\omega) = \frac{2N/\pi}{1+(\omega\tau_r)^2}\left(\frac{m}{2M_{eff}}\right)^2 . \tag{3.35}$$

The correlation time due to adsorption-desorption cycle is given by the time constant of the rate equation

$$\frac{dN}{dt} = R_a - R_d = R_a - \nu_d \exp(-\frac{E_b}{kT})N . \tag{3.36}$$

We find that

$$\tau_r = \nu_d \exp(\frac{E_b}{kT}) . \tag{3.37}$$

Since the spectral density of fractional frequency in equation (3.35) exhibits Lorentizian function form, we use equation (2.16) to obtain

$$\sigma_A(\tau_A) = \sqrt{N}\frac{m}{M_{eff}}\sqrt{F(\frac{\tau_r}{\tau_A})} . \tag{3.38}$$

In the limit, $\tau_r << \tau_A$, this expression becomes

$$\sigma_A(\tau_A) = \sqrt{N}\frac{m}{M_{eff}}\sqrt{\frac{\tau_r}{2\tau_A}} . \tag{3.39}$$

In the other limit, $\tau_A << \tau_r$, this expression becomes

$$\sigma_A(\tau_A) = \sqrt{N}\frac{m}{M_{eff}}\sqrt{\frac{\tau_A}{6\tau_r}} . \tag{3.40}$$

Table 3.3 tabulates the expressions for the two models presented here. Note that equation (3.27) differs from equation (3.38) in the statistics. The occupational variance σ_{OCC}^2 in equation (3.27) and thus adsorption-desorption noise in Yong and Vig's model vanishes upon completion of one monolayer due to the assumption that each site accommodates

only one molecule. In contrast, equation (3.38) exhibits idea gas statistics, manifested in the square root dependence of the number of adsorbed molecules.

Now we discuss the effect of the correlation time on Allan deviation. Because the spectral density of fractional frequency for these two models exhibits Lorentizian functional form, both equation (3.27) and equation (3.38) have the same dependence on the ratio of the correlation time, τ_r, to the averaging time, τ_A, through the analytic function, $F(x)$, defined in equation (2.17). Mathematically, $F(x)$ reaches a maximum at 0.095 for x=1.85 and vanishes when x equals to zero or infinity, and. In other words, the adsorption-desorption noise in both models maximizes when $\tau_r = 0.095\tau_A$ and diminishes for $\tau_r >> \tau_A$ or $\tau_r << \tau_A$ with the asymptotic behaviors dictated by equation (3.25), equation (3.26), equation (3.37), and equation (3.38).

To explicitly illustrate the surface effect of adsorption-desorption noise, we give the expression for the maximum Allan deviation $\sigma_{A\max}$ in Yong and Vig's model by simultaneously maximizing σ_{OCC} and $F(\tau_r / \tau_A)$ in equation (3.27). We find that

$$\sigma_{A\max} = 0.3\frac{\sqrt{N_a}m}{N_a m_D} = 0.3\left(\frac{m}{m_D}\right)\frac{\sqrt{N_a}}{N_V} = 0.3\left(\frac{m}{m_D}\right)\frac{1}{\sqrt{N_V}}\frac{N_a}{N_V}. \tag{3.41}$$

Here m_D is the mass of a single atom adsorbed the device. N_V is the total number of atoms of the device. N_a / N_V is the surface-to-volume ratio.

Finally, we give the expressions for minimum measurable frequency shift and mass sensitivity. For Yong and Vig's model, the integration of the spectra density yields

$$\delta\omega_0 = \frac{1}{2\pi}\frac{m\omega_0\sigma_{occ}}{M_{eff}}\left[N_a \arctan(2\pi\Delta f\tau_r)\right]^{1/2}, \tag{3.42}$$

$$\delta M \approx \frac{1}{2\pi} m\sigma_{occ}\left[N_a \arctan(2\pi\Delta f\tau_r)\right]^{1/2}. \tag{3.43}$$

Similar to equation (3.41), we give the expression for the maximum mass fluctuation $\delta M_{\max}$ by the maximized σ_{OCC} and $\arctan(2\pi\Delta f\tau_r)$ in equation (3.43) from Yong and Vig's model. We find that $\delta M_{\max} \approx 1/\sqrt{32\pi}\sqrt{N_a}m$ when $2\pi\Delta f\tau_r \to \infty$ and f=0.5.

Similarly, for ideal gas model, we obtain

$$\delta\omega_0 = \frac{1}{2\pi}\frac{m\omega_0}{M_{eff}}\left[N \arctan(2\pi\Delta f\tau_r)\right]^{1/2}, \tag{3.45}$$

$$\delta M \approx \frac{1}{2\pi} m\left[N \arctan(2\pi\Delta f\tau_r)\right]^{1/2}. \tag{3.46}$$

Table 3.2 summarizes the expressions from Yong and Vig's and ideal gas models. Table 3.3 shows the numerical estimates of $\sigma_{A\max}$ and $\delta M_{\max}$ arising from nitrogen for the same representative NEMS devices used in table 3.1. (The number of sites, N_a, is calculated assuming each atom on the device surface serves as one adsorption site. For silicon beam and nanowire, we assume that the device surface is terminated Si(100) with lattice constant=5.43 Å. For a single-walled nanotube (SWNT), we assume that the carbon bond length is 1.4 Å.) First, the magnitude of $\delta M_{\max}$ indicates that the mass fluctuation associate with adsorption-desorption noise of NEMS is at zeptogram level. Second, table 3.4 shows the increase of Allan deviation as a result of increasing the surface-to-volume ratio as the device dimensions are progressively scaled down. In particular, for the 10 GHz single-walled nanotube (SWNT), representing the extreme case that all the atoms are on the surface, the corresponding Allan deviation is almost five orders of magnitude higher than that due to thermomechanical noise (see table 3.1). In other words, the adsorption-desorption noise can severely degrade the noise performance

of the device. This, however, can be circumvented by packaging the device at low pressure or passivating the device surface.

Table 3.2. Summary of Yong and Vig's and ideal gas models

	Yong and Vig	Ideal Gas
Adsorption	Localized	Delocalized
Rates	$r_a = \frac{2}{5}\frac{p}{\sqrt{mkT}} sA_{Site}$ $r_d = \nu_d \exp(E_b / k_B T)$	$R_a = \frac{2}{5}\frac{p}{\sqrt{mk_B T}} sA_D$ $R_d = \nu_d \exp(E_b / k_B T) N$
Isotherm	$\frac{N}{N_a} = \frac{a(T)p}{1+a(T)p}$ $a(T) = \frac{2}{5}\frac{s}{\sqrt{mkT}\nu_d} \exp(\frac{E_b}{kT}) A_{site}$	$\frac{N}{A_D} = b(T)p$ $b(T) = \frac{2}{5}\frac{s}{\sqrt{mkT}\nu_d} \exp(\frac{E_b}{kT})$
Correlation Time	$\tau_r = 1/(r_a + r_d)$	$\tau_r = 1/\nu_d \exp(E_b / kT)$
Spectral Density	$S_y(\omega) = \frac{2N_a \sigma_{OCC}^2 \tau_r / \pi}{1+\omega^2 \tau_r^2} \left(\frac{m}{M_{eff}}\right)^2$	$S_y(\omega) = \frac{2N\tau_r / \pi}{1+\omega^2 \tau_r^2} \left(\frac{m}{M_{eff}}\right)^2$
Allan deviation	$\sigma_A = \sigma_{OCC}\sqrt{N_a}\frac{m}{M_{eff}}\sqrt{\frac{\tau_r}{2\tau_A}}$ $\sigma_{OCC}^2 = r_a r_d / (r_a + r_d)^2$	$\sigma_A = \sqrt{N}\frac{m}{M_{eff}}\sqrt{\frac{\tau_r}{2\tau_A}}$

Device	Frequency	N_a/N_V	Na	σ_{Amax}(gas)	δM_{max}
Si beam	1 GHz	1.1×10^{-2}	8.9×10^{5}	1.7×10^{-6}	1.6 zg
Si nanowire	7.7 GHz	5.5×10^{-2}	2.7×10^{4}	4.9×10^{-5}	0.28 zg
SWNT	10 GHz	1	5.0×10^{3}	4.9×10^{-3}	0.27 zg

Table 3.3. Maximum Allan deviation and mass fluctuation of representative NEMS devices

3.5 Diffusion Noise

So far we have analyzed the adsorption-desorption noise from adsorbed gasous species on the NEMS device. The surface diffusion provides another channel for exchange of adsorbed species between the device and the surroundings to generate noise. We start the analysis of diffusion noise from calculating the autocorrelation function of fractional frequency fluctuation. Mathematically, the autocorrelation function $G(\tau)$ is calculated as the time average ($<>$) of the product of the frequency fluctuations of the NEMS.

$$G(\tau) = <\delta f(t)\delta f(t+\tau)> / <f(t)>^2 = <\int \delta f(x,t)dx \int \delta f(x',t+\tau)dx'> / <f(t)>^2 . \quad (3.47)$$

Here $f(t)$ is the instantaneous resonant frequency of the device and we define the averaged resonant frequency by $<f(t)> \equiv f_0$. In the actual experiments, $\delta f(x,t)$ remains proportional to local concentration fluctuation $\delta C(x,t)dx$ and is given by

$$\frac{\delta f(x,t)}{f_0} = -\frac{m}{2M_{eff}} \frac{u(x)^2 \delta C(x,t)dx}{\frac{1}{L}\int u(x)^2 dx}, \quad (3.48)$$

where m is the mass of the adsorbed atoms or molecules, M_{eff} is the effective vibratory mass of the device,[3] L is the length of the device, and $u(x)$ is the eigenfunction describing flexural displacement of the beam. Here we only consider the fundamental mode $u(x) = 0.883\cos kx + 0.117\cosh kx$ for a beam extending from $-L/2$ to $L/2$, with $kL = 4.730$ with doubly clamped boundary condition imposed. Note that the end of the beam is never perfectly clamped so doubly clamped boundary condition is only an approximation. The normalization of $u(x)$ factors out in equation (3.48); therefore we are

free to choose $u(0)=1$. We define Green function for diffusion as $\phi(x,x',\tau) =< \delta C(x,t+\tau)\delta C(x',t) >$. As a result, equation (3.48) becomes

$$G(\tau) = L^2(\frac{m}{2M_{eff}})^2 = L^2(\frac{m}{2M_{eff}})^2 \frac{\int_{-L/2}^{L/2} dx \int_{-L/2}^{L/2} dx' u(x)^2 u(x')^2 \phi(x,x',t) >}{\left[\int_{-L/2}^{L/2} u(x)^2 dx\right]^2}. \quad (3.49)$$

In case of pure diffusion of one species in one dimension, the concentration $\delta C(x,\tau)$ obeys the diffusion equation

$$\frac{\partial \delta C(x,\tau)}{\partial \tau} = D\frac{\partial^2 \delta C(x,\tau)}{\partial^2 x}. \quad (3.50)$$

Following Elson and Magde,[19,20] we find that

$$\phi(x,x',\tau) = \frac{N}{L}\frac{1}{\sqrt{4\pi D\tau}}\exp[-\frac{(x-x')^2}{4D\tau}], \quad (3.51)$$

where N is the average total number of the adsorbed atoms inside the device. To calculate the autocorrelation function, we can approximate the vibrational mode shape $u(x)$ by a Gaussian mode shape $\exp[-\frac{1}{2}(\frac{ax}{L})^2]$ with a numerical factor a=4.43, extending from -∞ to ∞. Figure 3.1 shows the true vibration mode shape of the beam with its Gaussian approximation. Using Gausssian approximation, we can perform the integral analytically and obtain the autocorrelation function of the fractional frequency noise

$$\begin{aligned} G(\tau) &= L^2(\frac{m}{2M_{eff}})^2 \int_{-L/2}^{L/2} dx' \int_{-L/2}^{L/2} dx[u(x)^2 u(x')^2 \phi(x,x',\tau) / \left[\int_{-L/2}^{L/2} u(x'')^2 dx''\right]^2 \\ &\approx L^2(\frac{m}{2M_{eff}})^2 \int_{-\infty}^{\infty} dx \int_{-\infty}^{\infty} dx'[u(x)^2 u(x')^2 \phi(x,x',\tau) / \left[\int_{-\infty}^{\infty} u(x'')^2 dx''\right]^2 \quad (3.52) \\ &= \frac{aN}{\sqrt{2\pi}}(\frac{m}{2M_{eff}})^2 \frac{1}{(1+\tau/\tau_D)^{1/2}}. \end{aligned}$$

Here the diffusion time is defined by $\tau_D = L^2/(2a^2 D)$. Note that the time course of $G(\tau)$ is determined by the factor $(1+\tau/\tau_D)^{-1/2}$ even if the concentration correlation function has a typical exponential time dependence. This results from the convolution of the exponential Fourier components of diffusion with the Gaussian profile of the mode shape.[20] Also note that $G(\tau)$ is of the form $(1+\tau/\tau_D)^{-1/2d}$ with $d=1$, the dimensionality of the problem. This is consistent with the factor $(1+\tau/\tau_D)^{-1/2d}$, obtained by Elson and Magde with $d=2$.

We then apply the Wiener-Khintchine theorem to obtain the corresponding spectral density by

$$S_y(\omega) = \frac{1}{\pi}\int_{-\infty}^{\infty} G(\tau)e^{i\omega\tau} = \frac{\sqrt{2}aN}{\pi^{3/2}}\left(\frac{m}{2M_{eff}}\right)^2 \int_0^{\infty} \frac{\cos\omega\tau}{(1+\tau/\tau_D)^{1/2}}\,d\tau$$
$$= \frac{aN}{4\pi}\left(\frac{m}{M_{eff}}\right)^2 \tau_D \xi(\omega\tau_D). \tag{3.53}$$

Here $\xi(x) \equiv (\cos(x)+\sin(x) - 2C(\sqrt{x})\cos(x) - 2S(\sqrt{x})\sin(x))/\sqrt{x}$ and $C(x)$ and $S(x)$ are Fresnel integrals defined by[21]

$$C(x) = \sqrt{\frac{2}{\pi}}\int_0^x \cos u^2\,du, \tag{3.54}$$

$$S(x) = \sqrt{\frac{2}{\pi}}\int_0^x \sin u^2\,du. \tag{3.55}$$

In figure 3.2, we plot the function $\xi(x)$ with its asymptotic forms: $\xi(x) = 1/\sqrt{x}$ as $x \to 0$ and $\xi(x) = 1/x^2\sqrt{2\pi}$ as $x \to \infty$. For $\omega << 1/\tau_D$, the spectral density of fractional frequency noise is given by

$$S_y(\omega) = \frac{aN}{4\pi}\left(\frac{m}{M_{eff}}\right)^2 \tau_D \frac{1}{\sqrt{\omega\tau_D}}. \tag{3.56}$$

For $\omega >> 1/\tau_D$, the spectral density of fractional frequency noise is given by

$$S_y(\omega) = \frac{a}{4\sqrt{2}\pi^{3/2}} N(\frac{m}{M_{eff}})^2 \frac{1}{\omega^2 \tau_D}. \tag{3.57}$$

We now obtain the expression for Allan deviation using equation (3.53) by the performing the following integration,

$$\sigma_A^2(\tau_A) = \int_0^\infty \frac{8}{(\omega\tau_A)^2} S_y(\omega) \sin^4(\omega\tau_A/2) d\omega = \frac{2aN}{\pi} \left(\frac{m}{M_{eff}}\right)^2 X(\frac{\tau_D}{\tau_A}). \tag{3.58}$$

Here $X(x)$ is defined as

$$X(x) = x\int_0^\infty \xi(\eta x) \frac{\sin^4(\eta/2)}{\eta^2} d\eta. \tag{3.59}$$

For $x \to \infty$, the asymptotic form of $X(x)$ is given by

$$X(x) = \frac{\pi^{1/2}}{24\sqrt{2}} \frac{1}{x}. \tag{3.60}$$

In figure 3.3, we plot the function $X(x)$ in equation (3.60) together with its asymptotic form. For the limit, $\tau_D >> \tau_A$, we give the expression for Allan deviation as[1]

$$\sigma_A^2(\tau_A) = \int_0^\infty \frac{8}{(\omega\tau_A)^2} S_y(\omega) \sin^4(\omega\tau_A/2) d\omega = \frac{aN}{12\pi} \left(\frac{m}{M_{eff}}\right)^2 \frac{\tau_A}{\tau_D}. \tag{3.61}$$

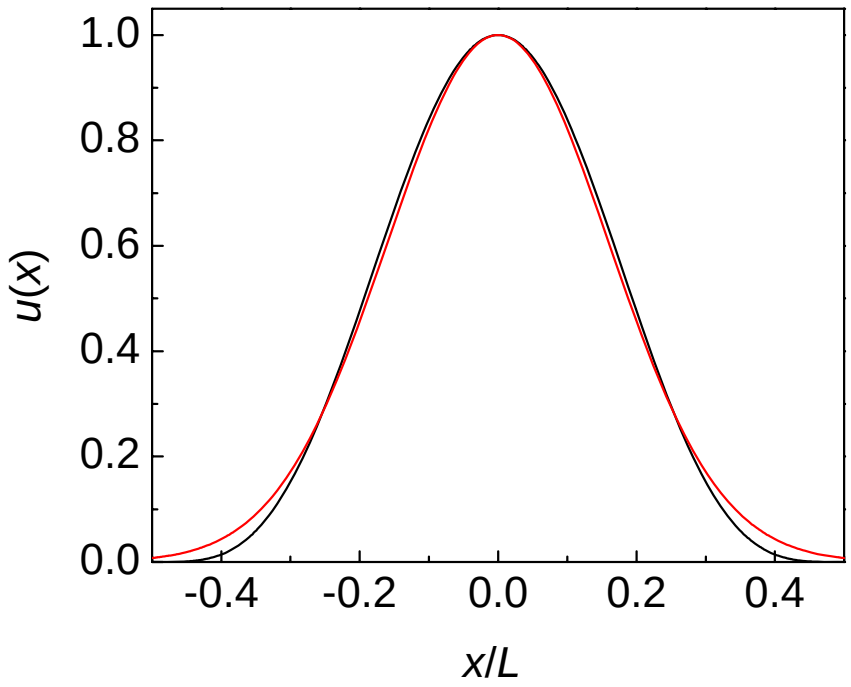

Figure 3.1. Vibrational mode shape of the beam with doubly clamped boundary condition imposed and its Gaussian approximation. The vibrational beam mode shape (black) with doubly clamped boundary condition imposed is displayed with its Gaussian approximation (red).

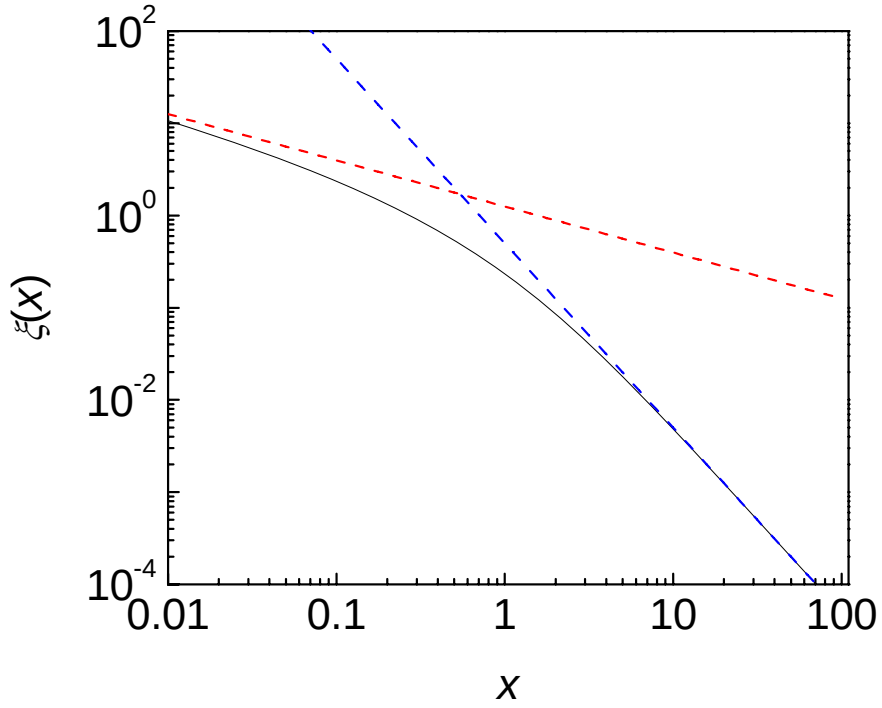

Figure 3.2. Plot of the function $\xi(x)$. The function $\xi(x)$ (black solid) is plotted together with it asymptotic approximations $1/\sqrt{x}$ (red dash) as $x \to 0$ and $1/x^2\sqrt{2\pi}$ (blue dash) as $x \to \infty$.

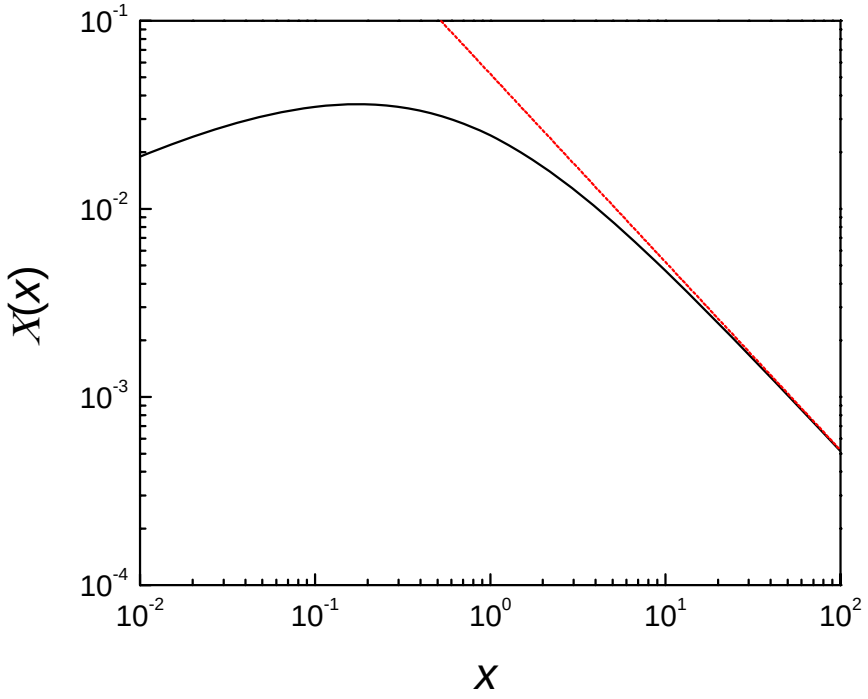

Figure 3.3. Plot of $X(x)$ and its asymptotic form. The function $X(x)$ (black solid) is plotted together with its asymptotic form (red dash) $X(x) = \frac{\pi^{1/2}}{24\sqrt{2}} \frac{1}{x}$ as $x \to \infty$.

3.6 Temperature Fluctuation Noise

The small dimensions of NEMS resonators in general imply that the heat capacity is very small and therefore the corresponding temperature fluctuations can be rather large. The effect of such fluctuations depends on upon the thermal contact of the NEMS to their environment. Because the resonant frequency depends on the temperature through the resonator material parameters and geometric dimensions, the temperature fluctuations produce frequency fluctuations. Here we present a simple model using the thermal circuit consisting of a heat capacitance, c, connected by a thermal conductance, g, to an infinite thermal reservoir at temperature, T. In the absence of any power load, the heat capacitance, c, will have an average thermal energy, $\langle E_C \rangle = cT$. Changes in temperature relax with thermal time constant, $\tau_T = c/g$. Applying the fluctuation-dissipation theorem to such a circuit, we expect a power noise source, p, connected to the thermal conductance, g, with the spectral density, $S_p(\omega) = 2k_B T^2 g/\pi$, and cause the instantaneous energy, $E_C(t) = \langle E_C \rangle + \delta E(t)$, to fluctuate.[4] The spectral density of the energy fluctuations $\delta E(t)$ can be derived as

$$S_E(\omega) = \frac{2}{\pi} \frac{k_B T^2 c^2 / g}{1 + \omega^2 \tau_T^2}. \tag{3.62}$$

We can interpret the energy fluctuations as temperature fluctuations $\delta T_C(t)$, if we define the temperature as $T_C = E_C / c$. The corresponding spectral density of the temperature fluctuations is given by

$$S_T(\omega) = \frac{2}{\pi} \frac{k_B T^2 / g}{1 + \omega^2 \tau_T^2}. \tag{3.63}$$

Equation (3.63) applies to any system that can be modeled as a heat capacitance with a thermal conductance. For a doubly clamped beam, however, there is no clear separation of the structure into a distinct heat capacitance and a thermal conductance. Cleland and Roukes have developed a distributed model of thermal transport along a doubly clamped beam of constant cross section, and derived the spectral density of frequency fluctuations arising from temperature fluctuations of a NEMS resonator.[1] Their analysis leads to

$$S_T(\omega) = \frac{4}{\pi}\frac{k_B T^2 / g}{1+\omega^2\tau_T^2}, \tag{3.64}$$

$$S_y(\omega) = \left(-\frac{22.4}{\omega_0^2 L^2}\alpha_T + \frac{2}{c_s}\frac{\partial c_s}{\partial T}\right)^2 \frac{1}{\pi}\frac{k_B T^2 / g}{1+\omega^2\tau_T^2}. \tag{3.65}$$

Here $c_s = \sqrt{E/\rho}$ is the temperature dependent speed of sound, $\alpha_T = (1/L)\partial L/\partial T$ is the linear thermal expansion coefficient, and g and τ_T are the thermal conductance and thermal time constant for the slice, respectively. In the limits $\tau_A >> \tau_T$, the Allan deviation is given by

$$\sigma_A(\tau_A) = \sqrt{\frac{2k_B T^2}{g\tau_A}}\frac{1}{\tau_T}\left(-\frac{22.4}{\omega_0^2 L^2}\alpha_T + \frac{2}{c_s}\frac{\partial c_s}{\partial T}\right)^2. \tag{3.66}$$

To give the expression for $\delta\omega_0$ and δM, we integrate equation (3.65) over the measurement bandwidth and obtain

$$\delta\omega_0 = \left[\frac{1}{2\pi^2}\left(-\frac{22.4 {c_s}^2}{{\omega_0}^2 l^2}\alpha_T + \frac{2}{c_s}\frac{\partial c_s}{\partial T}\right)^2 \frac{{\omega_0}^2 k_B T^2}{g}\frac{\arctan(2\pi\Delta f\tau_T)}{\tau_T}\right]^{1/2}, \tag{3.67}$$

$$\delta M = \frac{2}{\pi^{1/2}} 2M_{eff} \left(-\frac{22.4 {c_s}^2}{{\omega_0}^2 l^2} \alpha_T + \frac{2}{c_s} \frac{\partial c_s}{\partial T} \right) \left[\frac{k_B T^2 \arctan(2\pi \Delta f \tau_T)}{g \tau_T} \right]^{1/2}. \quad (3.68)$$

The values of the material dependent constants for silicon have been calculated as[1]

$$\left(-\frac{22.4}{\omega_0^2 L^2} \alpha_T + \frac{2}{c_s} \frac{\partial c_s}{\partial T} \right)^2 = 1.26 \times 10^{-4}\ 1/\text{K}. \quad (3.69)$$

$g = 7.4 \times 10^{-6}$ W/K and $\tau_T = 30$ ps. Using these values, a numerical estimate of equation (3.66) for 1 GHz silicon beam in table 3.1 is given by $\sigma_A(\tau_A) = 9.3\text{x}10^{-11}/\sqrt{\tau_A}$.[1] For $\tau_A = 1$ sec, the Allan deviation is $9.3\text{x}10^{-11}$, of the same order of magnitude as that due to the thermomechanical noise at room temperature listed in table 3.1. Similarly, for the same device at room temperature with measurement bandwidth Δf = 1 Hz, we obtain δM = 0.245 Da. Despite of the role of thermal fluctuations in generating phase noise that limits the mass sensitivity, single Dalton sensing is readily achievable. The effect can be even more significant as we further scale down the dimensions or increase the device temperature. This can be circumvented by lowering the temperature or optimizing the thermal contact of the NEMS to its environment.

3.7 Nonfundamental Noise

We develop a simple formalism to consider nonfundamental noise process from transducer amplifier implementations of NEMS.[5] First, the spectral density of the frequency noise $S_\omega(\omega)$ is transformed into the voltage domain by the displacement

transducer, the total effective voltage noise spectral density at the transducer's output predominantly originates from the transducer and readout amplifier.[5] It is the total voltage noise referred back to the frequency domain that determines the effective frequency fluctuation spectral density for the system $S_\omega(\omega) = S_V/(\partial V/\partial\omega)^2$. V is the transducer output voltage. If we define the transducer responsivity by the derivative of transducer output voltage with respect to displacement, i.e., $R_T = (\partial V/\partial x)$, a simple estimate is given by $(\partial V/\partial\omega) \approx QR_T|x_C|/\omega_0$. Assuming the voltage fluctuation S_V results from Nyquist-Johnson noise from the transducer amplifier and thus has a white spectrum, using equation (2.15) we obtain the expression for the Allan deviation

$$\sigma_A(\tau_A) = \frac{1}{Q}\frac{(\pi S_V/\tau_A)^{1/2}}{R_T|x_C|}. \tag{3.70}$$

We can rewrite this equation in a simple form in terms of the dynamic range, $DR = 20\log[R_T^2|x_C|^2/(\pi S_V/\tau_A)^{1/2}]$, or equivalently the signal-to-noise ratio (SNR) referred to transducer output of the NEMS.

$$\sigma_A(\tau_A) = \frac{1}{Q}10^{-DR/20}. \tag{3.71}$$

Finally, we give the expression for the minimum detectable frequency shift $\delta\omega$ and mass sensitivity δM. Upon the integration of spectral density using equation (2.21), the minimum detectable frequency shift for the measurement bandwidth Δf, is simply

$$\delta\omega = \frac{\omega_0}{Q}\frac{(S_V\Delta f)^{1/2}}{R_T|x_C|} = \frac{\omega_0}{Q}10^{-DR/20}. \tag{3.72}$$

The mass sensitivity follows as

$$\delta M \sim 2(M_{eff}/Q)10^{-DR/20}. \tag{3.73}$$

Equation (3.73) indicates the essential considerations for optimizing NEMS based mass sensors limited by the Nyquist-Johnson noise. First, this emphasizes the importance of devices possessing low mass, i.e., small volume, while keeping high *Q*. Second, the dynamic range for the measurement should be maximized. This latter consideration certainly involves careful engineering to minimize the noise from transducer amplifier implementations and controlling the nonlinearlity of the resonator through the mechanical design.

3.8 Conclusion

We present the theory of phase noise mechanisms affecting NEMS. We examine both *fundamental* and *nonfundamental* noises and their imposed limits on device performance. Table 3.4 tabulates the expressions for fundamental noise processes considered in this work. We find that the anticipated noise is predominantly from thermomechanical noise, temperature fluctuation noise, adsorption-desorption noise, and diffusion noise. First, a large dynamic range is always desirable for obtaining frequency stability in the case of thermomechanical noise. Clearly, as the device sizes are scaled downward while maintaining high resonance frequencies, M_{eff} and κ_{eff} must shrink in direct proportion. Devices with small stiffness (high compliance) are more susceptible to thermal fluctuations and consequently, the dynamic range becomes reduced. Second, next generation NEMS appear to be more susceptible to temperature fluctuations—more intensively at elevated temperatures. This fact can be circumvented by lowering the device temperatures and by designing NEMS with better thermalization properties. Third, for adsorption-desorption noise, both Yong and Vig's and ideal gas model suggest that

this noise becomes significant when appreciable molecules adsorb on the NEMS surface and the correlation time of adsorption-desorption cycle roughly matches the averaging time. One could easily prevent this, for instance, by reducing the packaging pressure or passivating the device to change the binding energy between the molecule and the surface.

To evaluate the impact of each noise process on the mass sensing application, we give expressions for the minimum measurable frequency shift and mass sensitivity. Our analysis culminates in the expression equation (3.10), i.e.,

$$\delta M \approx \frac{1}{\Re}\left(\Delta f \frac{\omega_0}{Q}\right)^{1/2} 10^{(-DR/20)}. \tag{3.74}$$

Equation (3.74) distills and makes transparent the essential considerations for optimizing inertial mass sensors at any size scale. There are three principal considerations. First, the mass responsivity, $\Re$, should be maximized. As seen from equation (3.3), this emphasizes the importance of devices possessing low mass, i.e., small volume, which operate with high resonance frequencies. Second, the measurement bandwidth should employ the full range that is available. Third, the dynamic range for the measurement should be maximized. At the outset, this latter consideration certainly involves careful engineering to minimize nonfundamental noise processes from the transducer amplifier implementation, as expressed in equation (3.72) and equation (3.73). But this is ultimately feasible only when fundamental limits are reached. In such a regime it is the fundamental noise processes that become predominant.

In table 3.1, we have translated the analytical results from equation (3.10) into concrete numerical estimates for representative and realizable device configurations. The values of δM span only the regime from a few tenths to a few tens of Daltons. This is the

mass range for a small *individual* molecule; hence it is clear that nanomechanical mass sensors offer unprecedented sensitivity to *weigh* individual neutral molecules routinely—blurring the distinction between conventional inertial mass sensing and mass spectrometry.[11]

Table 3.4 Summary of expressions for spectral density and Allan deviation for fundamental noise processes considered in this work

Noise	Correlation Time	Expression
Thermomechanical	None	$S_\phi(\omega) = \frac{k_B T}{8\pi P_c Q^2}\left(\frac{\omega_0}{\omega}\right)^2$ $\sigma_A(\tau_A) = \sqrt{\frac{k_B T}{8 P_C Q^2 \tau_A}}$
Momentum Exchange	None	$S_\phi(\omega) = \frac{k_B T}{8\pi P_c Q_{gas}^{\ 2}}\left(\frac{\omega_0}{\omega}\right)^2$ $\sigma_A(\tau_A) = \sqrt{\frac{k_B T}{8 P_C Q_{gas}^2 \tau_A}}$
Adsorption-Desorption Yong and Vig's Model	$\tau_r = 1/(r_a + r_d)$	$S_y(\omega) = \frac{2\sigma_{OCC}^2 N_a \tau_r / \pi}{1+\omega^2\tau_r}(\frac{m}{2M_{eff}})^2$ $\sigma_A(\tau_A) = \sqrt{N_a}\,\frac{\sigma_{OCC} m}{M_{eff}}\sqrt{F(\frac{\tau_r}{\tau_A})}$
Ideal Gas Model	$\tau_r = 1/\nu_d \exp(E_b/k_B T)$	$S_y(\omega) = \frac{2N\tau_r/\pi}{1+\omega^2\tau_r}\left(\frac{m}{2M_{eff}}\right)^2$ $\sigma_A(\tau_A) = \sqrt{N}\,\frac{m}{M_{eff}}\sqrt{F(\frac{\tau_r}{\tau_A})}$
Diffusion	$\tau_D = L^2/2a^2 D$	$\sigma_A(\tau_A) = \frac{2aN}{\pi}\left(\frac{m}{M_{eff}}\right)^2 X(\frac{\tau_D}{\tau_A})$
Temperature Fluctuation	$\tau_T = c/g$	$S_y(\omega) = \left[\frac{1}{\omega_0}(\frac{\partial\omega_0}{\partial T})\right]_T^2 \frac{4}{\pi}\frac{k_B T/g}{1+\omega^2\tau_T^2}$ $\sigma_A(\tau_A) = \sqrt{\frac{4k_B T}{g\tau_A}}\,\frac{1}{\tau_T}\,\frac{1}{\omega_0}\left(\frac{\partial\omega_0}{\partial T}\right)$

References

1. A. N. Cleland and M. L. Roukes Noise processes in nanomechanical resonators. *J. Appl. Phys.* **92**, 2758 (2002).

2. J. Vig and Y. Kim Noise in MEMS resonators. *IEEE Trans. on Ultrasonics Ferroelectics and Frequency Control.* **46**, 1558 (1999).

3. K. L. Ekinci, Y. T. Yang, M. L. Roukes Ultimate limits to inertial mass sensing based upon nanoelectromechanical systems. *J. Appl. Phys.* **95**, 2682 (2004).

4. L. D. Landau and E. M. Lifshitz *Statistical Physics* (England, Oxford, 1980).

5. K. L. Ekinci, X. M. H. Huang, and M. L. Roukes Ultrasensitive nanoelectromechanical mass detection. *Appl. Phys. Lett.* **84**, 4469 (2004).

6. For the fundamental mode response of a doubly clamped beam with rectangular cross section, the effective mass, dynamic stiffness are given as $M_{eff} = 0.735ltw\rho$, $\kappa_{eff} = 32Et^3w/L^3$. Here, *L*, *w*, and *t* are the length, width and thickness of the beam. *E* is Young's modulus and ρ is the mass density of the beam. We have assumed the material is isotropic; for single-crystal device anisotropy in the elastic constants will result in a resonance frequency that depends upon specific crystallographic orientation.

7. G. Z. Sauerbrey Verwendung von Schwingquarzen zur Wagang dunner Schichten und zur Mikrowagung *Z. Phys.* **155**, 206-222 (1959).

8. H. A. C. Tilmans and M. Elwenspoek, and H. J. Flutiman Micro resonator force gauge. *Sens. Actuators* **A 30**, 35 (1992).

9. For a doubly clamped tube of diameter d, we can calculate the maximum carrier power using $|x_C| = d/\sqrt{2}/\sqrt{0.5Q(1-\nu^2)}$. See A. Husain et al. Nanowire-based very high frequency electromechanical resonator. Appl. Phys. Lett. **83**, 1240 (2003).

10. W. Hansel, P. Hommelhoff, T. W. Hansh, and J. Reichel. Bose-Einstein condensation on microelectronic chips. *Nature* **413**, 498-500 (2001).

11. R. Aebersold and M. Mann Mass spectrometry-based proteomics. *Nature* **422**, 198-207 (2003).

12. W. Gerlach *Naturwiss.* **15**, 15 (1927).

13. G. E. Uhlenbeck and S. A. Goudsmit A problem in brownian motion. *Phys. Rev.* **34**, 145 (1929).

14. Y. K. Yong and J. R. Vig Resonator surface contamination: a cause of frequency fluctuations. *IEEE Trans. on Ultrasonics Ferroelectics and Frequency Control.* **36**, 452 (1989).

15. H. Clark *The Theory of Adsorption and Catalysis* (London, Academic Press, 1970).

16. S. Ross and H. Clark On physical adsorption VI two dimensional critical phenomena of xenon, methane, ethane adsorbed separately on sodium chloride. *J. Am. Chem. Soci.***76**, 4291 (1954).

17. H. J. Kreuzer and Z. W. Gortel *Physisorption Kinetics* (Heidelberg, Springer-Verlag, 1986).

18. S. M. Ross *Stochastic Process* (New York, John Wiley & Sons, 1996).

19. E. L. Elson and D. Magde Fluoresence correlation spectroscopy I concept basis and theory. *Biopolymer* **13**, 1-27 (1974).

20. D. Magde, E. L. Elson, and W. W. Webb Thermodynamic fluctuations in a reacting system- Measurement by fluorescence correlation spectroscopy. *Phys. Rev. Lett.* **29**, 705-708 (1972).

21. I. S. Gradshteyn and I. M. Ryzhik Alan Jefferey, Editor *Table of Integrals, Series, and Products* 5th edition (New York, Academic Press, 1980).

Chapter 4

Experimental Measurement of Phase Noise in NEMS

We present the experimental measurement of phase noise of NEMS. First, we analyze control servo behavior of the phase-locked loop, and give expressions for the locked condition and loop dynamics. We then describe two implementation schemes at very high frequency and ultra high frequency bands: (1) homodyne detection phase-locked loop based on a two port NEMS device and (2) frequency modulation phase-locked loop. The achieved phase noise and Allan deviation are compared with the local oscillator requirement of chip scale atomic clocks to evaluate the viability for such applications. Finally, we investigate the diffusion noise arising from the xenon atoms adsorbed on the NEMS surface by putting a ~190 MHz nanomechanical resonator into a phase-locked loop and measure the frequency noise and Allan deviation.

4.1 Introduction

We have presented the theory of phase noise mechanism of NEMS in chapter 3. So far, to our knowledge, none of *fundamental* noise sources proposed has been measured and very little experimental results are available to decide whether the predicted noise performance of NEMS can indeed be achieved. In this chapter, we address this problem by inserting high *Q* NEMS resonators in phase-locked loops and evaluate their noise performance against controlled variations in their environments.

We start our discussion from analyzing control servo behavior of a general phase-locked loop scheme based on NEMS and give the expressions for the locked condition and loop bandwidth. We then present two electronic implementations of NEMS-based phase-locked loops: (1) homodyne phase-locked loop based on a two port NEMS device and (2) frequency modulation phase-locked loop (FM PLL). These phase-locked loops are designed to lock minute electromechanical resonance of NEMS embedded in a large electrical background as a result of diminishing transducer responsivity as the device dimensions are scaled downward. The achieved noise floor in terms of phase noise density and Allan deviation will be compared with the local oscillator (LO) requirement of chip scale atomic clock (CSAC) to evaluate the viability of NEMS oscillators for this application.[1,2]

Finally, we investigate the diffusion noise arising from the xenon atoms adsorbed on the NEMS surface and measure the corresponding frequency noise and Allan deviation using FM PLL. We will characterize the adsorption behavior, extract the diffusion coefficients, and compare the experimental results with diffusion noise theory and Yong and Vig's model, both described in chapter 3.

4.2 Analysis of Phase-Locked Loop Based on NEMS

In general, two categories of schemes are commonly used for phase noise measurement: self-oscillation and phase-locked loop (PLL). In the self-oscillation scheme depicted in figure 4.1, the resonator operates within a positive feedback loop. The phase noise, manifesting itself in the noise sideband around the carrier, is measured by a spectrum analyzer (see section 2.3). The Allan deviation is calculated from the data taken with the frequency counter. Such a scheme has widely been used to characterize oscillators, and the detailed analysis can be found elsewhere.[3]

In this work, we extensively use the phase-locked loop scheme shown in figure 4.2(a). The principal elements of the loop are voltage control oscillator (VCO) and the resonant response circuitry. The VCO is simply an oscillator whose frequency is proportional to an externally applied voltage. The response function circuitry, containing NEMS and phase detection circuitry, produces a quasi-dc signal proportional to the phase of the mechanical resonance of NEMS. This phase sensitive signal is usually passed through a loop filter, then applied to the control input of the VCO, and serves as error signal to close the feedback loop. If the resonance frequency shifts slightly, the feedback will adjust the control voltage to track the frequency change. Therefore, the voltage fluctuation in the control input of the VCO reflects the frequency noise in the loop. Moreover, the Allan deviation can be obtained from the data taken with the frequency counter.

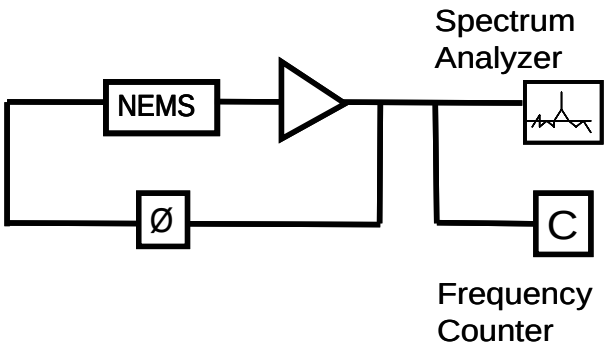

Figure 4.1. Self-oscillation scheme for the phase noise measurement of NEMS. The principal components of the self-oscillation scheme are (1) NEMS, (2) the amplifier, and (3) the phase shifter. The phase noise, manifesting itself in the noise sidebands around the carrier, is measured by a spectrum analyzer. The Allan deviation can be calculated from the data taken with the frequency counter.

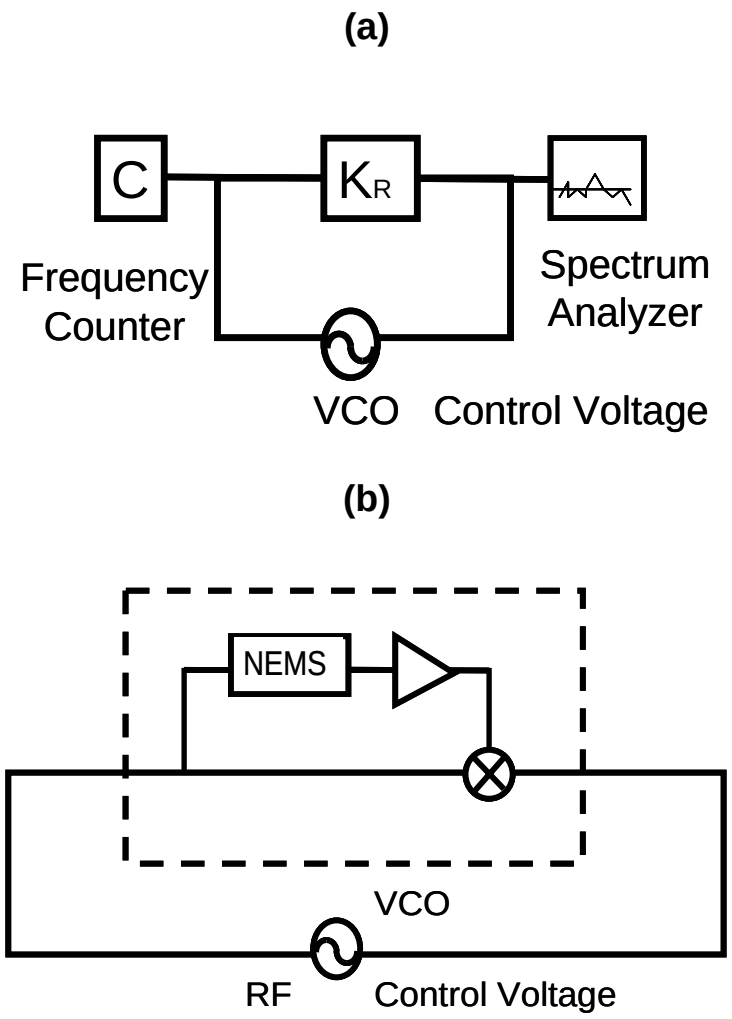

Figure 4.2. Configuration of a phase-locked loop based on NEMS. (a) Measurement scheme of a phase-locked loop (PLL) based on NEMS. The principal components of a PLL are the voltage controlled oscillator (VCO) and the resonant response circuitry (K_R). The output of the resonant response circuitry is used as error signal to the control input of the VCO to close the feedback loop. The frequency noise, manifesting itself as voltage fluctuation in the control port of the VCO, is measured by a spectrum analyzer. The Allan deviation is obtained from the data taken with frequency counter (C). **(b) Homodyne phase-locked loop.** Homodyne phase-locked loop is one example of the scheme shown in (a). In the homodyne phase detection, the NEMS device is driven by a VCO at constant amplitude, and the output is amplified and mixed with the carrier. The resonant response circuitry consists of NEMS, the amplifier, and the mixer.

We now analyze control servo behavior of the PLL, aiming to understand the locked condition and the loop dynamics under the feedback. The frequency of the VCO is determined by the control voltage $V_{control}$, as given by

$$\omega_{VCO} = \omega_{VCO}(V_{control} = 0) + K_V V_{control} . \quad (4.1)$$

K_V and $\omega_{VCO}(V_{control} = 0)$ are the frequency pulling coefficient and the center frequency of the VCO, respectively. The output of the resonant response circuitry can be represented as a voltage function of carrier frequency, $V_R(\omega_C)$, and is applied to the control input of VCO to provide the feedback. We analyze the loop behavior by linearizing $V_R(\omega_C)$ in the vicinity of the resonance frequency, ω_0, of the NEMS as

$$V_R(\omega_C) = K_R(\omega_0 - \omega_C) . \quad (4.2)$$

Here the proportional constant K_R, called henceforth the resonant response coefficient, is defined by $K_R = (\partial V_R / \partial \omega_C)_{\omega=\omega_0}$. When the VCO is locked to the NEMS, we have the condition $V_R = V_{control}$. From equation (4.1) and equation (4.2), we obtain the locked condition

$$\omega_C = \omega_{VCO}(V_{control} = 0) + K_V K_R(\omega_0 - \omega_C) . \quad (4.3)$$

We define the open loop gain of the PLL as

$$K_{loop} = K_V K_R . \quad (4.4)$$

Therefore, equation (4.3) can be rewritten as

$$\omega_C = \frac{K_{loop}}{1 + K_{loop}} \omega_0 + \frac{1}{1 + K_{loop}} \omega_{VCO}(V_{control} = 0) . \quad (4.5)$$

Assuming that VCO is infinitely stable, i.e., $\omega_{VCO}(V_{control} = 0)$ is constant, equation (4.5) implies that any frequency variation in the resonant frequency $\delta\omega_0$ of the device

will be scaled by a factor $K_{loop}/(1+K_{loop})$ as a result of feedback and reflected in the corresponding carrier frequency change $\delta\omega_C$ in the phase-locked loop, i.e.,

$$\delta\omega_C = \frac{K_{Loop}}{1+K_{Loop}}\delta\omega_0 . \tag{4.6}$$

Equation (4.5) also implies an experimental way to measure the loop gain K_{loop}. We rewrite equation (4.5) as

$$\omega_C - \omega_0 = \frac{1}{1+K_{loop}}(\omega_{VCO}(V_{control}=0)-\omega_0) . \tag{4.7}$$

In other words, $\omega_C - \omega_0$ is proportional to $\omega_{VCO}(V_{control}=0)-\omega_0$ with the proportionality constant $1/(1+K_{loop})$. Experimentally one can hold the resonant frequency ω_0 constant, rest the center frequency of VCO, $\omega_{VCO}(V_{control}=0)$, incrementally, and record the carrier frequency ω_C of the loop under lock. By plotting ω_C versus $\omega_{VCO}(V_{control}=0)$, we can determine the loop gain from the slope, i.e., the proportionality constant $1/(1+K_{loop})$.

So far we have considered the locked condition of the PLL in the steady state. We now analyze the loop dynamics and give the expressions for the loop bandwidth. We first discuss the case that a first-order low pass filter with a frequency cutoff, Δf_{filter}, described by the transfer function, $H_{filter}(\omega) = 1/(1+ j(\omega/2\pi\Delta f_{filter}))$, is employed in the control input of the VCO. Repeating the same steps from equation (4.1) to equation (4.5) by replacing K_V with $K_V H_{filter}$, we obtain

$$\omega_C = \frac{K_{loop}/(1+K_{loop})}{1+ j\omega/[(1+K_{loop})2\pi\Delta f_{filter}]}\omega_0 + \frac{1}{1+K_{loop}H_{filter}}\omega_{VCO}(V_{control}=0) . \tag{4.8}$$

Equation (4.8) means that the servo tracks the resonant frequency of the device with the loop bandwidth Δf_{PLL} given by

$$\Delta f_{PLL} = \Delta f_{filter}(1 + K_{loop}) . \tag{4.9}$$

Now we can write down the intrinsic bandwidth of the PLL limited by the NEMS itself. This is done by simply replacing Δf_{filter} in equation (4.9) with the resonant bandwidth $(\omega_0 / 2\pi Q)$ in the loop.[3] As a result, the intrinsic bandwidth of the PLL is given by

$$\Delta f_{PLL} = (\omega_0 / 2\pi Q)(1 + K_{loop}) . \tag{4.10}$$

Both equation (4.9) and equation (4.10) imply that the effect of feedback enhances the bandwidth by the factor $1 + K_{loop}$. For applications requiring fast response time, we can always increase the loop gain to extend the loop bandwidth. Similar ideas have also been used to enhance the bandwidth of atomic force microscopy by Albrecht et al.[3]

Finally, we give the explicit expression for the resonant response coefficient. The resonant response function, $V_R(\omega_C)$, is determined by the transducer voltage from NEMS, $V_{transducer}(\omega_C)$, cascaded by the amplifier gain, K_A, and the gain of phase detection circuitry, K_P, as given by

$$V_R(\omega_C) = V_{transducer}(\omega_C) K_A K_P . \tag{4.11}$$

Taking the derivative of the resonant response function with respect to the carrier frequency, the resonant response coefficient is given by

$$K_R \equiv (\partial V_R / \partial \omega_C)_{\omega_C = \omega_0} = (\partial V_{transducer} / \partial \omega)_{\omega_C = \omega_0} K_A K_P . \tag{4.12}$$

As an example, we give the expression of resonant response coefficient for homodyne phase-locked loop. The homodyne phase-locked loop shown in figure 4.2(b) is

one incarnation of the scheme shown in figure 4.2(a). In such a scheme, the NEMS device is driven by a VCO at constant amplitude and the output is amplified and mixed with the carrier. We first give the expression for the resonant response coefficient K_R. The gain of the phase detection circuitry K_P is given by the mixer gain K_M. $\partial V_{transducer} / \partial \omega_C$ can be approximated by $QV_{transducer}^{\max} / \omega_0$. $V_{transducer}^{\max}$ is the maximum transducer voltage producing linear response. Thus, the loop gain of the PLL is given by

$$K_R = K_M K_A Q V_{transducer}^{\max} / \omega_0 . \tag{4.13}$$

In the magnetomotive transduction, $V_{transducer}^{\max}$ is given by the electromotive force (emf) voltage generated across the device with length L vibrating with the amplitude $|x_C|$ at the frequency ω_0 in the magnetic field B, i.e.,

$$V_{transducer}^{\max} = BL\omega_0 |x_C| . \tag{4.14}$$

PLL	Frequency	Dimensions($L \times w \times t$)	Q	M_{eff}	DR	σ_A(1sec)	Δf
Two Port	125 MHz	1.6 μm × 800 nm × 70 nm	1300	1 pg	80 dB	4×10^{-7}	165 kHz
FM VHF	133 MHz	2.3 μm × 150 nm × 70 nm	5000	100 fg	80 dB	5×10^{-8}	32 Hz
FM VHF	190 MHz	2.3 μm × 150 nm × 100nm	5000	150 fg	80 dB	1×10^{-7}	32 Hz
FM UHF	419 MHz	1.35 μm × 150 nm × 70 nm	1000	50 fg	100 dB	1×10^{-7}	32 Hz

Table 4.1. Summary of parameters of all phase-locked loops based on NEMS presented in this work

4.3 Homodyne Phase-Locked Loop Based upon a Two-Port NEMS Device

We now present the electronic implementation of the homodyne phase-locked loop based on the scheme shown in figure 4.2(b) using a two port NEMS device, who parameters are summarized in table 4.1. In practice, the two port topology avoids direct electrical feedthrough of the simple one port scheme and allows careful design of the bonding fixture to minimize the unwanted parasitic coupling that produces a large electrical background on top of electromechanical resonance. Figure 4.3(a) shows the SEM micrograph of the two port device fabricated from SiC epilayer with Au metallization.[4] It is driven magnetomotively and the resonant frequency is found to be ~125 MHz with quality factor Q=1300. Figure 4.3(b) shows the fundamental mode of vibration of a two port device, optimized through the finite element simulation.

Figure 4.4 shows the electronic implementation of the PLL. The low phase noise VCO (Minicircuits POSA-138) drives the NEMS device at constant amplitude and the output of the transducer of the NEMS is amplified by a low noise preamplifier (Miteq AU1442). We further employ an external bridge, consisting of a variable phase shifter and a variable attenuator, to null out the electrical background. Figure 4.5 shows the resulting mechanical resonant response of the NEMS after the nulling. The rising background away from resonance shows the narrowband nature of the nullling, and hence the locking range of the loop is limited within the natural width of the resonance due the finite bandwidth of the variable phase shifter in the external bridge.The signal from the external bridge is then mixed down with the carrier, amplified by an instrumentation amplifier (Stanford Research Systems SR560), offset by a precision bias circuit, and fed into the control input of the VCO to close the feedback control loop. Note

that the cutoff frequency of the low pass filter in the control servo is set to 1 MHz to fully utilize the intrinsic bandwidth, $(1+K_{loop})(\omega_0/2\pi Q)$=165 kHz, provided by the NEMS device (K_{loop} approximately equals to 1). Hence this scheme is very desirable in sensing applications requiring fast response.

Figure 4.6 shows the phase noise spectrum of the VCO in PLL as measured by spectrum analyzer (Hewlett Packard HP8563E). At frequencies between 100 Hz and 20 kHz, the spectrum exhibits flicker noise and has $1/f^3$ dependence on the offset frequency due to the upconversion of the flicker noise of the preamplifier to the sideband of the carrier. Above 20 kHz, the spectrum flattens out to about -110dBc/Hz, the instrument noise floor of the spectrum analyzer.

Figure 4.7 shows the Allan deviation versus averaging times from frequency data over the course of ~1000 sec interval taken with the frequency counter. At the logarithmic scale, the observed Allan deviation, is nominally independent of averaging time and confirms the flicker noise in the phase noise spectrum. Note that the error bar of the each data point represents the confidence interval of the Allan deviation, given by $\sigma_A(\tau_A)/\sqrt{N_S-1}$. For τ_A= 1 sec, the observed Allan deviation $\sigma_A(\tau_A)$=4.7 x 10^{-7} is consistent with the estimated value 7.7 x 10^{-7} from the theoretical expression $\sigma_A(\tau_A)=(1/Q)10^{-DR/20}$ (with dynamic range DR=80 dB and Q=1300). In the present experiment, DR is limited by (extrinsic) transducer-amplifier noise and the onset of the Duffing instability of the NEMS device.

(a)

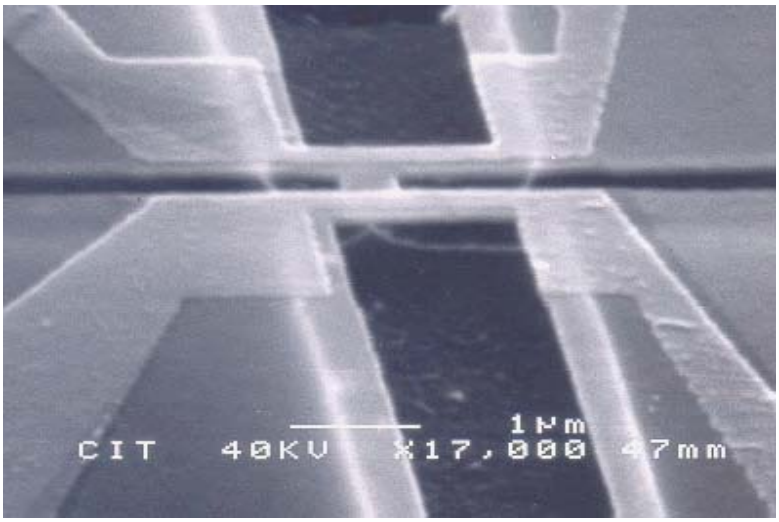

(b)

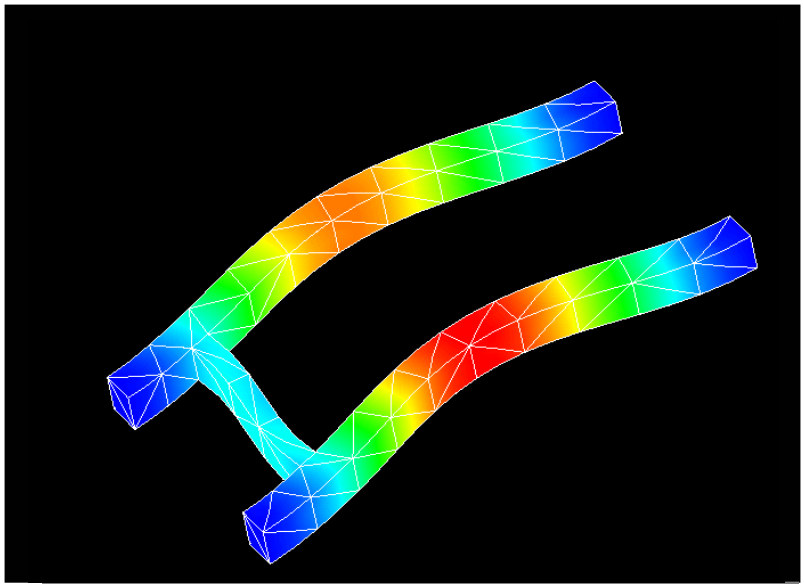

Figure 4.3. Pictures of two-port NEMS devices. (a) SEM micrograph of the two port NEMS device. The device is fabricated from SiC epilayer with Au metallization. **(b) Finite element simulation of the fundamental mode of vibration of a two port device.** The two port device consists of two doubly clamped beams mechanically coupled by a central beam. We use the finite element simulation to optimize the mechanical design.

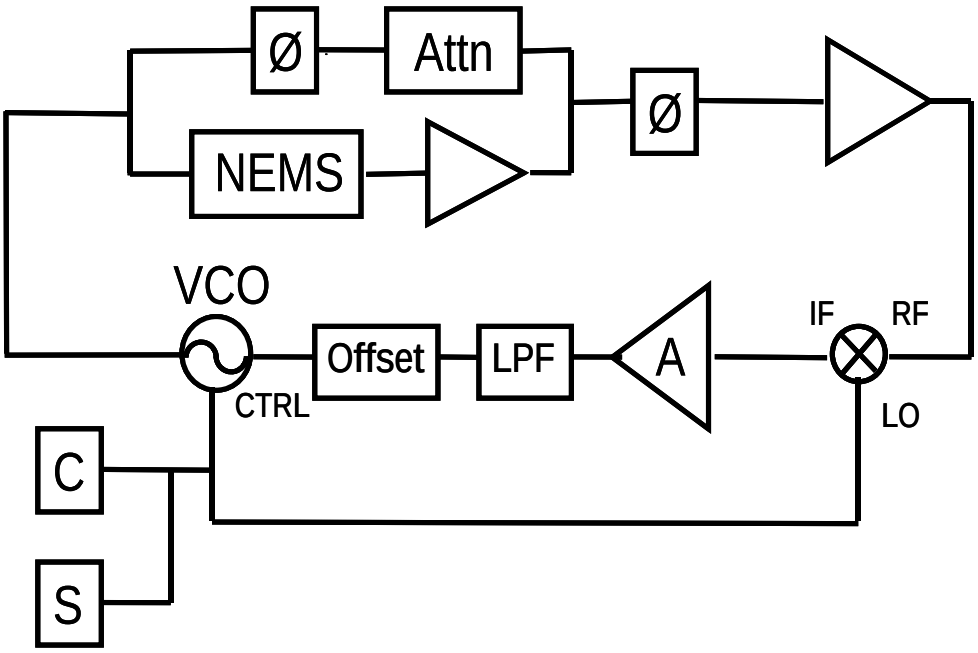

Figure 4.4. Implementation of the homodyne phase-locked loop based on a two-port NEMS device. We use a two port NEMS device with external bridge to implement the homodyne phase-locked loop. The external bridge, comprised of a narrowband voltage controlled phase shifter (ϕ) and a voltage controlled variable attenuator (Attn), is used to null the electrical background.

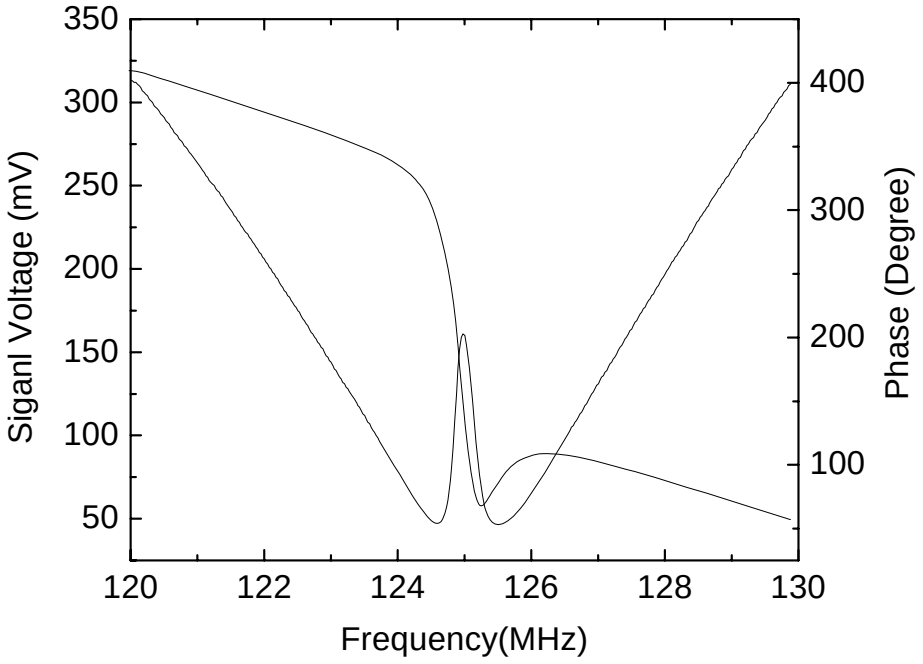

Figure 4.5. Mechanical resonant response after nulling. The mechanical resonance of the NEMS at 125 MHz is shown after the constant electrical background is nulled out by an external bridge circuit. The rising background away from resonance shows the narrowband nature of the nullling due to the bandwidth of the variable phase shifter in the external bridge. This limits our locking range within the natural width of the resonance.

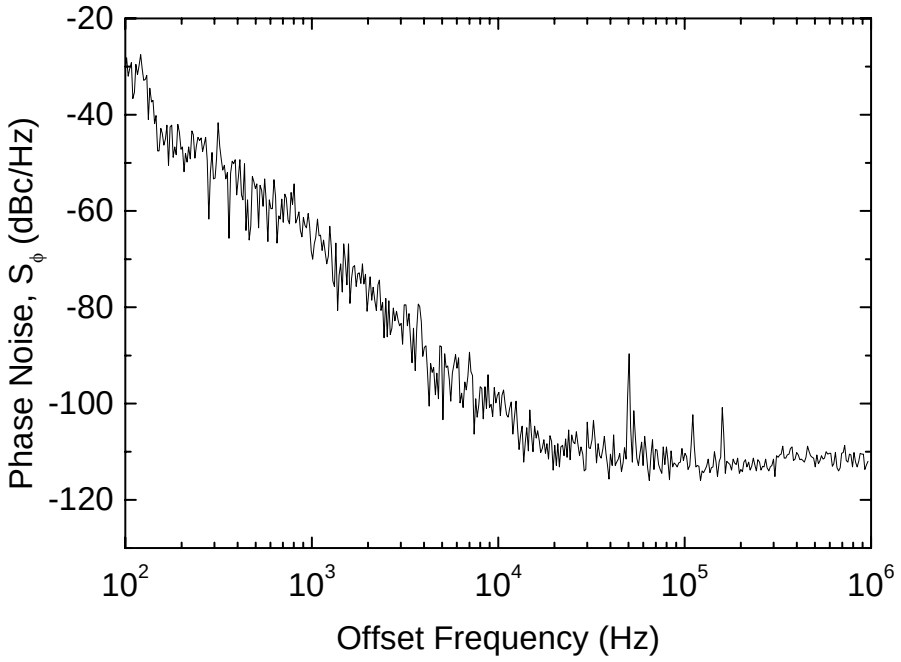

Figure 4.6. Phase noise density of the 125 MHz homodyne phase-locked loop based on a two-port NEMS device. The phase noise density of the 125 MHz homodyne phase-locked loop based on a two port NEMS is shown. Between 100 Hz and 20 kHz, the phase noise spectrum exhibits flicker noise, i.e., having $1/f^3$ dependence on the offset frequency. Above 20 kHz, it flattens out to ~110 dBc/Hz, the instrument noise floor of the spectrum analyzer.

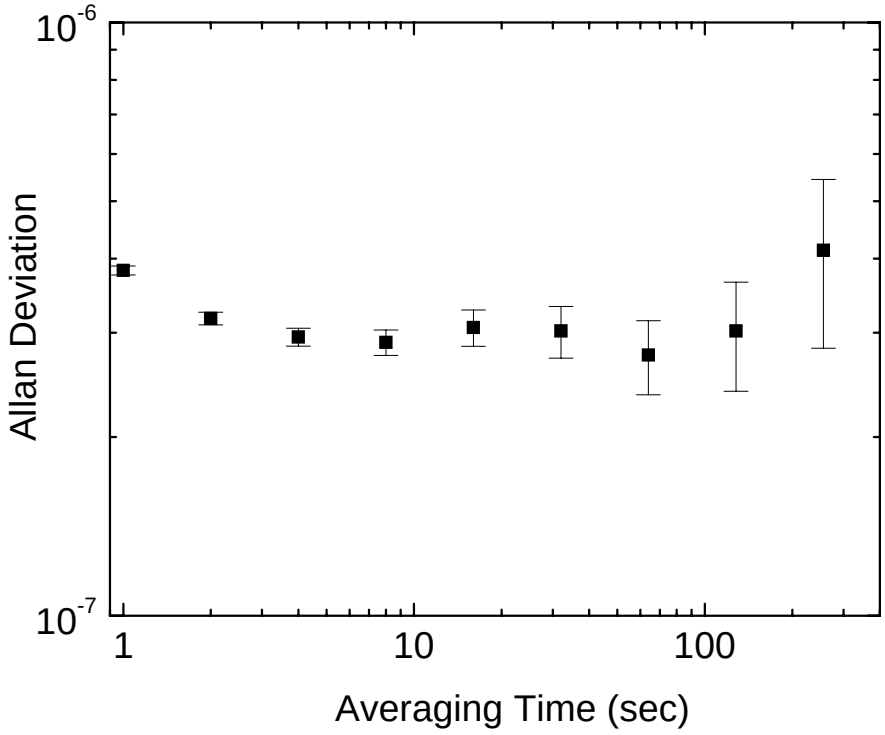

Figure 4.7. Allan deviation of the 125 MHz homodyne phase-locked loop based on a two-port NEMS device. The Allan deviation of 125 MHz homodyne phase-locked loop versus averaging time, calculated from frequency data over the course of ~1000 sec interval, is shown. At logarithmic scale, the Allan deviation is nominally independent of averaging time and consistent with the observed flicker noise in the phase noise spectrum in figure 4.6. The error bar in each data point represents the one-standard-deviation confidence interval of the Allan deviation.

4.4 Frequency Modulation Phase-Locked Loop

We now present the analysis and implementation of the frequency modulation phase-locked loop, which is designed to lock the even smaller electromechanical resonance of a NEMS embedded in a large electrical background. Roughly speaking, the frequency modulation of the carrier and subsequent demodulation by lock-in detection after mixer generates an electrical signal proportional to the derivative of the resonant response with respect to frequency. As a result, the constant electrical background, in which the electromechanical resonance of the NEMS is embedded, is nulled out. As shown in figure 4.8, the FM PLL is formed by adding frequency modulation of the carrier and lock-in detection to the homodyne phase-locked loop. One can prove that addition of the frequency modulation and lock-in detection contributes to K_R with two additional gain factors, the frequency modulation index M and the lock-in detection gain K_{Lockin}. By inserting these two factors into equation (4.13), we find

$$K_R = (K_M K_A Q V_{transducer}^{\max} / \omega_0) M K_{Lockin} . \tag{4.15}$$

Note that $M = V_m K_V / \omega_m$ in the case that a sinusoidal voltage of magnitude V_m at modulation frequency, ω_m is applied to the control voltage port of VCO.

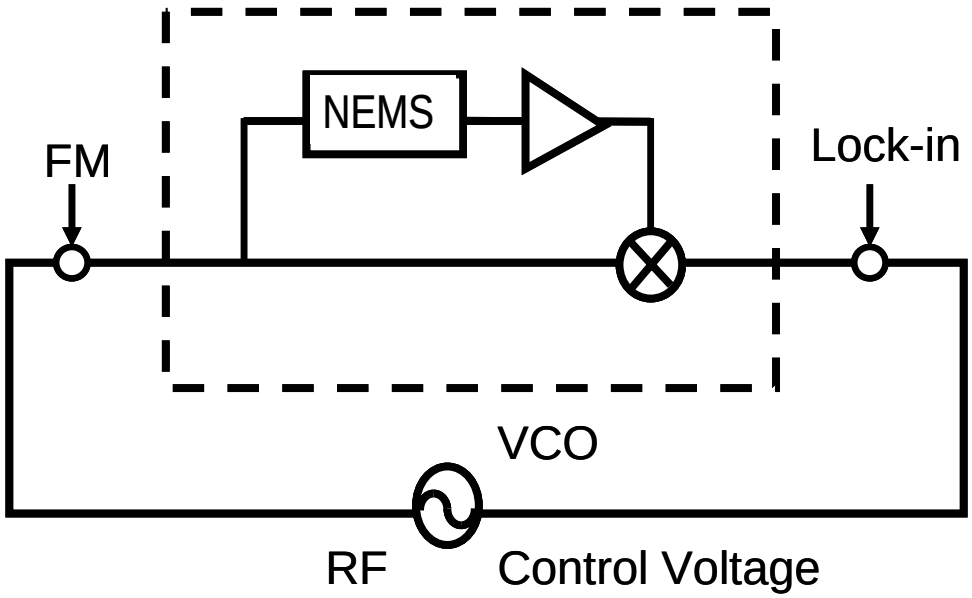

Figure 4.8. Conceptual diagram of frequency modulation phase-locked loop (FM PLL) scheme. Similar to homedyne phase-locked loop, the NEMS is driven by a VCO at constant amplitude, and the output is amplified and mixed with the carrier. The FM PLL is formed by adding the frequency modulation (FM) of the carrier and the lock-in detection to the homodyne phase-locked loop.

Figure 4.9 shows the electronic implementation of the FM PLL at VHF (very high frequency) band for 133 MHz and 190 MHz devices. The device configurations are summarized in table 4.1. We detect the mechanical resonance in the reflection scheme by a directional coupler. The signal from the NEMS device is amplified by a radio frequency (RF) amplifier with gain, K_{RF}, shifted in phase by the phase shifter, and subsequently mixed down to intermediate frequency (IF) by a mixer. The IF signal is further amplified by an IF amplifier with gain, K_{IF}. The total amplifier gain is given by

$$K_A = K_{RF} K_{IF} . \tag{4.16}$$

In our experiment, the carrier is modulated at 1.2652 kHz with reference oscillator in the lock-in amplifier. The lock-in amplifier (Stanford Research Systems SR830) is employed to detect the signal amplitude at the modulation frequency and subsequently rescale the readout according to the *Sensitivity* setting with full scale voltage $V_{fullscale}$. This is further divided by a voltage divider with a dividing factor *DF*. For convenience, we incorporate the voltage division and rescaling into the lock-in detection gain

$$K_{lockin} = (1/DF) V_{fullscale} / Sensitivity . \tag{4.17}$$

We summarize the experimental parameters used in FM PLL at 190 MHz in table 4.2. To close the feedback loop, the lock-in amplifier outputs the signal to the control port of the VCO. We use the frequency synthesizer (Hewlett Packard HP8648) in frequency modulation mode as the VCO. This imposes a proportional control with a frequency cutoff proportional to the inverse of the lock-in time constant τ_{lockin}. More precisely, the bandwidth of the FM PLL is given by $\Delta f_{PLL} = (1 + K_{loop})(1/2\pi\tau_{lockin})$ using equation (4.9) as a result of feedback. In addition, a digital feedback loop is established by a computer

interface, which periodically checks the digital output of the lock-in amplifier, computes a correction, and resets the center frequency of the VCO accordingly with prescribed loop gain and loop time. Effectively one has a discrete integral control, extending the locking range beyond the natural width of the resonance. We use it to follow the frequency shift induced by large changes in device mass over extended measurement intervals.

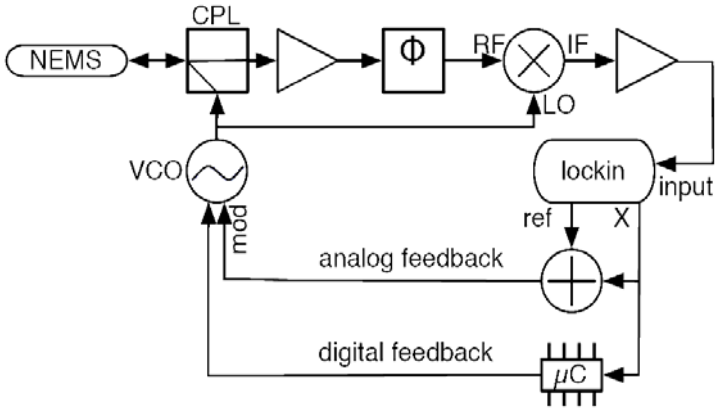

Figure 4.9. Implementation of frequency modulation phase-locked loop (FM PLL) scheme. We employ frequency modulation phase-locked loop (FM PLL) scheme to track the resonant frequency of the device. The mechanical resonance is detected in a reflection scheme, by using a directional coupler (CPL). The reflected signal is amplified, phase shifted (Φ), and mixed down (⊗). We modulate the carrier at 1.2652 kHz and employ a lock-in amplifier (Stanford Research Systems SR830) for demodulation. The resulting output (X) provides the analog feedback to the VCO (Hewlett Packard HP8648B). A computer-controlled parallel digital feedback (μC) is implemented for applications requiring a large locking range.

Figure 4.10 shows the phase noise spectrum of the FM PLL based on the 190 MHz device. At frequencies between 15 mHz and 30 Hz, the spectrum exhibits flicker noise, having $1/f^3$ dependence on the offset frequency. Above 30 Hz, the spectrum rolls off at the slope of 50 dB/decade, reflecting the loop bandwidth limited by the filter in lock-in detection. With the lock-in time constant τ_{lockin} = 10 ms and K_{loop} =1, we estimate the loop bandwidth to be 32 Hz from the expression $\Delta f_{PLL} = (1+K_{loop})(1/2\pi\tau_{lockin})$. Figure 4.11 shows the observed Allan deviation calculated from data over the course of one hour taken with frequency counter (Agilent 53132) for τ_A ranging from 1 sec to 128 sec. At the logarithmic scale, the observed Allan deviation versus averaging time is nominally constant and thus consistent with flicker noise in the phase noise spectrum in Figure 4.10. The Allan deviation $\sigma_A(\tau_A)$=1x10^{-7} for τ_A= 1 sec is close to the estimated value 2x10^{-7} from the expression $\sigma_A(\tau_A) = (1/Q)10^{-DR/20}$ (with dynamic range *DR* = 80 dB and *Q*= 5000).

We have also implemented the FM PLL at the ultra high frequency (UHF) band at 419 MHz. For the 419 MHz SiC device with dimensions 1.35 um(*L*) x 150 nm(*w*) x 70 nm (*t*) and *Q*=1600, the mechanical impedance is only ~0.08 Ω and embedded in a large electrical impedance ~100 Ω. To detect such a small impedance at the UHF band, we replace the simple reflection scheme used for FM PLL at the VHF band with a balanced bridge detection (see also chapter 7).[5] To amplify the signal from the NEMS device, we employ a cryogenic amplifier (Miteq AFS3-00100200-09-CR-4), working from 0.1 to 2 GHz with the equivalent noise temperature T_N =10 K at 419 MHz. We summarize the experimental parameters in table 4.2. Figure 4.12 shows the observed phase noise

spectrum. At frequencies between 15 mHz and 30 Hz, the spectrum exhibits $1/f^2$ dependence on the offset frequency. Similar to the FM PLL at VHF band, the additional rolloff in the spectrum at 30 Hz results from the loop bandwidth $\Delta f_{PLL} = (1 + K_{loop})(1/2\pi\tau_{lockin})$=32 Hz (with τ_{lockin} = 10 ms and K_{loop}=1). Figure 4.13 shows the Allan deviation calculated from the frequency data over the course of one hour taken with the frequency counter (Agilent 53132). For τ_A=1 sec, the observed Allan deviation σ_A=1 x 10^{-7} is much higher than the estimated value of 6.25 x 10^{-9} from the expression $\sigma_A(\tau_A) = (1/Q)10^{-DR/20}$ with *DR*=100 dB and *Q*=1000. (*DR* is estimated assuming the white noise contribution from the cryogenic amplifier with equivalent noise temperature T_N=10 K at 419 MHz and onset of Duffing nonlinearity of the NEMS.) We attribute this discrepancy to the conversion of other noise sources to side band of the carrier through the mixer or the nonlinearity of the circuit.

Table 4.2. Summary of experimental parameters used in the frequency modulation phase-locked loops (FM PLL) at very high frequency (VHF) and ultra high frequency (UHF) bands

Parameter	Symbol	VHF PLL	UHF PLL
Resonant Frequency	$\omega_0/2\pi$	190MHz	419MHz
Quality Factor	Q	5000	1600
Transducer Voltage	$V_{transucer}^{max}$	~1μV	~1μV
RF Gain	K_{RF}	35dB	45dB
IF Gain	K_{IF}	500	500
Mixer Gain	K_M	~0.1	~0.1
Modulation Frequency	$\omega_m/2\pi$	1.3kHz	10kHz
Modulation Voltage	V_m	30mV	30mV
Frequency Pulling Coefficient	K_V	100kHz/V	50kHz/V
Sensitivity	*Sensitivity*	200mV	1 mV
Dividing Factor	*DF*	10	10
Full Scale Voltage	$V_{fullscale}$	10V	10V
Lock-in Time Constant	$\tau_{lock\text{-}in}$	10ms	10ms
Modulation Index	M	2.3	0.15
Loop Gain (Estimated)	K_{loop}	~4.8	~4.5
Loop Gain (Measured)	K_{loop}	~1	~1

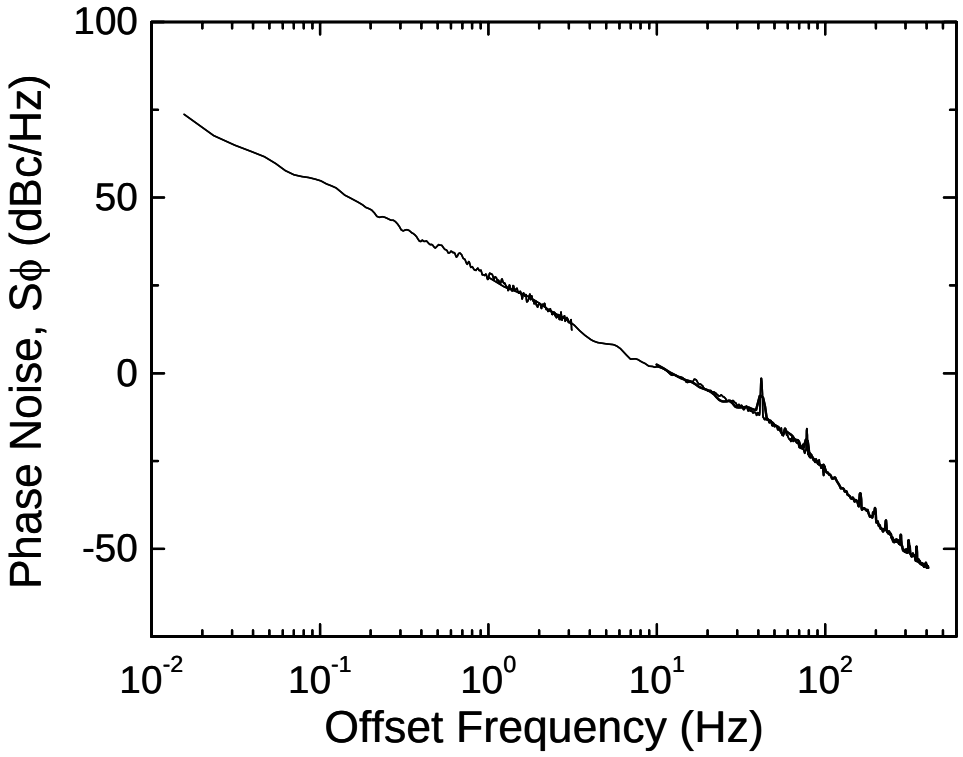

Figure 4.10. Phase noise density of the 190 MHz frequency modulation phase-locked loop (FM PLL). The phase noise density of the 190 MHz FM PLL is shown. Between 15 mHz and 30 Hz , the phase noise spectrum of the 190 MHz phase-locked loop exhibits flicker noise, i.e., having $1/f^3$ dependence on the offset frequency. Above 30 Hz, it rolls off at the slope of 50 dB/decade due to the loop bandwidth limited by lock-in detection $\Delta f_{PLL} = (1 + K_{loop})(1/2\pi\tau_{lock-in})$ =32 Hz (with $\tau_{lock-in}$ =10 ms and K_{loop} =1).

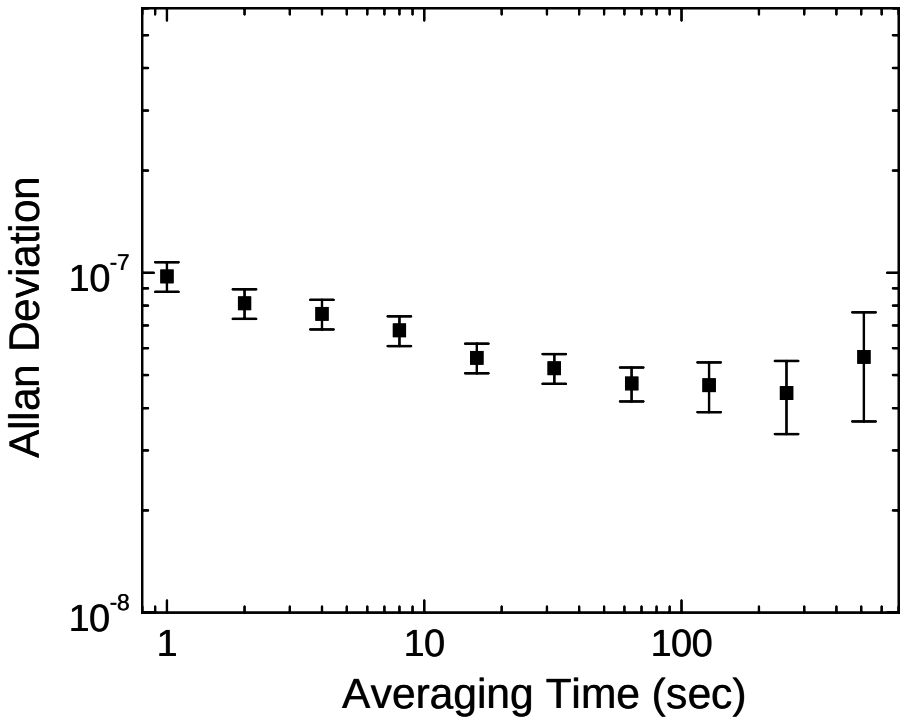

Figure 4.11. Allan deviation of the 133 MHz frequency modulation phase-locked loop (FM PLL). The Allan deviation of the 133 MHz FM PLL versus averaging time, calculated from frequency data over the course of one hour, is shown here. At logarithmic scale, the Allan deviation is nominally independent of averaging time and thus consistent with the observed flicker noise in the phase noise spectrum. The error bar in each data point represents the one-standard-deviation confidence interval of the Allan deviation.

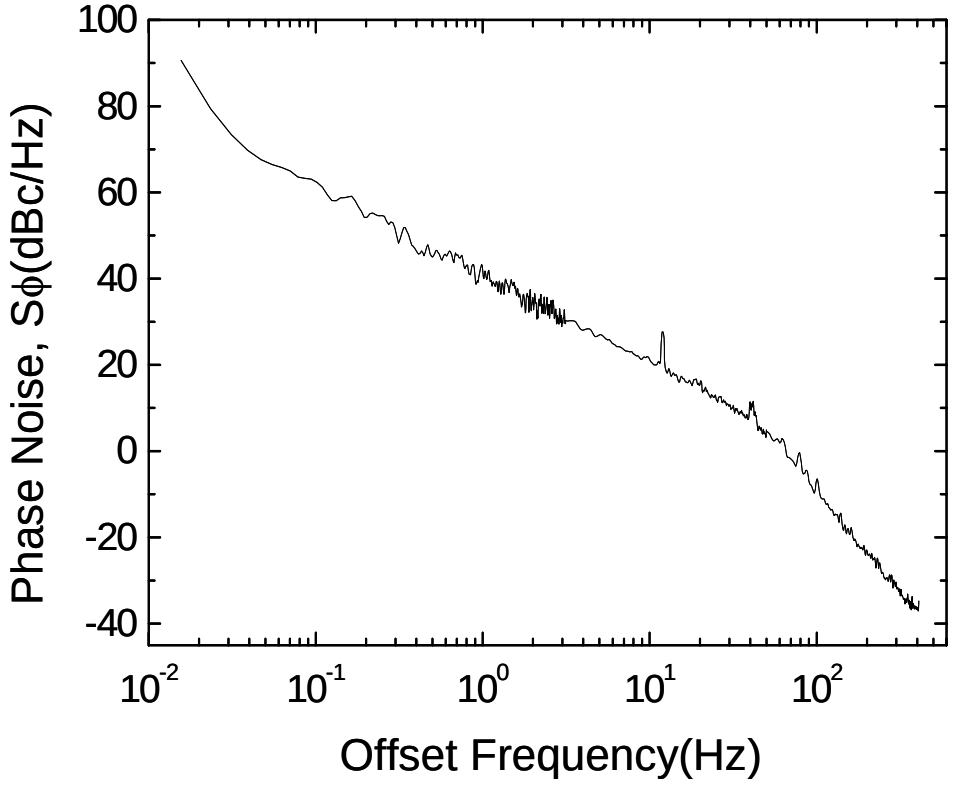

Figure 4.12. Phase noise density of the 419 MHz frequency modulation phase-locked loop (FM PLL). The phase noise density of the 419 MHz FM PLL is shown. Between 15 mHz and 30 Hz, the phase noise spectrum of the 419 MHz phase-locked loop exhibits white noise, having $1/f^2$ dependence on offset frequency. Above 30 Hz, it rolls off at the slope of 40 dB/decade due to the loop bandwidth limited by lock-in detection $\Delta f_{PLL} = (1 + K_{loop})(1/2\pi\tau_{lock-in})$ =32 Hz (with $\tau_{lock-in}$ =10 ms and K_{loop} =1).

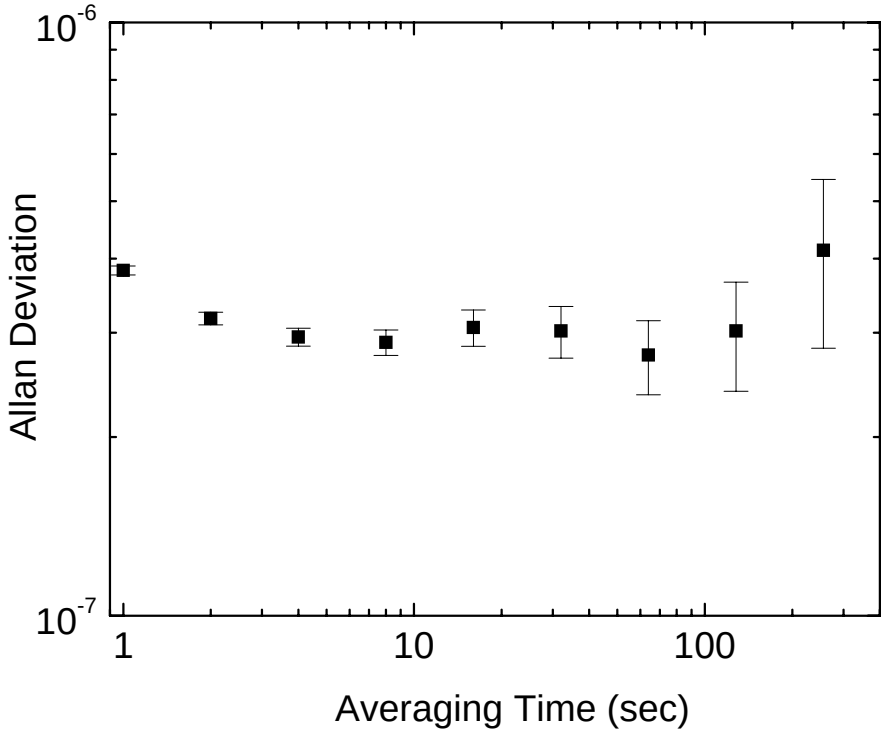

Figure 4.13. Allan deviation of the 419 MHz frequency modulation phase-locked loop (FM PLL). The Allan deviation of the 419 MHz FM PLL versus averaging time, calculated from frequency data over the course of one hour, is shown here. The error bar in each data point represents the one-standard-deviation confidence interval of the Allan deviation.

4.5 Comparison with Local Oscillator Requirement of Chip Scale Atomic Clock

The chip scale atomic clock is the vapor cell atomic clock, scaled down to microelectronic chip size.[6] The operation of CSAC requires a LO to interrogate the atomic transitions to provide the frequency precision. The frequency reference configuration consists of the physics package, the control circuitry, and the LO. In the physics package, the hyperfine transition of the atoms in the vapor cell is induced by a vertical cavity surface emitting laser (VCSEL), modulated at microwave frequency. The optical transmission is subsequently sensed by a semiconductor detector to produce a microwave signal, which is phase locked to the LO to optimize the long term and short term frequency stabilities through the control circuitry. Due to their small size and low operating power, NEMS oscillators are very promising candidates as the LO for CSAC, so it is interesting to compare our achieved noise floor with the LO requirement and evaluate their viability for such applications.

Kitching calculates the LO requirement by demanding that the fractional frequency instability of the CSAC satisfy the DAPRA program goal of 10^{-11} for one hour averaging time.[5] Figure 4.14 shows the phase noise floor of the LO requirement using the hyperfine transitions of Rb^{87} at frequency 6.8 GHz together with the measured phase noise spectra of all the phase-locked loops presented so far, properly scaled to 6.8 GHz. Although the high frequency (>20 kHz) and low frequency (<0.5 Hz) ends of the spectra barely meet the requirement, the middle band between 0.5 Hz and 20 kHz is still 40 dB higher than the requirement. This is due to extrinsic transducer amplifier noise in our still unoptimized experimental configuration. Also shown in figure 4.14 are the projected phase noise spectra of 400 MHz NEMS-based oscillators with $Q = 10^4$ and $Q = 10^5$,

limited by thermomechanical noise at room temperature. They are certainly able to meet the requirements of CSAC with at least 30 dB margin at all frequencies.

Figure 4.15 shows the corresponding Allan deviations of all phase-locked loops versus averaging time τ_A, and the LO requirement. For τ_A longer than 1 sec, all the experimentally achieved Allan deviations already meet the LO requirement. For $\tau_A < 1$ sec, the only available Allan deviation data for the 419 MHz PLL exhibits $1/\sqrt{\tau_A}$ dependence on the averaging time, which is worse than the LO requirement. Also shown in figure 4.15 are the projected Allan deviations of 400 MHz NEMS-based oscillators for Q=10^4 and Q=10^5, limited by thermomechanical noise at room temperature. They are certainly able to meet the LO requirement for all averaging times ranging from 10^{-7} sec to 100 sec. Meeting the LO requirement in terms of both phase noise spectra and Allan deviations clearly demonstrate the viability of the NEMS oscillators as the LO for CSAC.

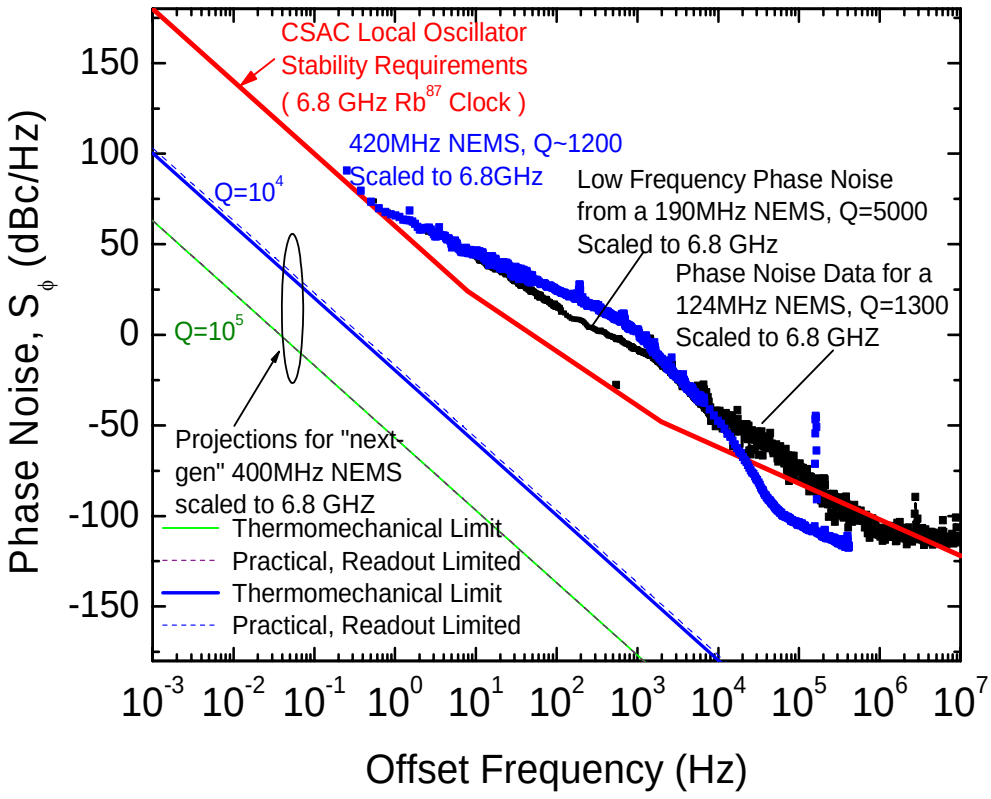

Figure 4.14. Phase noise spectrum of NEMS-based phase-locked loops versus the local oscillator (LO) requirement of chip scale atomic clock (CSAC). The measured phase noise spectra of 125 MHz, 190 MHz and 419 MHz phase-locked loops based on NEMS are compared to the LO requirement of CSAC, upon proper scaling to 6.8 GHz. The projected phase noise spectra of 400 MHz NEMS oscillators with Q=10^4 and Q=10^5, limited by thermomechanical fluctuations at room temperature, clearly shows the ability to meet the CSAC requirement.

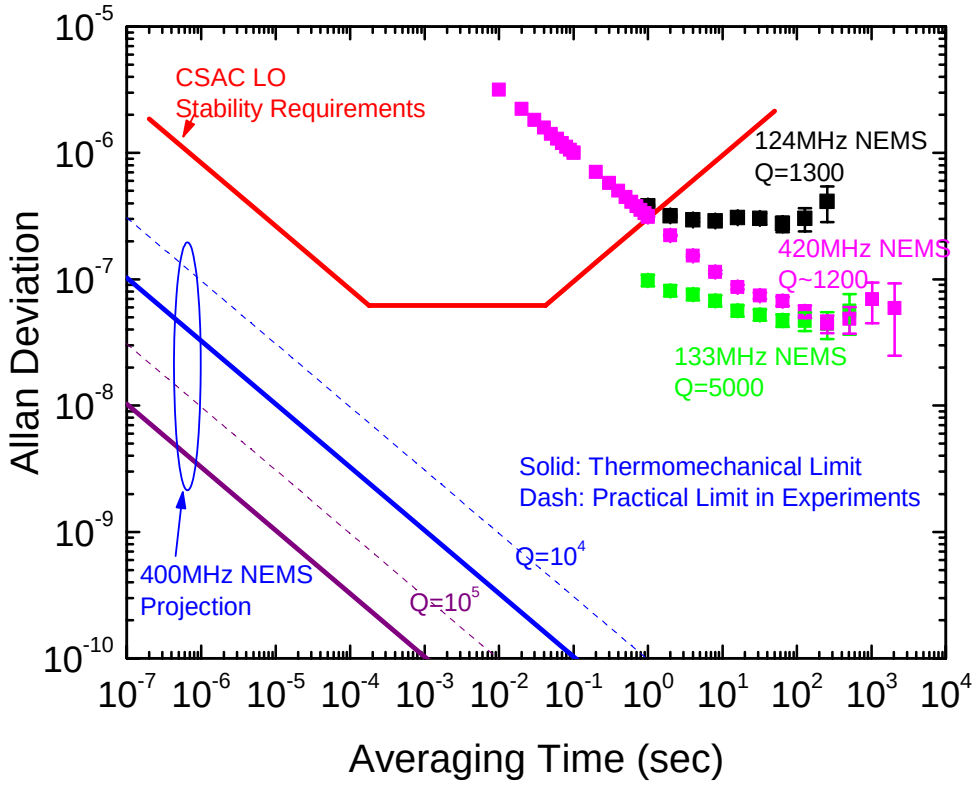

Figure 4.15. Allan deviations of NEMS-based phase-locked loops versus the local oscillator (LO) requirement of chip scale atomic clock (CSAC). The measured Allan deviations of 125 MHz, 190 MHz and 419 MHz phase-locked loops based on NEMS are compared to the LO requirement of CSAC. The projected Allan deviations of 400 MHz oscillators based on NEMS of Q=10^4 and Q=10^5, limited by thermomechanical fluctuations at room temperature, clearly meet the LO requirement of CSAC.

4.6 Experimental Measurement of Diffusion Noise

We have analyzed many noise processes in detail in chapter 3. All these noise processes arise from local fluctuation of the intrinsic thermodynamic properties of a physical system in equilibrium.[7] Although these fluctuations become noise which limits NEMS performance as sensors or resonators, they also provide a potential source of information.[8,9] The fluctuation around the thermodynamic mean is proportional to the number of independent accessible degree of freedom. Moreover, the spectral density of fluctuations is precisely governed by the dynamic parameters of the systems as generally expressed by the fluctuation-dissipation theorem.[7] In particular, when gaseous species adsorb on a NEMS device, typically from the surrounding environment, they can diffuse along the surface in and out of the device. Thus the number of adsorbed atoms in the device can fluctuate, which translates into mass fluctuation and hence frequency fluctuations. The noise spectrum in this case is governed by the diffusion time. We have proposed the diffusion noise theory of NEMS in section 3.5. Here we demonstrate the experimental measurement of the diffusion noise arising from adsorbed xenon atoms on NEMS surface.

We incorporate the NEMS device into a low-noise FM PLL circuit (see section 4.4). Data are obtained from a NEMS resonator with fundamental resonant frequency f_0~190 MHz and dimensions, 2.3 μm (L) × 150 nm (w) × 100 nm (t). (The surface area of the device is A_D=3.45x10^{-13} m^2.) The device is a doubly clamped beam patterned from SiC epilayers[4] and capped with thermally evaporated dual metallic layers: 30 nm Al (bottom) and 5 nm Ti (top). (The effective vibratory mass of the device, including the metallic layers, is M_{eff}=96 fg.) After fabrication, the device is loaded into a UHV

cryostat, actuated magnetomotively,[4] and exhibits Q of ~5000 for the fundamental in-plane flexural mode of vibration at the measurement temperatures ~58 K.

Xenon is used in our experiments due to its large atomic mass (m_{Xe}=130 amu), and its well characterized surface behavior in literature.[10-14] A gas nozzle is used to deliver a constant, calibrated flux to the device (see also section 5.2). The flux to the device, Φ, is 2.65×10^{17} atom/m^{2}sec, corresponding to an effective pressure of 6.6×10^{-8} torr at 58 K. Data presented here are taken at constant flux, while changing the temperature of the device.

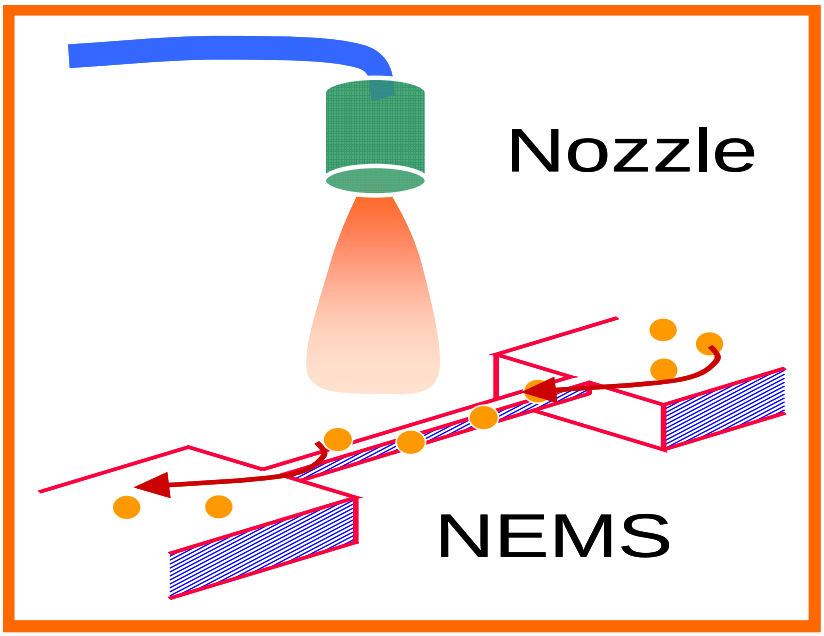

Figure 4.16. Experimental configuration for diffusion noise measurement. A gas nozzle with a 300 μm aperture provides a controlled flux of atoms or molecules. The flux is determined by direct measurements of the gas flow rate, in conjunction with a well-validated model for the molecular beam emanating from the nozzle.

First, we measure the adsorption spectrum, defined as the total number of adsorbed xenon atoms versus temperature. As the device is cooled below 57 K, we observe irreversible accumulation of xenon in solid phase due to the two-dimensional solid-gas phase transition.[11] The adsorption of xenon is fully reversible above this transition temperature. All the measurements are thus done above 57 K. We take the resonance frequency data of the device versus temperature with applied flux and without flux, denoted by $f_G(T)$ and $f_{NG}(T)$, respectively. The adsorption spectrum is deduced from the frequency change by $N(T) = -m_{Xe}(f_G(T) - f_{NG}(T)/(\Re/2\pi)$ due to the presence of gas, where $\Re/2\pi = f_0/2M_{eff} = 0.99$ Hz/zg is the mass responsivity of the device.[15] The coverage θ, defined as the number of adsorbed atoms per unit area, i.e., $N(T)/A_D$, is 6.67×10^{14} atoms/cm^2 at T=58 K, consistent with a commensurate monolayer coverage of 5×10^{14} atoms/cm^2 on Pt(111) at T=85 K.[13] Because the roughness of thermally evaporated Ti top layer of the device completely blurs the monolayer transition of xenon, we do not observe such a transition in the adsorption spectrum.[2]

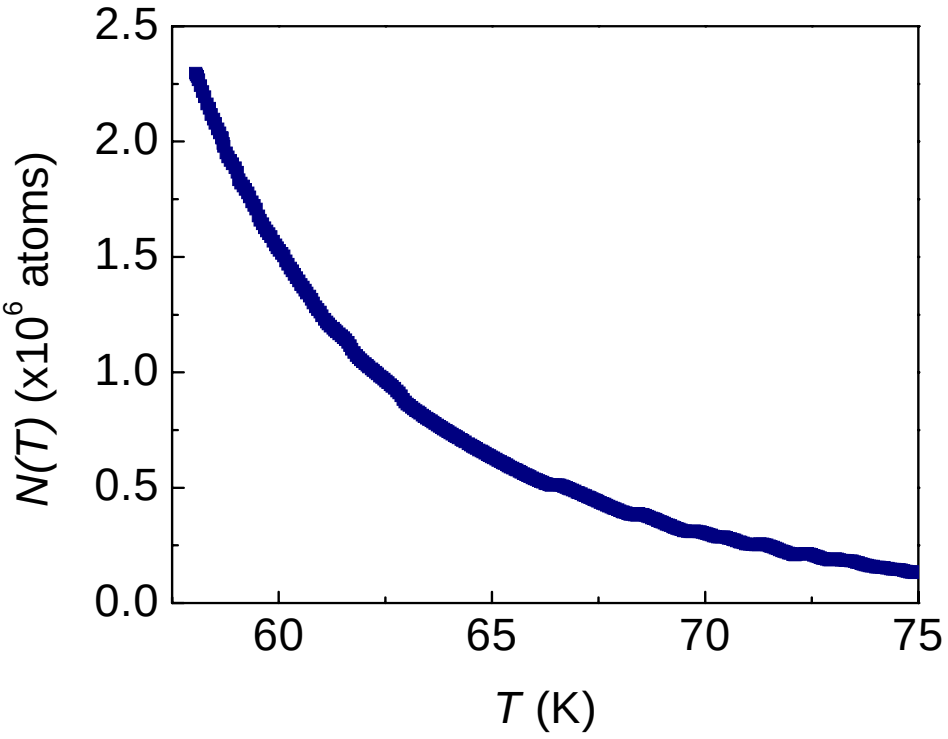

Figure 4.17. Adsorption spectrum of xenon atoms on NEMS surface. The adsorption spectrum is deduced from $N(T) = -m_{Xe}(f_G(T) - f_{NG}(T)/(\Re/2\pi)$, $\Re/2\pi = 0.99$ Hz/zg is the mass responsivity of the device. $f_G(T)$ and $f_{NG}(T)$ denote the resonant frequency data with applied gaseous flux and no flux, respectively.

Figure 4.18 shows the representative data of the spectral density of fractional frequency noise at T= 58 K with and without gaseous flux. The spectrum with no applied flux exhibits flicker noise from 0.1 Hz to 2 Hz and flattens out above 2 Hz, reflecting the instrumentation noise of FM PLL. In contrast, the spectrum with applied flux clearly shows excess noise contribution from gas. We have of course tested that the parameters affecting the loop gain of FM PLL (in particular, the quality factor of the resonator) do not change with temperature or coverage, and therefore cannot be responsible for the excess noise. More quantitatively, we calculate the fractional frequency noise contributed from gas, $S_y^G(\omega)$, by subtracting the spectral density of fractional frequency noise with zero flux, $S_y^{NG}(\omega)$, from that with applied flux at given temperatures $S_y^{Total}(\omega)$, i.e., from the formula $S_y^G(\omega) = S_y^{Total}(\omega) - S_y^{NG}(\omega)$. All the resulting spectra, as shown in figure 4.19, exhibit predicted functional form from equation (3.53), i.e.,

$$S_y(\omega) = \frac{aN(T)}{4\pi}\left(\frac{m_{Xe}}{M_{eff}}\right)^2 \int_0^\infty \frac{\cos\omega\tau}{(1+\tau/\tau_D)^{1/2}}\, d\tau . \qquad (4.18)$$

These spectral data are fitted to extract the diffusion time τ_D, using equation (4.18). Because the extracted diffusion times, ranging from 0.114 sec to 0.053 sec, are much shorter than the typical correlation times of an adsorption-desorption cycle,[16] the observed noise spectra cannot be attributed to adsorption-desorption process.

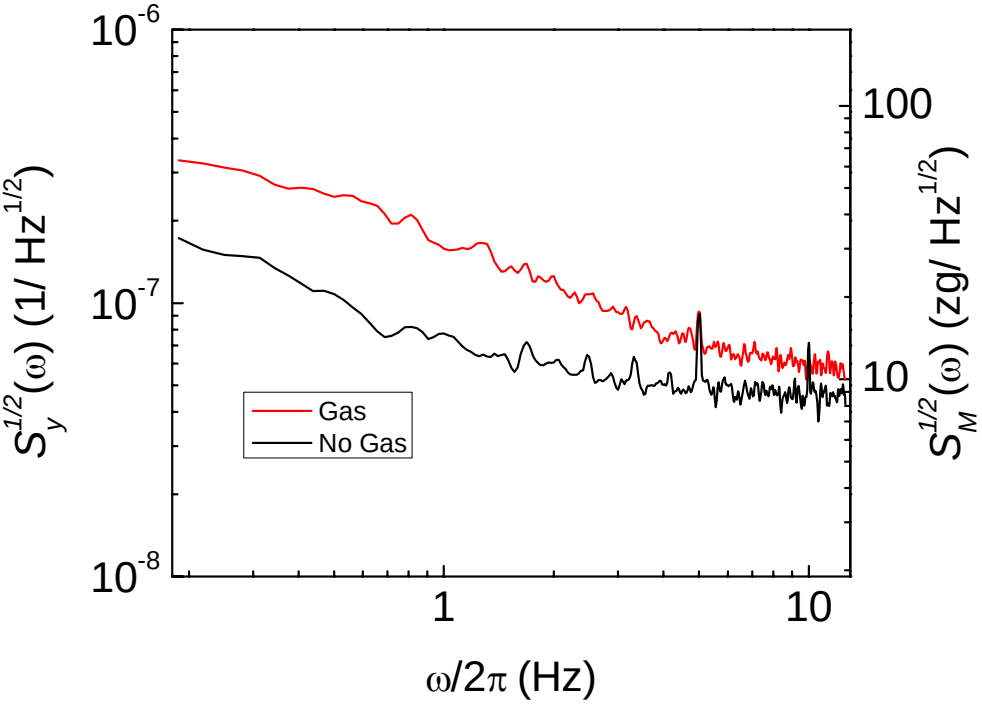

Figure 4.18. Representative fractional frequency noise spectra. The spectral density of fractional frequency with and without gaseous flux at T=59.2 K is shown. The spectrum, $S_y^{NG}(\omega)$, with no applied flux (black) reflects the instrumentation noise of FM PLL. In contrast, the spectrum $S_y^{Total}(\omega)$ with applied flux (red) clearly shows excess noise contribution from gas. The right hand axis shows the scale of the corresponding mass fluctuations in unit of zg/Hz$^{1/2}$.

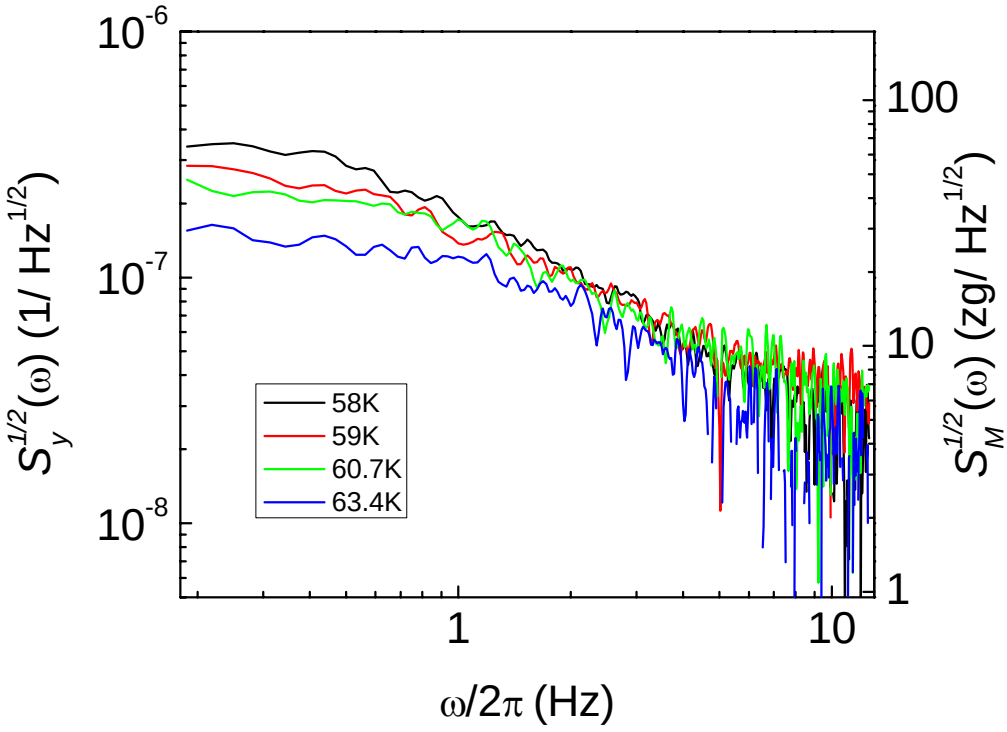

Figure 4.19. Spectral density of fractional frequency noise contributed from gas. The spectral density of fractional frequency noise contributed from the gaseous flux at four measurement temperatures is displayed. We calculate the fractional frequency noise contributed from gas, $S_y^G(\omega)$, by subtracting the spectral density of fractional frequency noise with zero flux, $S_y^{NG}(\omega)$, from that with applied flux at given temperatures $S_y^{Total}(\omega)$, i.e., from the formula $S_y^G(\omega) = S_y^{Total}(\omega) - S_y^{NG}(\omega)$. The right hand axis shows the scale of the corresponding mass fluctuations in unit of zg/Hz$^{1/2}$.

From the diffusion noise theory, we can also calculate the diffusion coefficients D by $D = L^2/(2a^2\tau_D)$, where a=4.43 is a numerical factor, and L=2.3 μm is the device length, (see section 3.5). Table 4.3 lists the extracted diffusion times and diffusion coefficients together with the corresponding coverage at four measurement temperatures. In general, the surface diffusion of xenon is determined by the corrugation of the adsorbate-surface potential and the attractive interactions between the adsorbed atoms.[13] At very dilute limits, the xenon atoms behave and diffuse like an ideal two-dimensional gas.[10,12] At higher coverage, however, the diffusion is more dominated by the attractive interaction between the adsorbed xenon atoms and as a result, the diffusion coefficient dramatically decreases with increasing coverage.[13] Our extracted diffusion coefficients are very close to D=2x10^{-8} cm^2/s, reported by Meixner and George for xenon on Pt(111) for coverage $\theta = 5\text{x}10^{14}$ atoms/cm^2 in spite of very different surface conditions and measurement temperatures.[13] The indifference of the diffusion coefficients to surface conditions and temperatures suggests that in both cases the attractive interaction between adsorbed xenon atoms completely dominates the surface diffusion.

Figure 4.21 shows the measured Allan deviation $\sigma_A(\tau_A)$ versus temperature with and without the gaseous flux for averaging time τ_A= 1 sec. The Allan deviation with zero applied flux, denoted by σ_A^{NG}, reflects the instrumentation noise floor of the FM PLL and slightly decreases with temperature. We attribute this slight decreasing trend with temperature to the corresponding increase in quality factor (15%) from T=75 K to T=58 K. In contrast, for temperature below 65 K, the Allan deviation with gaseous flux, σ_A^{Total}, clearly exceeds the instrumentation noise floor due to the excess noise contribution from the gas. Figure 4.22 shows the Allan deviation contributed from gas, σ_A^G, calculated by

subtracting the Allan deviation without gas from Allan deviation with gas, i.e., from the formula $(\sigma_A^G)^2 = (\sigma_A^{Total})^2 - (\sigma_A^{NG})^2$.

From equation (3.58), the expression for Allan deviation from diffusion noise theory is

$$\sigma_A^2(\tau_A) = \int_0^\infty \frac{8}{(\omega\tau_A)^2} S_y(\omega)\sin^4(\omega\tau_A/2)d\omega = \frac{2aN(T)}{\pi}\left(\frac{m_{Xe}}{M_{eff}}\right)^2 X(\frac{\tau_D}{\tau_A}), \qquad (4.19)$$

where $X(\tau_D/\tau_A)$ is a function defined in equation (3.59). Equation (4.19) shows that Allan deviation associated with the number fluctuation of an ensemble of adsorbed atoms is proportional to the square root of its total number, $N(T)$. Roughly speaking, we can thus attribute the monotonically increasing trend in Allan deviation in figure 4.22, as temperature is lowered, to the corresponding increase in the number of adsorbed xenon atoms in figure 4.17. Using equation (4.19) and measured $N(T)$ and τ_D from table 4.3, we calculate the Allan deviation and display the result in figure 4.22. In figure 4.22, we also show the calculated Allan deviation, $\sigma_A(\tau_A) = \sqrt{N_a}\sigma_{OCC}(m_{Xe}/M_{eff})\sqrt{\tau_A/6\tau_r}$, from Yong and Vig's model for the case of immobile monolayer adsorption, assuming the monolayer coverage N_a = 2.3x10^6 at T=58 K and the sticking coefficient s=1 to estimate the correlation time for an adsorption-desorption cycle from $\tau_r = N(T)/(\Phi s A_D)$ and the variance of occupational probability from $\sigma_{OCC}^2 = N(N_a - N)/N_a^2$ (see section 3.4).[17,18] As shown in figure 4.22, the experimentally observed Allan deviation is consistent with the prediction from diffusion noise theory. In contrast, the estimated Allan deviation from Yong and Vig's model, vanishing at completion of one monolayer, is apparently contradictory to experimental observation.

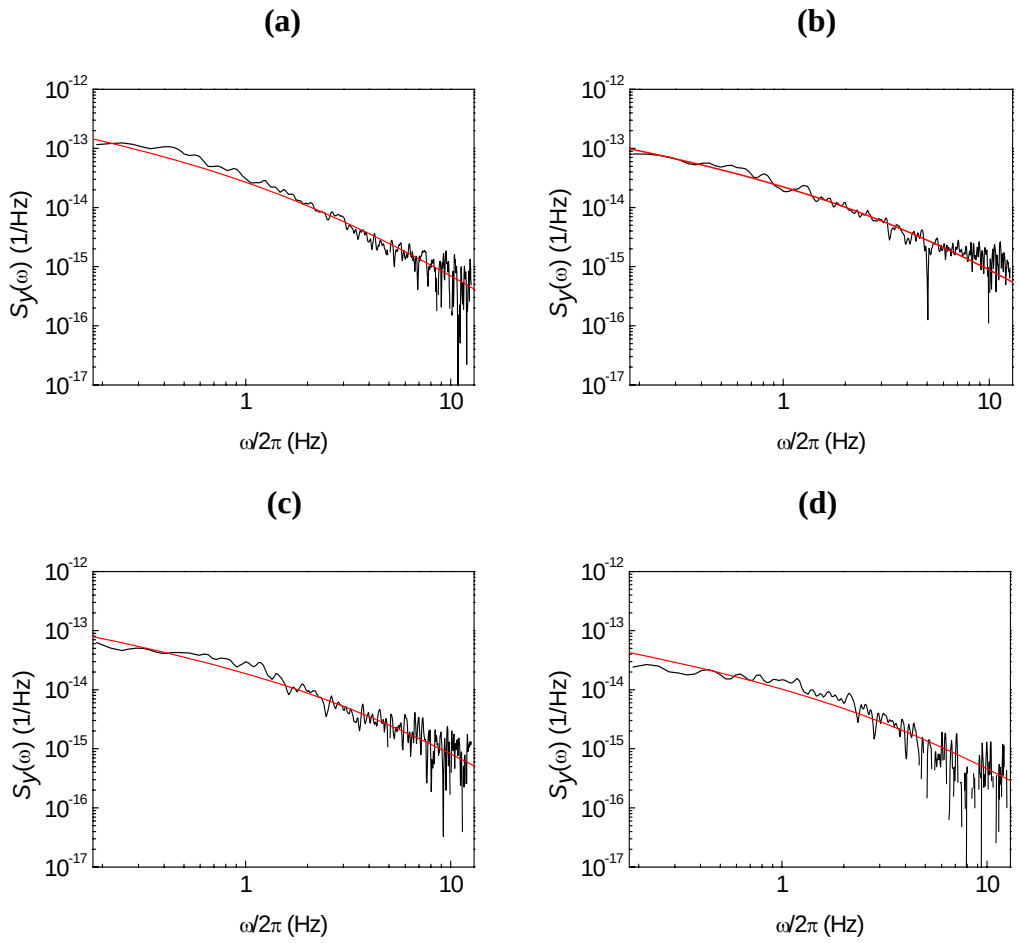

Figure 4.20. Spectral density of fractional frequency noise with fitting. Data (black) from figure 4.19 are fitted by a predicted function form in equation (4.18) (red) from diffusion noise theory to extract the diffusion times. **(a) Spectral density data with fitting at *T*= 58 K. (b) Spectral density data with fitting at *T*=59.2 K. (c) Spectral density data with fitting at *T*=60.7 K. (d) Spectral density data with fitting at *T*=63.4 K.**

Temp	N	θ	τ_D	D
K	atom	atom/cm^2	sec	cm^2/sec
58	2.30×10^{6}	6.67×10^{14}	0.114	1.15×10^{-8}
59.2	1.79×10^{6}	5.19×10^{14}	0.0637	2.06×10^{-8}
60.7	1.33×10^{6}	3.86×10^{14}	0.0553	2.37×10^{-8}
63.4	8.08×10^{5}	2.34×10^{14}	0.0530	2.47×10^{-8}

Table 4.3. Summary of diffusion times and coefficients versus temperature

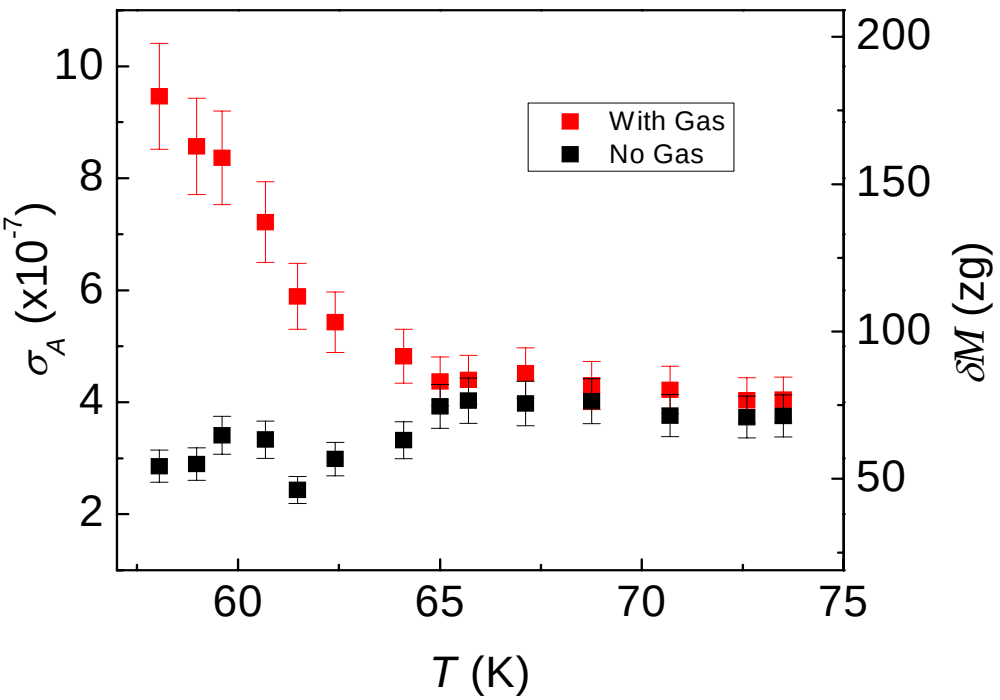

Figure 4.21. Allan deviation data with gas and without gas. The Allan deviation (black) with zero applied flux reflects the instrumentation noise floor of the FM PLL. For temperature below 65 K, the Allan deviation (red) with gas clearly exceeds that without gas due to the excess noise contribution from the gas. The right-hand axis shows the scale of the corresponding mass fluctuation in units of zg.

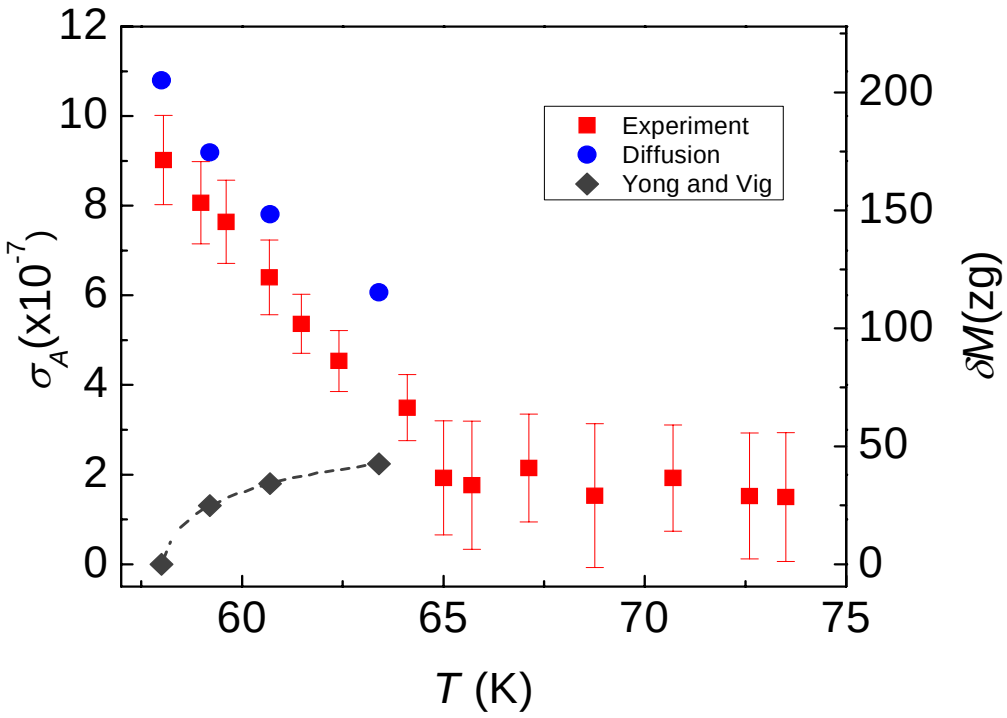

Figure 4.22. Comparison with prediction from diffusion noise theory and Yong and Vig's model. The Allan deviation (red) contributed from gas, σ_A^G, is calculated by subtracting the Allan deviation without gas from Allan deviation with gas, i.e., from the formula $(\sigma_A^G)^2 = (\sigma_A^{Total})^2 - (\sigma_A^{NG})^2$. The Allan deviation (blue) from diffusion noise is calculated using equation (4.19) and measured $N(T)$ and τ_D from table 4.3. For comparison, the calculated Allan deviation (dark gray) from Yong and Vig's model is also displayed, assuming the monolayer coverage N_a = 2.3x10^6 at T=58 K and the sticking coefficient s=1. The right hand axis shows the scale of the corresponding mass fluctuation in units of zg.

As already mentioned, no appreciable change in quality factor is observed from the adsorbed species in our experiment and thus the observed diffusion noise is non-dissipassive in nature, a very important attribute of parametric noise as pointed out by Cleland and Roukes.[17]

Having verified that the observed fluctuations are due to the mass fluctuation caused by diffusion, we can relate the spectral density of mass fluctuation $S_M^{1/2}(\omega)$ to the spectral density of fractional frequency noise $S_y^{1/2}(\omega)$ by the expression $S_M^{1/2}(\omega) = f_0 S_y^{1/2}(\omega)/(\Re/2\pi)$ with the mass responsivity. Similarly, we relate the Allan deviation to the corresponding mass fluctuation δM by $\delta M = f_0 \sigma_A /(\Re/2\pi)$. The scale in the right hand axes in figure 4.18, 4.19, 4.21 and 4.22 shows that the corresponding mass fluctuation is on the order of tens of zeptogram (1 zeptogram = 10^{-21} gram) and thus our experiment is indeed the "fluctuation sensing" at zeptogram scale.

4.7 Conclusion

In this chapter, we present the experimental measurement of phase noise of NEMS. We first analyze control servo behavior of a phase-locked loop based on NEMS and give the expressions for the locked condition and measurement bandwidth. Based on such a scheme, we then present in detail several electronic implementations, all of which are designed to lock minute mechanical resonance of NEMS and complement each other in their merits. The homodyne phase-locked loop based on a two-port NEMS device fully utilizes the intrinsic bandwidth provided by NEMS, and is very desirable for sensing applications requiring fast response time. It requires, however, laborious manual adjustments and is limited in the locking range. On the other hand, the FM PLL, touted

for its easy loop implementation and large locking range, suffers from the limited bandwidth due to the lock-in detection. In general, the observed Allan deviation $\sigma_A(\tau_A)$ is consistent with the estimated value from the expression $\sigma_A(\tau_A) = (1/Q)10^{-DR/20}$ with experimentally determined dynamic range *DR* and *Q*. We summarize the performance of all the phase-locked loops with their device parameters considered in this chapter in table 4.1.

We then consolidate the phase noise and Allan deviation data of all the phase-locked loops and compare them with the LO requirement of CSAC. While our current performance, limited by transducer amplifier noise, only partially meets the requirement, the projected phase noise and Allan deviation for 400 MHz NEMS based oscillators with Q=10^4 and Q=10^5, limited by thermomechanical noise, clearly show the potential for this application.

We further demonstrate the measurement of diffusion noise arising from adsorbed xenon atoms on the NEMS device. In general, our experimental results can be explained with the diffusion noise theory. The measured spectra of fractional frequency noise confirm the predicted functional form from the diffusion noise theory and the extracted diffusion coefficients agree well with the reported values in literature. Moreover, the measured Allan deviation contributed from gas is consistent with the theoretical estimates from diffusion noise theory, using the total number of adsorbed atoms and extracted diffusion times. Finally, we point out that the diffusion noise or its equivalent mass fluctuation, measured with unprecedented mass sensitivity at zeptogram level, imposes the ultimate sensitivity limits of any nanoscale gas sensors, regardless of their sensing mechanisms. But more importantly, this work, for the first time, goes beyond simple

measurement of adsorption spectrum in nanodevices and demonstrate a canonical example where a high quality factor NEMS device, inserted into a phase-locked loop, serves to probe the noise process of the adsorbed species and extract the microscopic and dynamic information of surface diffusion. We expect the generalization of this approach will find many interesting applications in surface science of nanodevices.

References

1. H. Pauly and G. Scoles (editor) *Atomic and Molecular Beam Methods* (New York, Oxford University Press, 1988).

2. J. Krim, D. H. Solina, and R. Chiarello Nanotribology of a Kr Monolayer: a quartz-crystal microbalance study of atomic scale friction. *Phys. Rev. Lett*. **66**, 181-184 (1991).

3. T. R. Albrecht, P. Grutter, D. Horne, and D. Rugar Frequency modulation detection using high Q cantilever for enhanced force microscopy sensitivity. *J. Appl. Phys.* **69**, 668 (1991).

4. Y. T. Yang, K. L. Ekinci, X. M. H. Huang, M. L. Roukes, C. A. Zorman, and M. Mehregany Monocrystalline 3C-SiC nanoelectromechanical systems. *Appl. Phys. Lett.* **78**, 612 (2001).

5. J. Kitching Local oscillator requirements for chip-scale atomic clocks. *Private communication* (2004).

6. J. Kitching, S. Knappe, and L. Hollberg Miniatured vapor-cell atomic frequency. *Appl. Phys. Lett.* **81**, 553 (2002).

7. L. D. Landau and E. M. Lifshitz *Statistical Physics* Vol. 1 (Oxford, Butterworkth-Heinemann,1980).

8. E. L. Elson and D. Magde Fluoresence correlation spectroscopy I concept basis and theory. *Biopolymer* **13**, 1-27 (1974).

9. D. Magde, E. L. Elson, and W. W. Webb Thermodynamic fluctuations in a reacting system- Measurement by fluorescence correlation spectroscopy. *Phys. Rev. Lett.* **29**, 705-708 (1972).

10. C. T. Rettner, D. S. Bethune, and E. K. Schweizer Measurement of Xe desorption rates from Pt(111):Rates for an ideal surfaces and in the defect-dominated regime. *J. Chem. Phys.* **92**, 1442 (1990).

11. H. Clark *The theory of Adsorption and Catalysis* (London, Academic Press, 1970).

12. J. Ellis, A. P. Graham, and J. P. Toennies Quasielastic helium atom scattering from a two-dimensional gas of xenon atoms on Pt(111). *Phys. Rev. Lett.* **82**, 5072-5075 (1999).

13. D. L. Meixner and S. M. George Surface diffusion of xenon on Pt(111). *J. Chem. Phy.* **98**, 11 (1983).

14. H. J. Kreuzer and Z. W. Gortel *Physisorption Kinetics* (Heidelberg, Springer-Verlag, 1986)

15. K. L. Ekinci, Y. T. Yang, and M. L. Roukes Ultimate limits to inertial mass sensing based upon nanoelectromechanical systems. *J. Appl. Phys.* **95**, 2682 (2004).

16. To measure the correlation time of an adsorption desorption cycle, we dose the device with given coverage, block the gaseous flux with mechanical shutter, and observe the coverage over the time. Under similar conditions, the typical correlation time, obtained by fitting the exponential decay of the coverage, is >2 sec.

17. A. N. Cleland and M. L. Roukes Noise processes in nanomechanical resonators. *J. Appl. Phys.* **92**, 2758 (2002).

18. Y. K.Yong and J. Vig Resonator surface contamination: a cause of frequency fluctuations. *IEEE Trans. On Ultrasonics, Ferroelectric, and Frequency Control* **36**, 452 (1989).

Chapter 5

Zeptogram Scale Nanomechanical Mass Sensing

Very high frequency nanoelectromechanical systems (NEMS) provide unprecedented sensitivity for inertial mass sensing. We demonstrate *in situ* measurements in *real time* with mass noise floor ~20 zeptogram. Our best mass sensitivity corresponds to ~7 zeptograms, equivalent to ~30 Xenon atoms or the mass of an individual 4 kDa molecule. Detailed analysis of the ultimate sensitivity of such devices based on these experimental results indicates that NEMS can ultimately provide inertial mass sensing of individual intact, electrically neutral macromolecules with single-Dalton (1 amu) sensitivity.

5.1 Introduction

Today mechanically based sensors are ubiquitous, having a long history of important applications in many diverse fields of science and technology. Among the most responsive are sensors based on the acoustic vibratory modes of crystals,[1,2] thin films,[3] and more recently, microelectromechanical systems (MEMS)[4,5] and nanoelectromechancial systems (NEMS).[6,7] Two attributes of NEMS devices—minuscule mass and high quality factor (Q)— provide them with unprecedented potential for mass sensing. This is revealed in our analysis in chapter 3 and demonstrated by recently achieved femtogram[6] and attogram resolution.[7] Attainment of zeptogram (1 zg=10^{-21} g) sensitivity shown herein opens many new possibilities; among them is directly "weighing" the inertial mass of individual, electrically neutral macromolecules.[8] Such sensitivity also enables the observation of extremely minute (statistical) mass fluctuations that arise from the diffusion of atomic species upon the surfaces of NEMS devices—processes that impose fundamental sensitivity limits upon nanoscale gas sensors (see section 4.6). As an initial step into these applications, we perform mass sensing experiments with gaseous species adsorbed on the NEMS surfaces at the zeptogram scale.

5.2 Experimental Setup

All the experiments are done *in situ* within a cryogenically cooled, ultrahigh vacuum apparatus with base pressure below 10^{-10} Torr. As shown in figure 5.1, a minute, calibrated, highly controlled flux of Xe atoms or N_2 molecules is delivered to the device surface by a mechanically shuttered gas nozzle within the apparatus.[9] The nozzle has an

orifice with a 100 μm diameter aperture, which is maintained at T=200 K by heating it with ~1 W of power to prevent condensation of the gas within the orifice and its supply line. Gas is delivered to this nozzle from a buffering chamber (volume V_C =100 cm^3 for the N_2 experiments, and 126 cm^3 for the Xe experiments), in turn maintained at temperature T_C = 300 K. Prior to the commencement of a run, this chamber is pressurized with the species to be delivered, then sealed to allow escape only through the nozzle. Thereafter, the rate of pressure decrease, $\dot{P}_C$, which is continuously monitored, is proportional to the total adsorbate delivery rate from the gas nozzle to the NEMS sensor, i.e., the number of incident atoms or molecules per unit time. The total number flux of gas atoms or molecules out of the nozzle in steady state is given by $\dot{N}_C = \dot{P}_C V_C / k_B T_C$.

Real-time mass sensing is enabled by the incorporation of NEMS device into a VHF frequency modulation phase-locked loop (FM PLL), described in section 4.4. With this measurement scheme, data are obtained from two separate sets of experiments involving different NEMS resonators: a first device (hereafter, **D133**) with a fundamental resonant frequency f_0~133 MHz having dimensions: 2.3 μm (L) x 150 nm (w) x 70nm (t), and a second (hereafter, **D190**) with f_0~ 190 MHz and dimensions 2.3 μm (L) x 150 nm (w) x 100 nm (t). Both are patterned from SiC epilayers[10] and exhibit a quality factor of Q =5000 in the temperature range of the present measurement.

For our experiment, the NEMS devices are maintained at high vacuum (~10^{-7} torr) at 300K for >1 day prior to mass accretion studies. The experiments are carried out immediately after cryogenically cooling the devices in a background pressure below ~10^{-10} torr. Hence we assume the arriving species adsorb with unity sticking probability;

for our choices of Xe and N_2 this is a reasonable assumption.[11] The mass deposition rate to the device is then

$$\dot{M}_D = m\dot{N}_D = mA_D\,\dot{N}_C/(\pi L_D^{\,2}), \tag{5.1}$$

where m is the mass of adsorbed species (m_{Xe}=131 amu, m_{N_2}=28 amu), the factor A_D/L^2 is the solid angle of capture, A_D is the surface area of the device exposed to the flux, and L_D is the distance between the device and nozzle.[9] The weighting factor $1/\pi$ accounts for the cosine distribution of the beam profile. For N_2 experiment, $\dot{N}_C$ = 2.25 x 10^{12} molecules/sec, L_D = 2.37 cm, and A_D = 3.45 x 10^{-13} m^2, yielding $\dot{M}_D$=20.5 zg/sec. For the Xe experiment, the setting are $\dot{N}_C$ = 2.81 x 10^{12} atoms/sec, L_D=1.86 cm, and A_D=3.45x10^{-13} m^2. These values yield $\dot{M}_D$ = 195 zg/sec.

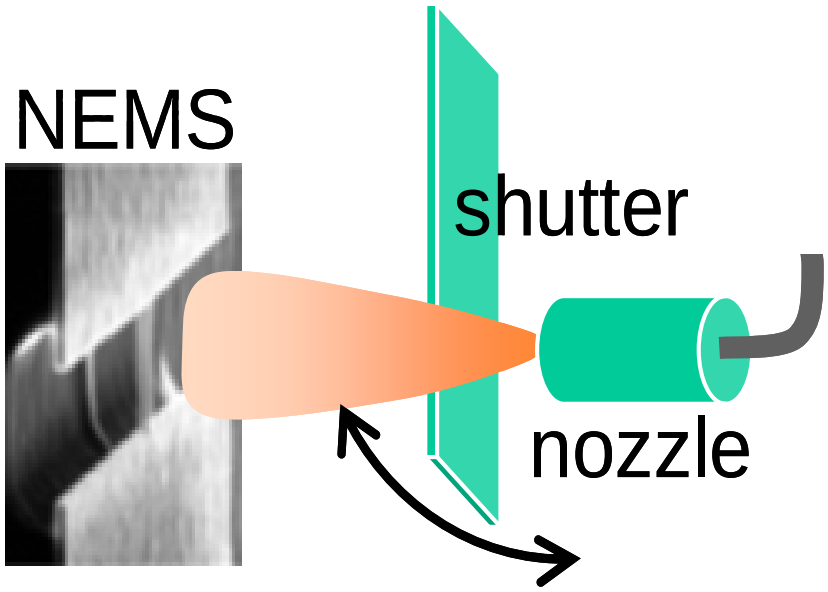

Figure 5.1. Experimental configuration. A gas nozzle with a 100 μm aperture provides a controlled flux of atoms or molecules. The flux is gated by a mechanical shutter to provide calibrated, pulsed mass accretions upon the NEMS device. The mass flux is determined by direct measurements of the gas flow rate, in conjunction with effusive-source formulas for the molecular beam emanating from the nozzle.

5.3 Mass Sensing at Zeptogram Scale

We first demonstrate the *real time*, *in situ*, zeptogram-scale mass accretion on **D190**, resulting from pulsed delivery of N_2 molecules at T=37 K, as shown in figure 5.2. With a mass deposition rate $\dot{M}_D$ = 20.5 zg/sec, sequential openings of the shutter for 5 second intervals provides a series of 100 zg accretions. The resulting discretely stepped frequency shifts tracked by the FM PLL confirm sequential, regular steps of mass accretion (each ~100 zg, i.e., ~2000 N_2 molecules).[12] The mass sensitivity δM is set by the standard deviation of frequency fluctuations on the plateaus

$$\delta M = \delta f / \Re = \left\langle (f - f_0)^2 \right\rangle^{1/2} / \Re . \qquad (5.2)$$

Here $\Re = \left| \partial f_0 / \partial M_{eff} \right|$ is the mass responsivity of the device; M_{eff} and f_0 are the effective vibratory mass and resonant frequency of the device, respectively. The data of figure 5.2 demonstrate δM =20 zg for the 1 sec averaging time employed.

The mass responsivities for the devices are directly determined from such pulsed atom or molecule deposition measurements. Data are shown both for **D190** (for conditions described above) and for **D133** in figure 5.3. We expose **D133** to Xe with mass deposition rate $\dot{M}_D$=195 zg/sec and opening shutter for 1 sec yields ~200 zg mass accretion (or equivalently ~900 Xe atoms) per data point at T =46 K. Both devices demonstrate unprecedented responsivities: $\Re$, directly extracted from the slope of the linear fit, at the level of roughly 1 Hz shift per zeptogram of accreted mass. More precisely, we find $\Re_{D133} \approx 0.96$ Hz/zg and $\Re_{D190} \approx 1.16$ Hz/zg. These values are in excellent agreement with the theoretical estimates from the expression $\Re \approx f_0 / 2M_{eff}$,

which yields ~0.89 Hz/zg for **D133** (M_{eff} ≈73 fg) and ~0.99 Hz/zg for **D190** (M_{eff} ≈96 fg).[8]

Our highest mass sensitivity, at present, is demonstrated with **D133** stabilized at T= 4.2 K. Exceptionally small fractional frequency fluctuations $\delta f / f_0 = \left\langle (f - f_0)^2 \right\rangle^{1/2} =$ 5×10^{-8} (50 ppb) are observed over a course of ~4000 sec interval with 1 sec averaging time (right inset of figure 5.3). This demonstrates attainment of a mass sensitivity of δM ~7 zg, equivalent to accretion of ~30 Xe atoms or, alternatively, of an *individual* 4 kDa macromolecule. Using M_{eff} ≈73 fg, Q~5000, and dynamic range DR ~80 dB, such a mass sensitivity is consistent with the estimated value 2.9 zg from the expression,

$$\delta M \sim (2M_{eff} / Q)10^{-DR/20}, \tag{5.3}$$

as described by Ekinci et al.[7] Our current dynamic range is determined, at the bottom end, by the noise floor of the posttransducer readout amplifier of the NEMS device and, at the top end, by the onset of nonlinearity arising from the Duffing instability for a doubly clamped beam (see section 3.2). With our current experimental setup, we are able to track mass accretions up to a total of ~2.3x10^6 Xe atoms on **D190**, with no observable change in the quality factor (see section 4.6). This confirms a remarkably large mass dynamic range from a few kDa (or several zeptogram sensitivity) up to ~100 MDa range, corresponding to almost femtogram-scale accretions.

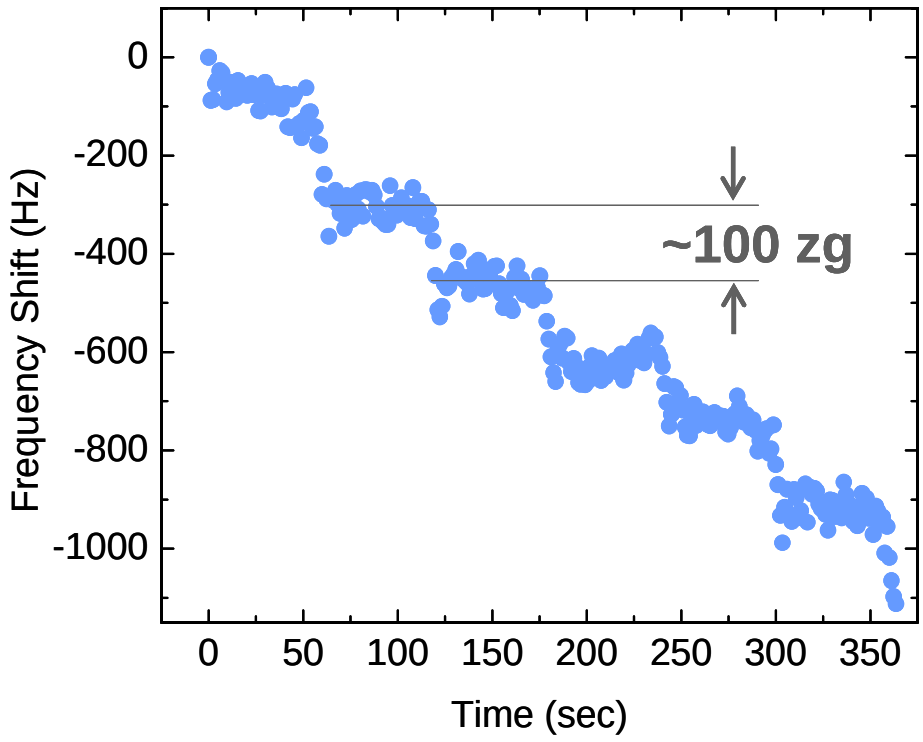

Figure 5.2. Real time zeptogram-scale mass-sensing experiment. Sequential mass depositions are executed *in situ* upon the 190 MHz device within a cryogenic UHV apparatus. The resulting frequency shift of the NEMS device is tracked in *real time* by a very high frequency (VHF) phase-locked loop. Each step in the data corresponds to a ~100 zg mass accretion (~2000 N_2 molecules) resulting from opening the mechanical shutter for 5 sec. The root-mean-square frequency fluctuations of the system correspond to a mass sensitivity of δM = 20 zg for the 1 sec averaging time employed.

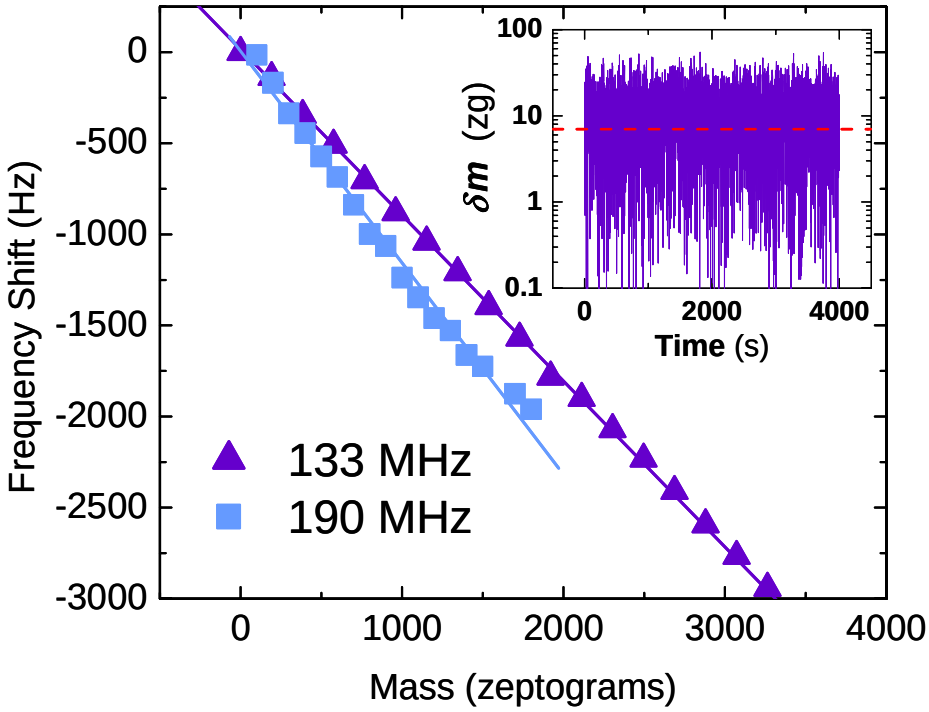

Figure 5.3. Mass responsivities of nanomechanical devices. The mass responsivities (resonant frequency shifts versus accreted mass) are measured for two VHF NEMS devices (operating at 133 MHz and 190 MHz). Xe atoms are accreted at T=46 K upon the 133 MHz device with ~200 zg mass increments per data point (purple). N_2 molecules are accreted at T=37 K upon the 190 MHz device with ~100 zg mass increments per data point (blue). The slopes of the mass loading curves directly exhibit the unprecedented mass responsivity on the order 1 Hz per zeptogram. **(right inset) Mass sensitivity.** The "mass noise floor" for the 133 MHz device, which originates from its frequency-fluctuation noise, is measured with 1 sec averaging time over the course of ~4000 sec while it is temperature stabilized at 4.2 K with zero applied flux. The average root-mean-square value (red dashed line), reflects the attainment of ~7 zg (i.e., ~4 kDa) mass sensitivity, the equivalent of ~30 Xe atoms.

5.4 Conclusion

We demonstrate NEMS mass sensing at the zeptogram scale. The agreement between predicted and experimentally observed values for both $\Re$ and δM confirms our analyses in chapter 3 and validates their use in projecting a path toward single-Dalton mass sensitivity.[8] Attainment of this goal is possible, for example, with a device having a fundamental resonant frequency of 1 GHz, vibratory mass of M_{eff}=1x10^{-16} g, and Q=10,000, using a transduction-readout system providing DR=80 dB. These are realistic parameters for next generation NEMS.[13] Huang, et al. recently attained NEMS vibrating in fundamental mode at microwave frequencies.[13] In conjunction with the recent development of techniques for improved Q,[14] and the advances in frequency-shift readout in the tens of ppb range, it is clear that NEMS sensing at the level of ~1 Da will soon be within reach. Attainment of NEMS mass sensors with single-Dalton sensitivity will make feasible the detection of *individual*, intact, electrically neutral macromolecules with masses ranging well into the hundreds of MDa range. This is an exciting prospect — when realized it will blur the traditional distinction between inertial mass sensing and mass spectrometry. We anticipate that it will also open intriguing possibilities in atomic physics and life science.[15,16]

References

1. D. S. Ballantine et al. *Acoustic Wave Sensors* (San Diego, Academic Press, 1997).

2 C. Lu *Application of Piezoelectric Quartz Crystal Microbalance* (London, Elsevier, 1984).

3. M. Thompson and D. C. Stone *Surface-Launched Acoustic Wave Sensors: Chemical Sensing and Thin Film Characterization* (New York, John Wiley and Sons, 1997).

4. J. Thundat, E. A. Wachter, S. L. Sharp, and R. J. Warmack Detection of mercury vapor using resonating microcantilevers. *Appl. Phys. Lett.* **66**, 1695–1697 (1995).

5. Z. J. Davis, G. Abadal, O. Kuhn, O. Hansen, F. Grey, and A. Boisen Fabrication and characterization of nanoresonating devices for mass detection. *J. Vac. Sci. Technol.* **B 18**, 612-616 (2000).

6. N. V. Lavrik and P. G. Datskos Femtogram mass detection using photothermally actuated nanomechanical resonators. *Appl. Phys. Lett* **82**, 2697 (2003).

7. K. L. Ekinci, X. M. H. Huang, and M. L. Roukes Ultrasensitive nanoelectromechanical mass sensing. *Appl. Phy. Lett.* **84**, 4469 (2004).

8. K. L. Ekinci, Y. T. Yang, and M. L. Roukes Ultimate limits to inertial mass detection based upon nanoelectromechanical systems. *J. Appl. Phys.* **95**, 2682 (2004).

9. H. Pauly and G. Scoles (editor) *Atomic and Molecular Beam Methods* (New York, Oxford University Press, 1988).

10. Y. T. Yang et al. Monocrystalline silicon carbide nanoelectromechancial systems. *Appl. Phys. Lett.* **78**, 162-164 (2001).

11. H. J. Kreuzer and Z. W. Gortel *Physisorption Kinetics* (Springer-Verlag, New York, 1986). At low coverage, unity sticking probability are observed for Xe on W(100) at T= 65 K. Xe on Ni(100) at T=30 K and N_2 on Ni(110) T=87 K. We expect the above to be representative materials and conditions, so that cryogenic adsorption upon the NEMS device will behave similarly in our case.

12. We have also verified that the arriving species provide negligible thermal perturbation upon the device. This is accomplished by high-resolution *in situ* resistance thermometry upon the metallic displacement-transducer electrode, and comparing shutter-open and shutter-closed conditions. The kinetic energy of the arriving species negligibly perturbs the device.

13. X. M. H. Huang, C. A. Zorman, M. Mehregany, and M. L. Roukes Nanodevices motion at microwave frequencies. *Nature* **421**, 496 (2003).

14. X. M. H. Huang, X. L. Feng, C. A. Zorman, M. Mehregany, and M. L. Roukes Free free beam silicon carbide nanomechanical resonators. *New J. Phys.* **7**, 247 (2005).

15. W. Hansel, P. Hommelhoff, T. W. Hansh, and J. Reichel Bose-Einstein condensation on microelectronic chips. *Nature* **413**, 498-500 (2001).

16. R. Aebersold and M. Mann Mass spectrometry-based proteomics. *Nature* **422**, 198-207 (2003).

Chapter 6*

Monocrystalline Silicon Carbide Nanoelectromechanical Systems

SiC is an extremely promising material for nanoelectromechanical systems given its large Young's modulus and robust surface properties. We have patterned nanometer scale electromechanical resonators from single-crystal 3C-SiC layers grown epitaxially upon Si substrates. A surface nanomachining process is described that involves electron beam lithography followed by dry anisotropic and selective electron cyclotron resonance plasma etching steps. Measurements on a representative family of the resulting devices demonstrate that, for a given geometry, nanometer-scale SiC resonators are capable of yielding substantially higher frequencies than GaAs and Si resonators.

© *2001 American Institute of Physics.* [DOI: 10.1063/1.1338959]

* This section has been published as: Y. T. Yang, K. L. Ekinci, X. M. H. Huang, L. M. Schiavone, M. L. Roukes, C. A. Zorman, and M. Mehregany, *Appl. Phys. Lett.* **78**, 162-164 (2001).

6.1 Introduction

Silicon carbide is an important semiconductor for high temperature electronics due to its large band gap, high breakdown field, and high thermal conductivity. Its excellent mechanical and chemical properties have also made this material a natural candidate for microsensor and microactuator applications in microelectromechanical systems (MEMS).[1,2]

Recently, there has been a great deal of interest in the fabrication and measurement of semiconductor devices with fundamental mechanical resonance frequencies reaching into the microwave bands.[3] Among technological applications envisioned for these nanoelectromechanical systems (NEMS) are ultrafast, high-resolution actuators and sensors, and high frequency signal processing components and systems. From the point of view of fundamental science, NEMS also offer intriguing potential for accessing regimes of quantum phenomena and for sensing at the quantum limit.[4]

SiC is an excellent material for high frequency NEMS for two important reasons. First, the ratio of its Young's modulus, E, to mass density, ρ, is significantly higher than for other semiconducting materials commonly used for electromechanical devices, e.g., Si and GaAs. Flexural mechanical resonance frequencies for beams directly depend upon the ratio $\sqrt{E/\rho}$. The goal of attaining extremely high fundamental resonance frequencies in NEMS, while simultaneously preserving small force constants necessary for high sensitivity, requires pushing against the ultimate resolution limits of lithography and nanofabrication processes. SiC, given its larger $\sqrt{E/\rho}$, yields devices that operate at significantly higher frequencies for a given geometry, than otherwise possible using

conventional materials. Second, SiC possesses excellent chemical stability.[3] This makes surface treatments an option for higher quality factors (Q factor) of resonance. It has been argued that for NEMS the Q factor is governed by surface defects and depends on the device surface-to-volume ratio.[2]

Micron-scale SiC MEMS structures have been fabricated using both bulk and surface micromachining techniques. Bulk micromachined 3C-SiC diaphragms, cantilever beams, and torsional structures have been fabricated directly on Si substrates using a combination of 3C-SiC growth processes and conventional Si bulk micromachining techniques in aqueous KOH and TMAH solutions.[5,6] Surface micromachined SiC devices have primarily been fabricated from polycrystalline 3C-SiC (poly-SiC) thin films deposited directly onto silicon dioxide sacrificial layers, patterned using reactive ion etching, and released by timed etching in aqueous hydrofluoric acid solutions.[8] Single crystal 3C-SiC surface micromachined structures have been fabricated in a similar way from 3C-SiC-on-SiO_2 substrates created using wafer bonding techniques.[9] We have developed an alternative approach for nanometer-scale single crystal, 3C-SiC layers that is not based upon wet chemical etching or wafer bonding. Especially noteworthy is that our final suspension step in the surface nanomachining process is performed by using a dry etch process. This avoids potential damage due to surface tension encountered in wet etch processes, and circumvents the need for critical point drying when defining large, mechanically compliant devices. We first describe the method we developed for fabrication of suspended SiC structures, then demonstrate the high frequency performance attained from doubly clamped beams read out using magnetomotive detection.

6.2 Device Fabrication and Measurement Results

The starting material for device fabrication is a 259 nm thick single crystalline 3C-SiC film heteroepitaxially grown on a 100 mm diameter (100) Si wafer. 3C-SiC epitaxy is performed in a rf induction-heated reactor using a two-step, carbonization-based atmospheric pressure chemical vapor deposition (APCVD) process detailed elsewhere.[10] Silane and propane are used as process gases and hydrogen is used as the carrier gas. Epitaxial growth is performed at a susceptor temperature of about 1330 $^{\circ}$C. 3C-SiC films grown using this process have a uniform (100) orientation across each wafer, as indicated by x-ray diffraction. Transmission electron microscopy and selective area diffraction analysis indicates that the films are single crystalline. The microstructure is typical of epitaxial 3C-SiC films grown on Si substrates, with the largest density of defects found near the SiC/Si interface, which decreases with increasing film thickness. A unique property of these films is that the 3C-SiC/Si interface is absent of voids, a characteristic not commonly reported for 3C-SiC films grown by APCVD.

Fabrication begins by defining large area contact pads by optical lithography. A 60 nm thick layer of Cr is then evaporated and, subsequently, standard lift-off is carried out with acetone. Samples are then coated with a bilayer polymethylmethacrylate (PMMA) resist prior to patterning by electron beam lithography. After resist exposure and development, 30–60 nm of Cr is evaporated on the samples, followed by lift-off in acetone. The pattern in the Cr metal mask is then transferred to the 3C-SiC beneath it by anisotropic electron cyclotron resonance (ECR) plasma etching. We use a plasma of NF_3, O_2, and Ar at a pressure of 3 mTorr with respective flow rates of 10, 5, 10 sccm, and a

microwave power of 300 W. The acceleration dc bias is 250 V. The etch rate under these conditions is ~65 nm/min.

The vertically etched structures are then released by controlled local etching of the Si substrate using a selective isotropic ECR etch for Si. We use a plasma of NF_3 and Ar at a pressure of 3 mTorr, both flowing at 25 sccm, with a microwave power 300 W, and a dc bias of 100 V. We find that NF_3 and Ar alone do not etch SiC at a noticeable rate under these conditions. The horizontal and vertical etch rates of Si are ~300 nm/min. These consistent etch rates enable us to achieve a significant level of control of the undercut in the clamp area of the structures. The distance between the suspended structure and the substrate can be controlled to within 100 nm.

After the structures are suspended, the Cr etch mask is removed either by ECR etching in an Ar plasma or by a wet Cr photomask etchant (perchloric acid and ceric ammonium nitrate). The chemical stability and the mechanical robustness of the structures allow us to perform subsequent lithographic fabrication steps for the requisite metallization (for magnetomotive transduction) step on the *released* structures. Suspended samples are again coated with bilayer PMMA and after an alignment step, patterned by electron beam lithography to define the desired electrodes. The electrode structures are completed by thermal evaporation of 5 nm thick Cr and 40 nm thick Au films, followed by standard lift-off. Finally, another photolithography step, followed by evaporation of 5 nm Cr and 200 nm Au and conventional lift-off, is performed to define large contact pads for wire bonding. Two examples of completed structures, each containing a family of doubly clamped SiC beams of various aspect ratios, are shown in figure 6.1.

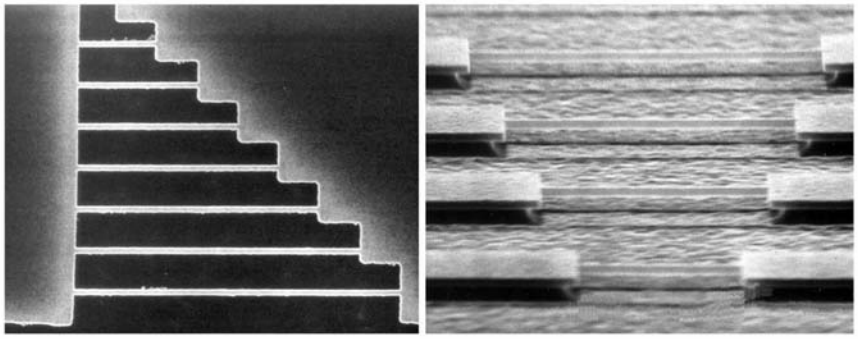

Figure 6.1. SEM picture of doubly clamped SiC beams. Doubly clamped SiC beams patterned from a 259 nm thick epilayer. (left) Top view of a family of 150 nm wide beams, having lengths from 2 to 8 μm. (right) Side view of a family of 600 nm wide beams, with lengths ranging from 8 to 17 μm.

We have measured the fundamental resonance frequencies of both the in-plane and out-of-plane vibrational modes for a family of doubly clamped SiC beams, with rectangular cross section and different aspect ratios (length/width). Samples were glued into a chip carrier and electrical connections were provided by Al wirebonds. Electromechanical characteristics were measured using the magnetomotive detection technique[11] from 4.2 to 295 K, in a superconducting solenoid within a variable temperature cryostat. The measured fundamental frequencies in this study ranged from 6.8 to 134 MHz. The quality factors, extracted from the fundamental mode resonances for each resonator, range from $10^3<Q<10^4$. Figure 6.2 shows the response of one representative beam with dimensions 8 μm (length) × 600 nm (width) × 259 nm (thickness). This particular device yields an in-plane resonant frequency of 71.91 MHz and a Q=4000 at 20 K. Quality factors at room temperature were typically a factor of 4–5 smaller than values obtained at low temperature.

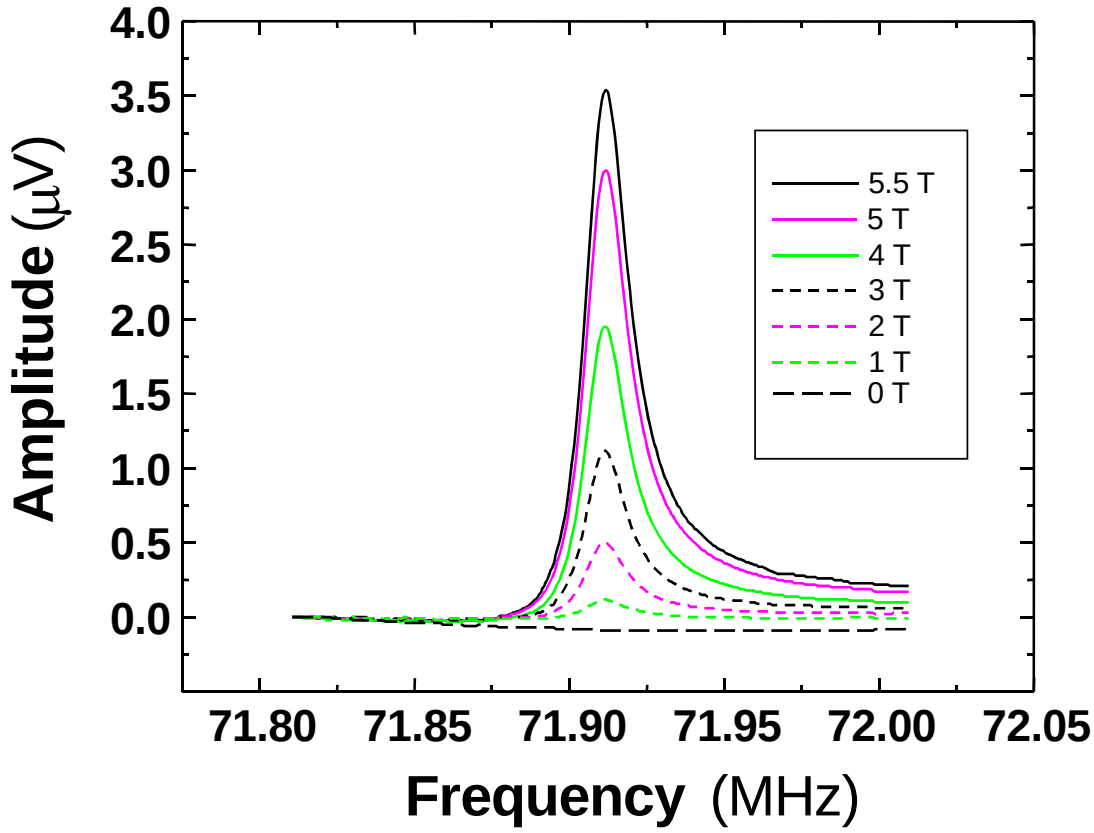

Figure 6.2. Representative data of mechanical resonance. A SiC doubly clamped beam resonating at 71.91 MHz, with quality factor Q=4000. The family of resonance curves are taken at various magnetic fields; the inset shows the characteristic B^2 dependence expected from magnetomotive detection. For clarity of presentation here the data are normalized to response at zero magnetic field, with the electrode's dc magnetoresistance shift subtracted from the data; these provide an approximate means for separating the electromechanical response from that of the passive measurement circuitry.

We now demonstrate the benefits of SiC for NEMS, by directly comparing frequencies attainable for structures of similar geometry made with SiC, Si, and GaAs. The fundamental resonance frequency, f_0, of a doubly clamped beam of length, L, and thickness, *t*, varies linearly with the geometric factor t/L^2 according to the simple relation

$$f_0 = 1.03\sqrt{\frac{E}{\rho}}\frac{t}{L^2}, \tag{6.1}$$

where E is the Young's modulus and ρ is the mass density. In our devices the resonant response is not so simple, as the added mass and stiffness of the metallic electrode modify the resonant frequency of the device. This effect becomes particularly significant as the beam size shrinks. To separate the primary dependence upon the structural material from secondary effects due to electrode loading and stiffness, we employ a simple model for the composite vibrating beam.[12] In general, for a beam comprised of two layers of different materials the resonance equation is modified to become

$$f_0 = \frac{\eta}{L^2}\left(\frac{E_1 I_1 + E_2 I_2}{\rho_1 A_1 + \rho_2 A_2}\right). \tag{6.2}$$

Here the indices 1 and 2 refer to the geometric and material properties of the structural and electrode layers, respectively. The constant η depends upon mode number and boundary conditions; for the fundamental mode of a doubly clamped beam η =3.57. Assuming the correction due to the electrode layer (layer 2) is small, we can define a correction factor *K*, to allow direct comparison with the expression for homogeneous beam

$$f_0 = \frac{\eta}{L^2}\left(\frac{E_1 I_{10}}{\rho_1 A_{10}}K\right)^{1/2}, \quad \text{where} \quad K = \frac{E_1 I_1 + E_2 I_2}{E_1 I_{10}}\frac{1}{1+\dfrac{\rho_2 A_2}{\rho_1 A_1}}. \tag{6.3}$$

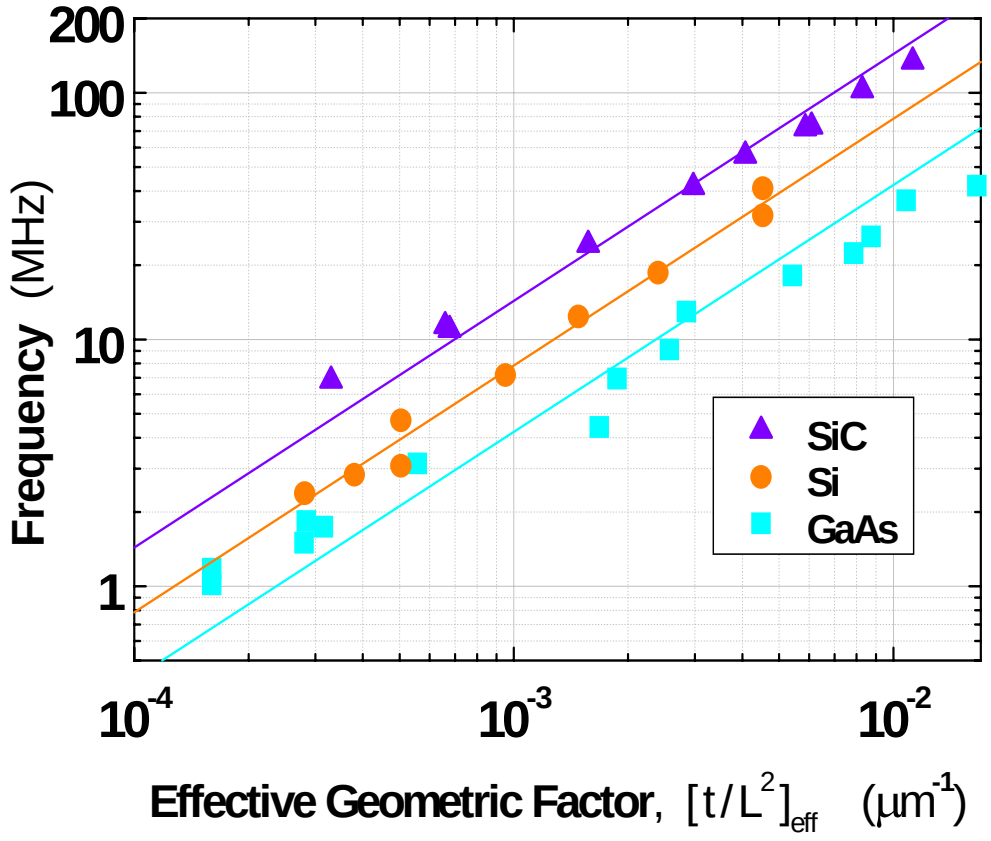

Figure 6.3. Frequency versus effective geometric factor for three families of doubly clamped beams made from single-crystal SiC, Si, and GaAs. All devices are patterned to have the long axis of the device along <100>. Ordinate are normalized to remove the effect of additional stiffness and mass loading from electrode metallization. The solid lines are least squares fits assuming unity slope, and yield values of the parameter $v = \sqrt{E/\rho}$ that closely match expected values.

In this expression, I_{10} is the moment calculated in the absence of the second layer. The correction factor K can then be used to obtain a value for the *effective geometric factor*, $[t/L^2]_{eff}$, for the measured frequency.[13] Further nonlinear correction terms, of order higher than $[t/L^2]_{eff}$, are expected to appear if the beams are under significant tensile or compressive stress. The linear trend of our data, however, indicates that internal stress corrections to the frequency are small.

In figure 6.3, we display the measured resonance frequencies as a function of $[t/L^2]_{eff}$ for beams made of three different materials: GaAs, Si and SiC.[14] The lines in this logarithmic plot represent least squares fits to the data assuming unity slope. From these we can deduce the effective values of the parameter, $v = \sqrt{E/\rho}$, which is similar (but not identical) to the velocity of sound for the three materials.[15] The numerical values obtained by this process are: $v(SiC) = 1.5\times10^4$ m/s, $v(Si) = 8.4\times10^3$ m/s, and $v(GaAs) = 4.4\times10^3$ m/s. These are quite close to values calculated from data found in the literature: $v(SiC) = 1.2\times10^4$ m/s,[16] $v(Si) = 7.5\times10^3$ m/s,[17] and $v(GaAs) = 4.0\times10^3$ m/s,[18] respectively. The small discrepancies are consistent with our uncertainties in determining both the exact device geometries and the precise perturbation of the mechanical response arising from the metallic electrodes. Nonetheless, SiC very clearly exhibits the highest $\sqrt{E/\rho}$ ratio.[17]

6.3 Conclusion

In conclusion, we report a simple method for fabricating nanomechanical devices from single-crystal 3C-SiC materials. We demonstrate patterning mechanical resonators using a single metal mask, and just two steps of ECR etching. Our results illustrate that

SiC is an ideal semiconductor with great promise for device applications requiring high frequency mechanical response.

References

1. M. Mehregany, C. A. Zorman, N. Rajan, and C. H. Wu Silicon carbide MEMS for harsh environments. *Proc. IEEE* **86**, 1594 (1998).

2. M. L. Roukes Nanoelectromechanical systems. *Technical Digest of the 2000 Solid-State Sensor and Actuator Workshop, Hilton Head Island, South Carolina (June 4–8 2000)* 367–376 (2000).

3. X. M. H. Huang, C. A. Zorman, M. Mehregany, and M. L. Roukes Nanodevices motion at microwave frequencies. *Nature* **421**, 496 (2003).

4. M. D. LaHaye, O. Buu, B. Camarota, and K. C. Schwab Approaching the quantum limit of a nanomechanical resonator. *Science* **304**, 74 (2004).

5. P. A. Ivanov and V. E. Chelnokov Recent developments in SiC single-crystal electronics. *Semicond. Sci. Technol.* **7**, 863 (1992).

6. L. U. Tong and M. Mehregany Mechanical-properties of 3C-Silicon Carbide. *Appl. Phys. Lett.* **60**, 2992 (1992).

7. C. Serre, A. Perez-Rodriguez, A. Romano-Rodriguez, J. R. Morante, J. Esteve, and M. C. Acero Test microstructures for measurement of SiC thin firm mechanical properties. *J. Micromech. Microeng.* **9**, 190 (1999).

8. A. J. Fleischman, X. Wei, C. A. Zorman, and M. Mehregany Surface micromachining of polycrystalline SiC deposited on SiO_2 by APCVD. *Proc. of the IEEE International Conference on Silicon Carbide, III-Nitrides, and Related Materials* (1997) 885–888 (1998).

9. S. Stefanescu, A. A. Yasseen, C. A. Zorman, and M. Mehregany Surface micromachined lateral resonant structures fabricated from single crystal 3C-SiC films, *Proceeding of the 10th International Conference on Solid State Sensors and Actuators, Sendai, Japan (June 7–10 1999)*, 194–198 (1999).

10. C. A. Zorman, A. J. Fleischman, A. S. Dewa, M. Mehregany, C. Jacob, S. Nishino, and P. Pirouz Epitaxial-growth of 3C-SiC films on 4 inch diam. (100) silicon-wafers by atmospheric-pressure chemical-vapor-deposition. *J. Appl. Phys.* **78**, 5136 (1995).

11. A. N. Cleland and M. L. Roukes Fabrication of high frequency nanometer scale mechanical resonators from bulk Si crystals. *Appl. Phys. Lett.* **69**, 2653 (1996).

12. K. E. Petersen and C. R. Guarnieri Young's modulus measurements of thin-films using micromechanics. *J. Appl. Phys.* **50**, 676 (1979).

13. The correction factor *K* primarily reflects mass loading from the metallic electrode. Using values from the literature for Young's modulus of the electrode materials we deduce that the additional stiffness introduced is completely negligible.

14. Electrodes were composed of either Au or Al, with typical thickness ranging from 50 to 80 nm.

15. The quantity $\sqrt{E_{<100>}/\rho}$ is strictly equal to neither the longitudinal sound velocity, $\sqrt{c_{11}/\rho}$, nor the transverse sound velocity, $\sqrt{c_{44}/\rho}$ for propagation along <100> direction of cubic crystal. Here the *c*s are elements of the elastic tensor and $E_{<100>} = (c_{11} - c_{12})(c_{11} + 2c_{12})/(c_{11} + c_{12})$ for cubic crystal. See, e.g. B. A. Auld, *Acoustic Fields and Waves in Solids*, 2nd edition (Robert E. Krieger, Malabar, 1990)

16. W. R. L. Lambrecht, B. Segall, M. Methfessel, and M. Vanschilfgaarde Calculated elastic-constants and deformation potentials of cubic SiC. *Phys. Rev. B* **44**, 3685 (1991).

17. J. J. Hall Electronic effects in elastic constants of n-Type silicon. *Phys. Rev.* **161**, 756 (1967).

18. R. I. Cottam and G. A. Saunders Elastic-constants of GaAs from 2 K to 320 K. *J. Phys. C: Solid State* **6**, 2105 (1973).

Chapter 7*

Balanced Electronic Detection of Displacement in Nanoelectromechanical Systems

We describe a broadband radio frequency balanced bridge technique for electronic detection of displacement in nanoelectromechanical systems (NEMS). With its two-port actuation-detection configuration, this approach generates a background-nulled electromotive force in a dc magnetic field that is proportional to the displacement of the NEMS resonator. We demonstrate the effectiveness of the technique by detecting small impedance changes originating from NEMS electromechanical resonances that are accompanied by large static background impedances at very high frequencies. This technique allows the study of important experimental systems such as doped semiconductor NEMS and may provide benefits to other high frequency displacement transduction circuits.

© *2002 American Institute of Physics.* [DOI: 10.1063/1.1507833]

* This section has been published as: K. K. L. Ekinci, Y. T. Yang, X. M. H. Huang, and M. L. Roukes, *Appl. Phys. Lett.* **78** 162 (2002).

7.1 Introduction

The recent efforts to scale microelectromechanical systems (MEMS) down to the submicron domain[1] have opened up an active research field. The resulting nanoelectromechanical systems (NEMS) with fundamental mechanical resonance frequencies reaching into the microwave bands are suitable for a number of important technological applications. Experimentally, they offer potential for accessing interesting phonon mediated processes and the quantum behavior of mesoscopic mechanical systems.

Among the most needed elements for developing NEMS based technologies—as well as for accessing interesting experimental regimes—are broadband, on-chip transduction methods sensitive to subnanometer displacements. While displacement detection at the scale of MEMS has been successfully realized using magnetic,[2] electrostatic[3,4] and piezoresistive[5] transducers through electronic coupling, most of these techniques become insensitive at the submicron scales.

7.2 Circuit Schemes and Measurement Results

An on-chip displacement transduction scheme that scales well into the NEMS domain and offers direct electronic coupling to the NEMS displacement is magnetomotive detection.[6,7] Magnetomotive reflection measurements as shown schematically[8] in figure 7.1(a) have been used extensively.[6,7,9] Here, the NEMS resonator is modeled as a parallel *RLC* network with a mechanical impedance, $Z_m(\omega)$, a two-terminal dc coupling resistance, R_e, and mechanical resonance frequency, ω_0. When

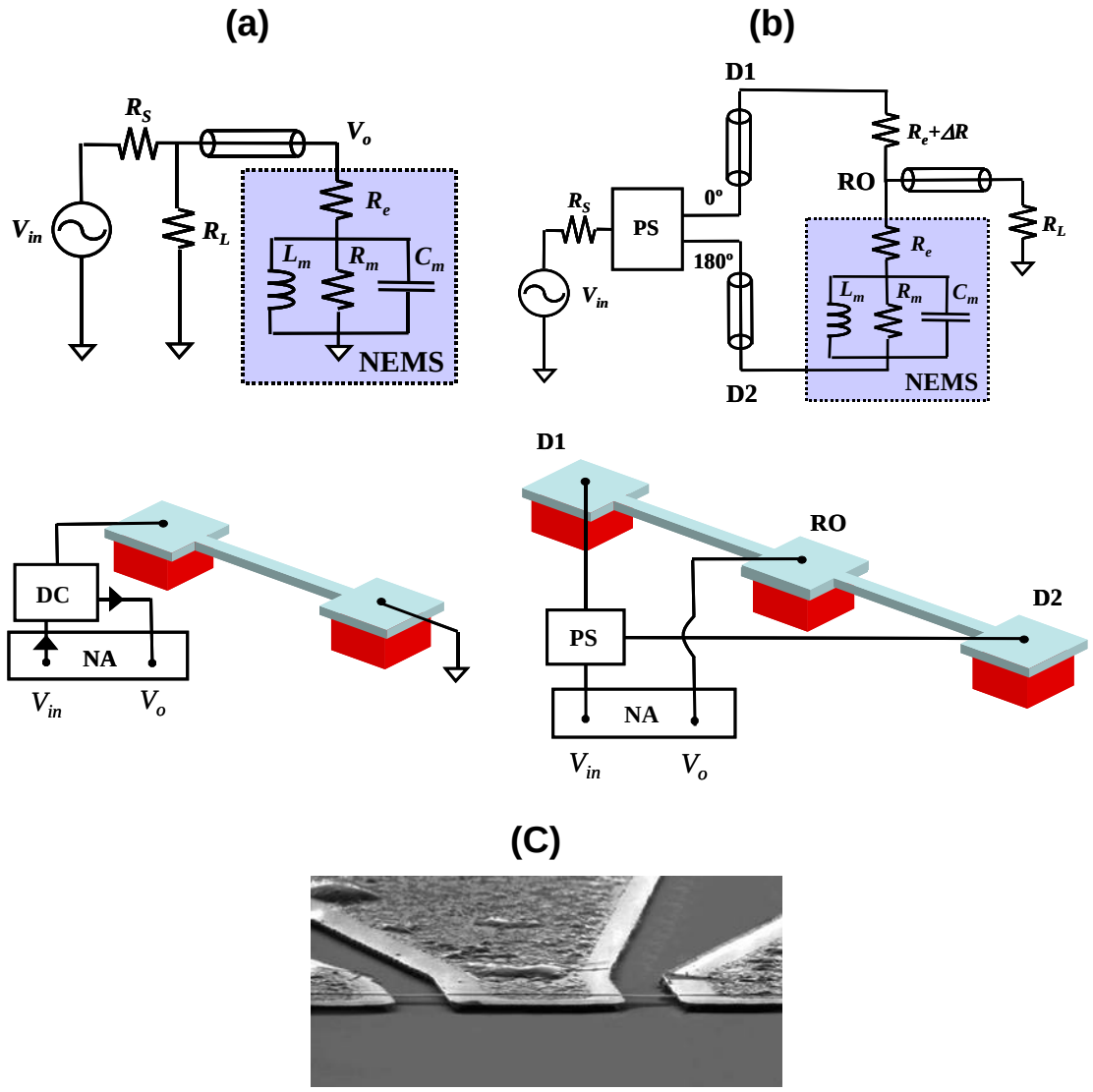

Figure 7.1. Schematic diagrams for the magnetomotive reflection measurement and bridge measurement (a) Schematic diagram for the magnetomotive reflection mesurement. In both reflection and bridges measurements, a network analyzer (NA) supplies the drive voltage, V_{in}. In reflection measurement, a directional coupler (DC) is implemented to access the reflected signal from the device. **(b) Schematic diagram for the magnetomotive bridge measurement.** V_{in} is split into two out-of-phase components by a power splitter (PS) before it is applied to ports D1 and D2. (c) Scanning electron micrograph of a representative bridge device, from an epitaxially grown wafer with 50 nm thick n^+ GaAs and 100 nmGaAs structure layer on top. The doubly clamped beams with dimensions of 8 μm(L) × 150 nm(w) × 500 nm(t) at the two arms of the bridge have in plane fundamental flexural mechanical resonances at ~35 MHz. D1, D2, and RO ports on the device are as shown.

driven at ω by a source with impedance R_s, the voltage on the load, R_L, can be approximated as

$$V_0(\omega) = V_{in}(\omega)\frac{R_e + Z_m(\omega)}{R_L + (R_e + Z_m(\omega))} \cong V_{in}(\omega)\frac{R_e + Z_m(\omega)}{R_L + R_e}. \quad (7.1)$$

Here, $R_L = R_S = 50\Omega$. We have made the approximation that $R_e >> |Z_m(\omega)|$, as is the case in most experimental systems. Apparently, the measured electromotive force (EMF) due to the NEMS displacement proportional to $|Z_m(\omega)|$ is embedded in a background close to the drive voltage amplitude, $|V_0| \sim |V_{in}| - 20\log R_e/(R_L + R_e)$ dB.[10] This facilitates the definition of a useful parameter at $\omega = \omega_0$, the detection *efficiency*, *S/B*, as the ratio of the signal voltage to the background. For the reflective, one-port magnetomotive measurement of figure 7.1(a), $S/B = Z_m(\omega_0)/R_e = R_m/R_e$, indicating some shortcomings. First, detection of the EMF becomes extremely challenging, when $R_e << R_m$, i.e., in unmetallized NEMS devices or metallized high frequency NEMS (small R_m). Second, the voltage background prohibits the use of the full dynamic range of the detection electronics. In addition to the balanced bridge detection here, we describe two-port schem to improve the detection efficiency, i.e., *S/B* ratio.[11]

The balanced circuit shown in figure 7.1(b) with a NEMS resonator on one side of the bridge and a matching resistor of resistance, $R = R_e + \Delta R$ on the other side, is designed to improve *S/B*. The voltage, $V_0(\omega)$ at the readout (RO) port is nulled for $\omega \neq \omega_0$, by applying two 180° out of phase voltages to the Drive 1 (D1) and Drive 2 (D2) ports in the circuit. We have found that the circuit can be balanced with exquisite sensitivity, by fabricating two identical doubly clamped beam resonators on either side of

the balance point (RO), instead of a resonator and a matching resistor, as shown in figure 7.1(c). In such devices, we almost always obtained two well-separated mechanical resonances, one from each beam resonator, with $|\omega_2 - \omega_1| >> \omega_1 / Q$ where ω_i and Q are the resonance frequency and the quality factor of resonance of the resonators (i=1,2) (see figure 7.3). This indicates that in the vicinity of either mechanical resonance, the system is well described by the mechanical resonator-matching resistor model of figure 7.1(b). We attribute this behavior to the high Q factors ($Q \geq 10^3$) and the extreme sensitivity of the resonance frequencies to local variations of parameters during the fabrication process.

First, to clearly assess the improvements, we compared reflection and balanced bridge measurements of the fundamental flexural resonances of doubly clamped beams patterned from n^+ (B-doped) Si as well as from n^+ (Si-doped) GaAs. Electronic detection of mechanical resonances of these types of NEMS resonators have proven to be Challenging,[12] since for these systems $R_e \geq 2k\Omega$ and $R_m \leq R_e$. Nonetheless, with the bridge technique we have detected fundamental flexural resonances in the 10 MHz<f_0 <85 MHz range for n^+ Si resonators and in the 7 MHz <f_0<35 MHz range for n^+ GaAs beams. In all our measurements, the paradigm that $R_m << R_e$ remained true as $R_m = 10\,\Omega$ and 2 k$\Omega < R_e <$ 20 kΩ. Here, we focus on our results from n^+ Si beams. These were fabricated from a B-doped Si on insulator wafer, with Si layer and buried oxide layer thicknesses of 350 and 400 nm, respectively. The doping was done at 950 $^\circ$C. The dopant concentration was estimated as $N_d \approx 6x10^{19}$ cm^{-3} from the sample sheet resistance, $R_\square$=60 Ω.[13] The fabrication of the actual devices involved optical lithography, electron beam lithography, and lift-off steps followed by anisotropic electron cyclotron resonance

plasma and selective HF wet etches.[7,9,12] The electromechanical response of the bridge was measured in a magnetic field generated by a superconducting solenoid. Figure 7.2(a) shows the response of a device with dimensions 15 μm(L) × 500 nm(w) × 350 nm(t) and with $R_e = 2.14\,\mathrm{k}\Omega$, measured in the reflection (upper curves) And bridge configurations for several magnetic field strengths. The device has an in plane flexural resonance at 25.598 MHz with $Q = 3x10^4$ at $T = 20\,\mathrm{K}$. With $\Delta R \approx 10\,\Omega$ a background reduction of a factor of $R_e / \Delta R =$ 200 was obtained in the bridge measurements (see analysis below). Figure 7.2(b) shows a measurement of the broadband transfer functions for both configurations for comparable drives at zero magnetic field. Notice the dynamic background reduction in the relevant frequency range.

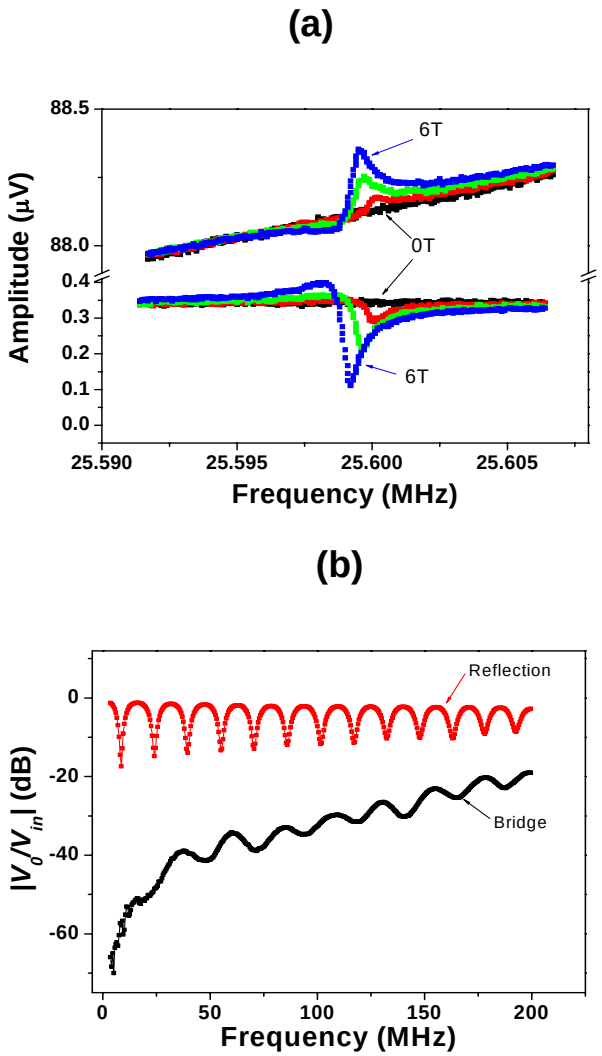

Figure 7.2 Data from a doubly clamped n^+ Si beam. (a) Mechanical resoanance. The mechanical resonance at 25.598 MHz with a Q~3x10^4 from a doubly clamped, n^+ Si beam is measured in reflection (upper curves) and in bridge (lower curves) configurations for magnetic field strengths of B=0,2,4,6 T. The drive voltages are equal. The background is reduced by a factor of ~200 in the bridge measurements. The phase of the resonance in the bridge measurements can be shifted 180° with respect to the drive signal (see Fig.7.1). **(b) The amplitude of the broadband transfer functions.** The broadband transfer function $H_B(\omega) = V_0(\omega)/V_{in}(\omega)$ for reflection (upper curve) and bridge (lower curve) configurations. The data indicate a background reduction of at least 20 dB and capacitive coupling between the actuation–detection ports in the bridge circuit.

Bridge measurements also provided benefits in the detection of electromechanical resonances from metallized VHF NEMS. These systems generally possess high R_e and R_m diminishes quickly as the resonance frequencies increase. Here, we present from our measurements on doubly clamped SiC beams embedded within the bridge configuration. These beams were fabricated with top metallization layers using a process described in detail.[9] For such beams with $R_e = 100\,\Omega$ and $R_m \leq 1\,\Omega$, we were able to detect mechanical flexural resonances deep into the VHF band. Figure 7.3(a) depicts a data trace of the in plane flexural mechanical resonances of two 2 μm (L) × 150 nm (w) × 80 nm (t) doubly clamped SiC beams. Two well-separated resonances are extremely prominent at 198.00 and 199.45 MHz, respectively, with Q=10^3 at T= 4.2 K. The broadband response from the same device is plotted in figure 7.3(b). A reflection measurement in the vicinity of the mechanical resonance frequency of this system would give rise to an estimated background on the order, $|V_0 / V_{in}|$ =-20dB,[10] making the detection of the resonance extremely challenging.

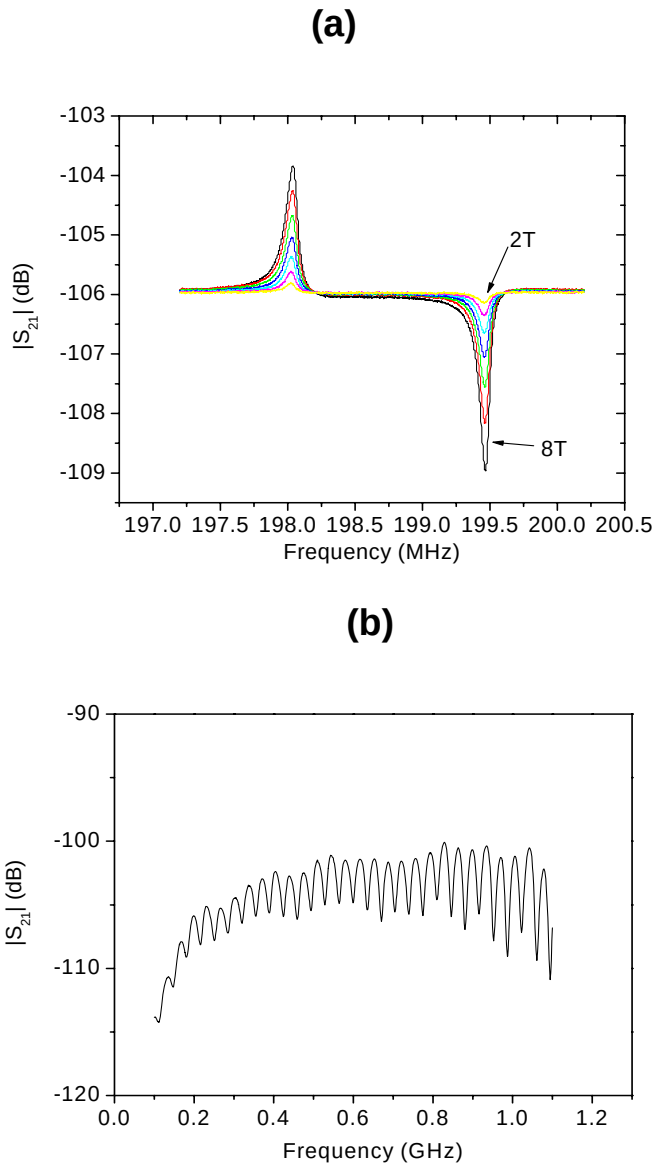

Figure 7.3. Narrow band and broadband transfer function (S_{21}) amplitudes from metallized SiC beams in bridge configuration. (a) The narrow band response. The narrowband response is measured for different magnetic field strengths of B=2, 4, 6, 8 T and shows two well-separated resonances at 198.00 and 199.45 MHz, respectively, with Q=10^3. **(b) The broadband response.** The broadband response at B=0 T shows the significant background nulling attainable in bridge measurements. We estimate that a reflection measurement on this system would produce $\left|V_0 / V_{in}\right|$=20dB for $\omega \approx \omega_0$.

Figure 7.1(b) depicts our analysis of the bridge circuit. The voltage at point RO in the circuit can be determined as[14]

$$V_0(\omega) = -\frac{V_{in}(\omega)[\Delta R + Z_m(\omega)]}{(\Delta R + Z_m(\omega))(1 + R_e / R_L) + R_e(2 + R_e / R_L)} = -\frac{V_{in}(\omega)}{Z'_{eq}(\omega)}[\Delta R + Z_m(\omega)], \qquad (7.2)$$

in analogy to equation (7.1). At $\omega = \omega_0$, $S/B = R_m / \Delta R$. Given that ΔR is small, the background is suppressed by a factor of order $R_e / \Delta R$, as compared to the one-port case as shown in figure 7.2(a). At higher frequencies, however, the circuit model becomes imprecise as is evident from the measurements of the transfer function. Capacitive coupling becomes dominant between D1, D2, and RO ports as displayed in figure 7.2(b), and this acts to reduce the overall effectiveness of the technique. With careful design of the circuit layout and the bonding pads, such problems can be minimized. Even further signal improvements can be obtained by addressing the significant impedance mismatch, $R_e \geq R_L$, between the output impedance, R_e, and the amplifier input impedance, R_L. In the measurements displayed in figure 7.2(a), this mismatch caused a signal attenuation estimated to be of order ~40 dB.

Our measurements on doped NEMS offer insight into energy dissipation mechanisms in NEMS, especially those arising from surfaces and surface adsorbates. In the frequency range investigated, 10 MHz < f_0 < 85 MHz, the measured Q factors of $2.2\text{x}10^4 < Q < 8\text{x}10^4$ in n^+ Si beams is a factor of 2–5 higher than those obtained from metallized beams.[15] Both metallization layers[16] and impurity dopants[3] can make an appreciable contribution to the energy dissipation. Our measurements on NEMS seem to confirm that metallization overlayers can significantly reduce Q factor. The high Q factors attained and the metal free surfaces make doped NEMS excellent tools for the

investigation of small energy dissipation changes due to surface adsorbates and defects. In fact, efficient *in situ* resistive heating in doped beams through R_e has been shown to facilitate thermal annealing[17] and desorption of surface adsorbates—yielding even higher quality factors.

7.3 Conclusion

In conclusion, we have developed a broadband, balanced radio frequency bridge technique for detection of small NEMS displacements. This technique may prove useful for other high frequency high impedance applications such as piezoresistive displacement detection. The technique, with its advantages, has enabled electronic measurements of NEMS resonances otherwise essentially unmeasurable.

References

1. M. L. Roukes Nanoelectromechanical systems face the future. *Phys. World* **14**, 25 (2001).

2. D. S. Greywall, B. Yurke, P. A. Busch, A. N. Pargellis, and R. L. Willett Evading amplifier noise in nonlinear oscillators. *Phys. Rev. Lett.* **72**, 2992 (1994).

3. R. E. Mihailovich and J. M. Parpia Low-temperature mechanical-properties of boron-doped silicon. *Phys. Rev. Lett.* **68**, 3052 (1992).

4. W. C. Tang, T. C. H. Nguyen, M. W. Judy, and R. T. Howe Electrostatic-comb drive of lateral polysilicon resonators. *Sens. Actuator* **A 21**, 328 (1990).

5. M. Tortonese, R. C. Barrett, and C. F. Quate Atomic resolution with an atomic force microscope using piezoresistive detection. *Appl. Phys. Lett.* **62**, 834 (1993).

6. A. N. Cleland and M. L. Roukes Fabrication of high frequency nanometer scale mechanical resonators from bulk Si crystals. *Appl. Phys. Lett.* **69,** 2653 (1996).

7. A. N. Cleland and M. L. Roukes External control of dissipation in a nanometer-scale radiofrequency mechanical resonator. *Sens. Actuator* **A 72**, 256 (1999).

8. To simplify, the length of the transmission line, l_t, between the NEMS and the measurement point has been set to $l_t \approx \lambda/2$ where λ is the drive wavelength. Also, the reflection coefficient, Γ, from the NEMS, defined as the ratio of the amplitudes of reflected to incident voltages, is taken as unity. Experimentally, *l* is readily adjustable and Γ closed to unity with R_e close to 100 $\Omega \rightarrow$ 1 kΩ.

9. Y. T. Yang, K. L. Ekinci, X. M. H. Huang, L. M. Schiavone, M. L. Roukes, C. A. Zorman, and M. Mehregany Monocrystalline silicon carbide nanoelectromechanical systems. *Appl. Phys. Lett.* **78**, 162 (2001).

10. When $\Gamma \neq 1$, $V_0 \cong \Gamma V_{in}(R_e + Z(\omega))/(R_L + R_e)$, giving a correction to the background on the order of $-20\log\Gamma$ dB.

11. See chapter 4.

12. L. Pescini, A. Tilke, R. H. Blick, H. Lorenz, J. P. Kotthaus, W. Eberhardt, and D. Kern Suspending highly doped silicon-on-insulator wires for applications in nanomechanics. *Nanotechnology* **10**, 418 (1999).

13. S. M. Sze *Physics of Semiconductor Devices* (New York, Wiley, 1981).

14. Replacing R_e with $R_e + R_S$ would produce the more general form.

15. We have qualitatively compared *Q* factors of eight metallized and 14 doped Si beams measured in different experimental runs, spanning the indicated frequency range.

16. X. Liu, E. J. Thompson, B. E. White, and R. O. Pohl Low-temperature internal friction in metal films and in plastically deformed bulk aluminum. *Phys. Rev. B* **59**, 11767 (1999).

17. K. Y. Yasumura, T. D. Stowe, E. M. Chow, T. Pfafman, T. W. Kenny, B. C. Stipe, and D. Rugar Quality factors in micron- and submicron-thick cantilevers. *J. Microelectromech. Syst.* **9**, 117 (2000).